EPRI

Community Multiscale Air Quality - Model of Aerosol Dynamics, Reaction, Ionization, and Dissolution (CMAQ-MADRID)

Technical Documentation

Technical Report

Community Multiscale Air Quality—Model of Aerosol Dynamics, Reaction, Ionization, and Dissolution (CMAQ-MADRID)

Technical Documentation

1005239

Final Report November 2002

EPRI Project Manager
N. Kumar

EPRI • 3412 Hillview Avenue, Palo Alto, California 94304 • PO Box 10412, Palo Alto, California 94303 • USA
800.313.3774 • 650.855.2121 • askepri@epri.com • www.epri.com

DISCLAIMER OF WARRANTIES AND LIMITATION OF LIABILITIES

ORGANIZATION(S) THAT PREPARED THIS DOCUMENT

Atmospheric and Environmental Research, Inc.

ORDERING INFORMATION

Requests for copies of this report should be directed to EPRI Orders and Conferences, 1355 Willow Way, Suite 278, Concord, CA 94520, (800) 313-3774, press 2 or internally x5379, (925) 609-9169, (925) 609-1310 (fax).

CITATIONS

This report was prepared by

Atmospheric and Environmental Research, Inc.
2682 Bishop Drive
Suite 120
San Ramon, CA 94583

Principal Investigators
Y. Zhang
B. Pun
K. Vijayaraghavan
S. Wu
C. Seigneur

This report describes research sponsored by EPRI.

The report is a corporate document that should be cited in the literature in the following manner:

Community Multiscale Air Quality—Model of Aerosol Dynamics, Reaction, Ionization, and Dissolution (CMAQ-MADRID): Technical Documentation, EPRI, Palo Alto, CA: 2002. 1005239.

REPORT SUMMARY

States need three-dimensional (3-D) air quality models to develop State Implementation Plans (SIPs) in order to meet National Ambient Air Quality Standards (NAAQS) for particulate matter (PM) and ensure reasonable progress under regional haze regulations. This report describes a new 3-D PM air quality model, which uses the Community Multiscale Air Quality (CMAQ) model as the host and includes new modules for aerosol processes as well as gas- and aqueous-phase chemistry.

Background

Existing 3-D models for particulate matter have several limitations in their treatment of aerosols that should be addressed before they can provide reliable insights/results in a regulatory context. To address such limitations, EPRI sponsored enhancement of the CMAQ 3-D grid-based air quality model developed by the U.S. Environmental Protection Agency (EPA).

Objectives

- To add new modules for aerosol processes as well as gas- and aqueous-phase chemistry to the CMAQ model.
- To apply the enhanced model to simulation of an air pollution episode in the Los Angeles basin.

Approach

Developers selected CMAQ as the 3-D host air quality model following a review of various 3-D models. The CMAQ model can be applied to simulate ozone and other photochemical oxidants, PM, toxic air pollutants, and the deposition of other pollutants such as acids and nitrogen species. New CMAQ modules include the Model of Aerosol Dynamics, Reaction, Ionization, and Dissolution (MADRID); the Carnegie-Mellon University (CMU) aqueous-phase chemical kinetic mechanism; and the Caltech Atmospheric Chemistry Mechanism (CACM). In addition, developers modified existing CMAQ modules, either to be compatible with the new modules or to provide better representation of atmospheric processes. No modifications were made to the CMAQ transport modules (advection, convection, and turbulent diffusion). The new 3-D PM air quality model—referred to as CMAQ-MADRID—is an option within CMAQ, enabling users to select either CMAQ or CMAQ-MADRID within the same code.

Results

This report provides an in-depth look at each new CMAQ-MADRID module. Covered are the following areas critical to PM air quality modeling:

- Gas-phase chemical kinetic mechanisms, including a description of the treatment of condensable organic compounds that lead to secondary organic aerosol (SOA) formation in the original CMAQ mechanisms as well as the new mechanism, CACM
- The chemical composition of PM for organic and inorganic species, with emphasis on thermodynamic equilibrium for species and partitioning of hydrophilic compounds
- Aerosol dynamics, including representation of the particle size distribution and the processes that govern it in MADRID—in particular, new particle formation, condensational growth (or shrinkage by volatilization), and mass transfer between the bulk gas phase and the particles
- Cloud processes, including particle scavenging, aqueous-phase chemistry, and particle formation following cloud evaporation
- Heterogeneous reactions taking place at the surface of particles or droplets
- Dry deposition and wet deposition of particles and condensable organic species

EPRI Perspective

CMAQ-MADRID was applied to simulate an air pollution episode in the Los Angeles basin, with emphasis on initial and boundary conditions, meteorology, and emissions. Model performance was shown to be consistent with existing guidance. The evolution of the chemical composition of PM from coastal areas to inland areas was well reproduced by the model except that SOA and particulate nitrate formation were underpredicted. The underpredictions in nitrate were due mainly to underpredictions in the relative humidity as well as uncertainties in the emissions of primary pollutants such as volatile organic compounds, NO_x, and NH_3. The treatment of SOA formation remains an area of ongoing research, and large uncertainties currently exist for this PM component in all current air quality models. Overall, however, CMAQ-MADRID offers utilities and other stakeholders a new tool in their array of regulatory compliance options. EPRI is currently sponsoring a study where CMAQ-MADRID and other PM models are being evaluated against measurements made in the eastern United States.

Keywords

Air Quality
CMAQ-MADRID
Particulate Matter

ABSTRACT

States need three-dimensional (3-D) air quality models to develop State Implementation Plans (SIPs) in order to meet National Ambient Air Quality Standards (NAAQS) for particulate matter (PM) and ensure reasonable progress under regional haze regulations. This report describes a new 3-D PM air quality model, which uses the Community Multiscale Air Quality (CMAQ) model as the host. The CMAQ model can be applied to simulate ozone and other photochemical oxidants, PM, toxic air pollutants, and the deposition of other pollutants such as acids and nitrogen species. Module enhancements to the CMAQ model include the Model of Aerosol Dynamics, Reaction, Ionization, and Dissolution (MADRID); the Carnegie-Mellon University (CMU) aqueous-phase chemical kinetic mechanism; and the Caltech Atmospheric Chemistry Mechanism (CACM). In addition, existing CMAQ modules have been modified either to be compatible with the new modules or to provide better representation of atmospheric processes. No modifications were made to the CMAQ transport modules (advection, convection, and turbulent diffusion). The new 3-D PM air quality model—referred to as CMAQ-MADRID—is an option within CMAQ, enabling users to select either CMAQ or CMAQ-MADRID within the same code.

ACKNOWLEDGMENTS

The development of MADRID 2 and its incorporation into CMAQ was funded in part by the California Air Resources Board, Dr. Nehzat Motallebi, project manager and Professor John Seinfeld, California Institute of Technology, principal investigator. Thanks are due to Ms. Sharon LeDuc and Dr. Francis Binkowski, U.S. Environmental Protection Agency (EPA), for helpful discussions regarding the EPA CMAQ model, Professor John Seinfeld for providing us with the CIT aerosol module, Professor Mark Jacobson, Stanford University, for providing us with the moving-center condensational growth algorithm, Professor Spyros Pandis, Carnegie-Mellon University, for providing us with the CMU aqueous-phase chemistry module and the mass transfer hybrid approach, Professor Robert Griffin, Duke University, for providing us with the formulation of the Caltech Atmospheric Chemistry Mechanism (CACM), and to Mr. Athanasios Nenes, California Institute of Technology, for providing us with ISORROPIA.

CONTENTS

LIST OF FIGURES

LIST OF TABLES

1
OVERVIEW OF CMAQ-MADRID

1.1 Introduction

The demonstration of attainment of the National Ambient Air Quality Standards (NAAQS) for particulate matter (PM) and reasonable progress under the Regional Haze regulations will require the use of three-dimensional (3-D) air quality models (EPA, 2001). Recent reviews of the current status of 3-D air quality models for PM (Seigneur et al., 1999; Seigneur, 2001) have suggested that existing 3-D models have several limitations in their treatment of aerosols that should be addressed before they can provide reliable insights/results in a regulatory context. Accordingly, we present here a new 3-D air quality model for PM. It uses the Community Multiscale Air Quality model (CMAQ) as the host model and includes new modules for aerosol processes, gas-phase chemistry and aqueous-phase chemistry.

CMAQ is a three-dimensional grid-based air quality model that can be applied to simulate ozone (O_3) and other photochemical oxidants, PM, and the deposition of pollutants such as acids (i.e., sulfate, nitrate), nitrogen species, and toxic air pollutants. CMAQ was developed by the U.S. Environmental Protection Agency (EPA). CMAQ was selected as the 3-D host air quality model following a review of selected existing 3-D models (Seigneur et al., 2000a). Its original formulation has been described by Byun and Ching (1999). The version used here is the August 2000 version as released by EPA.

The new modules included in CMAQ are the Model of Aerosol Dynamics, Reaction, Ionization, and Dissolution (MADRID), the Carnegie-Mellon University (CMU) aqueous-phase chemical kinetic mechanism and the Caltech Atmospheric Chemistry Mechanism (CACM). In addition, some existing modules of CMAQ were modified either to be compatible with the new modules or to provide better representation of atmospheric processes. No modifications were made to the transport modules (i.e., advection, convection and turbulent diffusion) of CMAQ. This new PM model is referred to as CMAQ-MADRID. CMAQ-MADRID is provided as an option within CMAQ and the user can select either CMAQ or CMAQ-MADRID within the same computer code.

1.2 Options of CMAQ-MADRID

Table 1-1 summarizes the scientific modules that are currently available in CMAQ-MADRID. The scientific modules for emissions and transport processes are those of the core CMAQ code

and are not listed here. The reader is referred to the CMAQ technical documentation for those modules (Byun and Ching, 1999).

As shown in Table 1-1, two distinct optional modules are available for organic species. We refer to these two versions of MADRID as MADRID 1 and MADRID 2. MADRID 1 uses an empirical SOA approach that relies on the results of smog chamber experiments. It is compatible with the two CMAQ gas-phase mechanisms. MADRID 2 uses a mechanistic approach. It is compatible with CACM.

The various configurations for gas-phase chemistry, aqueous-phase chemistry and aerosol processes that are available to the user are listed in Table 1-2. All the CMAQ options for transport processes (advection and turbulent diffusion) are compatible with these configurations. When the particle size distribution is represented by only two sections (typically, fine and coarse particles), the only aerosol processes that are simulated are thermodynamic equilibrium and gas/particle mass transfer. Condensational growth (or shrinkage by volatilization) is not simulated because transfer of particulate mass between those two sections via this process is negligible. New particle formation can be simulated but it should be neglected since it will have no effect on a two-section size distribution. When a multi-sectional size representation is selected, then all aerosol processes are simulated (thermodynamic equilibrium, gas/particle mass transfer, condensational growth and new particle formation). The user may, however, elect to neglect gas/particle mass transfer (in the case where coarse particles do not lead to secondary aerosol species, i.e. in the absence of sea-salt) and new particle formation (in the case where PM concentrations are high, e.g., under polluted urban conditions).

The selection of the corresponding scientific modules is described in detail in the user's manual (Pun et al., 2002b).

Table 1-1
Processes simulated in CMAQ-MADRID (Transport processes are those of CMAQ and are not listed here).

Process	Module (Options are indicated with numbers)	Comments
Gas-phase chemistry	1. CBM-IV 2. RADM2 3. CACM	CBM-IV and RADM2 modified to account for additional VOC for SOA formation and heterogeneous reactions.
Photolysis rates	1. Spatial resolution of 10° 2. Spatial resolution of 1°	
Gas-particle thermodynamic equilibrium for inorganic species	1. ISORROPIA version 1.5 (sulfate, nitrate, ammonium, sodium, chloride, water)	
Gas-particle equilibrium for organic species	1. Empirical partition coefficients for absorption into an organic phase of 4 SOA from anthropogenic precursors and 34 SOA from biogenic precursors (MADRID 1) 2. Gas/particle thermodynamic equilibrium with 10 surrogate compounds by aqueous dissolution or absorption into an organic phase (MADRID 2)	Partition coefficients from Odum et al. (1997) and Griffin et al. (1999); compatible with CBM-IV and RADM2. See Pun et al. (2002) for module description; compatible with CACM.
Particle size distribution	Sectional with at least 2 size sections 1. 2-section representation (fine and coarse particles) 2. Multi-section representation	The Stokes diameter is used to define the size section boundaries; note that the $PM_{2.5}$ and PM_{10} definitions are based on the aerodynamic diameter.
Coagulation	None	Coagulation is negligible compared to other processes under most conditions.
Nucleation	1. New particle formation theory of McMurry and Friedlander (1979) 2. None	Look-up table is the default option since the full model may be too computationally demanding for 3-D simulations. Nucleation can be neglected when using two particle size sections as well as under conditions with high PM concentrations (e.g., polluted urban environment).
Condensational growth/shrinkage by volatilization	Diffusion-limited condensation/volatilization using the moving-center algorithm	Condensational growth algorithms do not apply to the two-section option. Moving-center algorithm tracks both mass and number concentrations.
Gas/particle mass transfer for inorganic species	1. Hybrid algorithm – CIT 2. Hybrid algorithm – CMU 3. Full equilibrium algorithm	Explicit mass transfer for particles with diameter > 2.15 μm

Table 1-1
(continued)

Process	Module (Options are indicated with numbers)	Comments
Gas/particle mass transfer for organic species	1. Hybrid algorithm – CIT 2. Hybrid algorithm – CMU 3. Full equilibrium algorithm	SOA formation occurs only on fine particles when full equilibrium is selected; it may occur on both coarse and fine particles with the CMU hybrid algorithm.
Cloud chemistry	1. None 2. RADM 3. CMU	Option without radical chemistry is recommended for computational efficiency in CMU.
Heterogeneous chemistry	1. None 2. Four reactions with PM and/or one reaction with droplets	Jacob (2000)
Dry deposition	Integrated flux approach	Venkatram and Pleim (1999)
Wet deposition	In-cloud (rainout) and below-cloud (washout) scavenging of gases and particles	Effective Henry's law constants used for gases

Table 1-2
Configurations available in CMAQ-MADRID.

Gas-phase chemistry[(a)]	Aqueous-phase chemistry	Aerosol processes[(b)]
CBM-IV	None	None
CBM-IV	None	MADRID 1
CBM-IV	RADM	MADRID 1
CBM-IV	CMU	MADRID 1
CBM-IV	RADM	None
CBM-IV	CMU	None
RADM2	None	None
RADM2	None	MADRID 1
RADM2	RADM	MADRID 1
RADM2	CMU	MADRID 1
RADM2	RADM	None
RADM2	CMU	None
CACM	None	None
CACM	None	MADRID 2
CACM	CMU	MADRID 2
CACM	CMU	None

(a) All gas-phase mechanisms include heterogeneous reactions on surface of particles and droplets; these reactions are not simulated when aqueous-phase chemistry and/or aerosol processes are not selected. They can also be neglected by the user.

(b) Two- and multi-size sections can be simulated with MADRID 1; only two-size sections can be simulated with MADRID 2.

1.3 Configuration of the CMAQ-MADRID Code

Figure 1-1 depicts the configuration of the aerosol modules of MADRID within CMAQ. This configuration parallels that of the original CMAQ. The user can input the PM concentrations and emissions using either the original modal representation of CMAQ or a sectional representation. All applications to date of CMAQ-MADRID have been conducted using modal inputs. A pre-processor converts the modal inputs into sectional inputs as follows.

Three kinds of inputs are specific to the aerosol module: emissions, initial conditions (IC) and boundary conditions (BC) of PM and gaseous precursors. No changes are needed for PM precursors since they are the same for both aerosol modules. The PM inputs are set up in CMAQ using modal characteristics for the size distribution (i.e., mass median diameter, standard deviation and mass of each mode). If the CMAQ-MADRID option is chosen by the user, the modal inputs from the CMAQ pre-processors are used to calculate the corresponding sectional representation according to the number of size sections selected. This calculation is done by integrating each modal distribution (i.e., Aitken, accumulation and coarse modes) over each section to obtain the modal mass corresponding to each section. For example, the calculation of the mass of the accumulation mode assigned to the first size section, M_{1a}, is as follows.

$$M_{1a} = \int_{d_{p0}}^{d_{p1}} \frac{M_a}{(2\pi)^{1/2} \log(\sigma_a)} \exp\left[-\frac{1}{2} \left(\frac{\log(d_p / d_{pa})}{\log(\sigma_a)} \right) \right] d\, d_p \qquad (1\text{-}1)$$

where M_a is the total mass of the accumulation mode, σ_a is the standard deviation of the accumulation mode, d_p is the particle diameter, d_{pa} is the geometric mean diameter of the accumulation mode, and d_{po} and d_{pl} are the lower and upper particle diameters of the first size section. Then, the resulting sectional PM size distribution is input into the Chemical Transport Model (CTM) of CMAQ. We elected to perform the conversion from modal to sectional outside of the CTM rather than within the CTM because the former approach keeps the flexibility of using sectional inputs directly (i.e., without converting modal inputs to sectional inputs) if desired. In other words, the user can input the aerosol concentrations with either a modal (e.g., from the CMAQ pre-processor, through a model-to-sectional conversion step) or sectional format. If the conversion had been incorporated within the CTM, the user would lose the flexibility of using a sectional format and would be constrained to a modal format for input.

Figure 1-2 depicts the configuration of the CMU cloud module into CMAQ. As for the aerosol module, this configuration parallels that of the original CMAQ. Similarly, the gas-phase chemical kinetic mechanism CACM is incorporated according to the configuration of other gas-phase mechanisms in CMAQ.

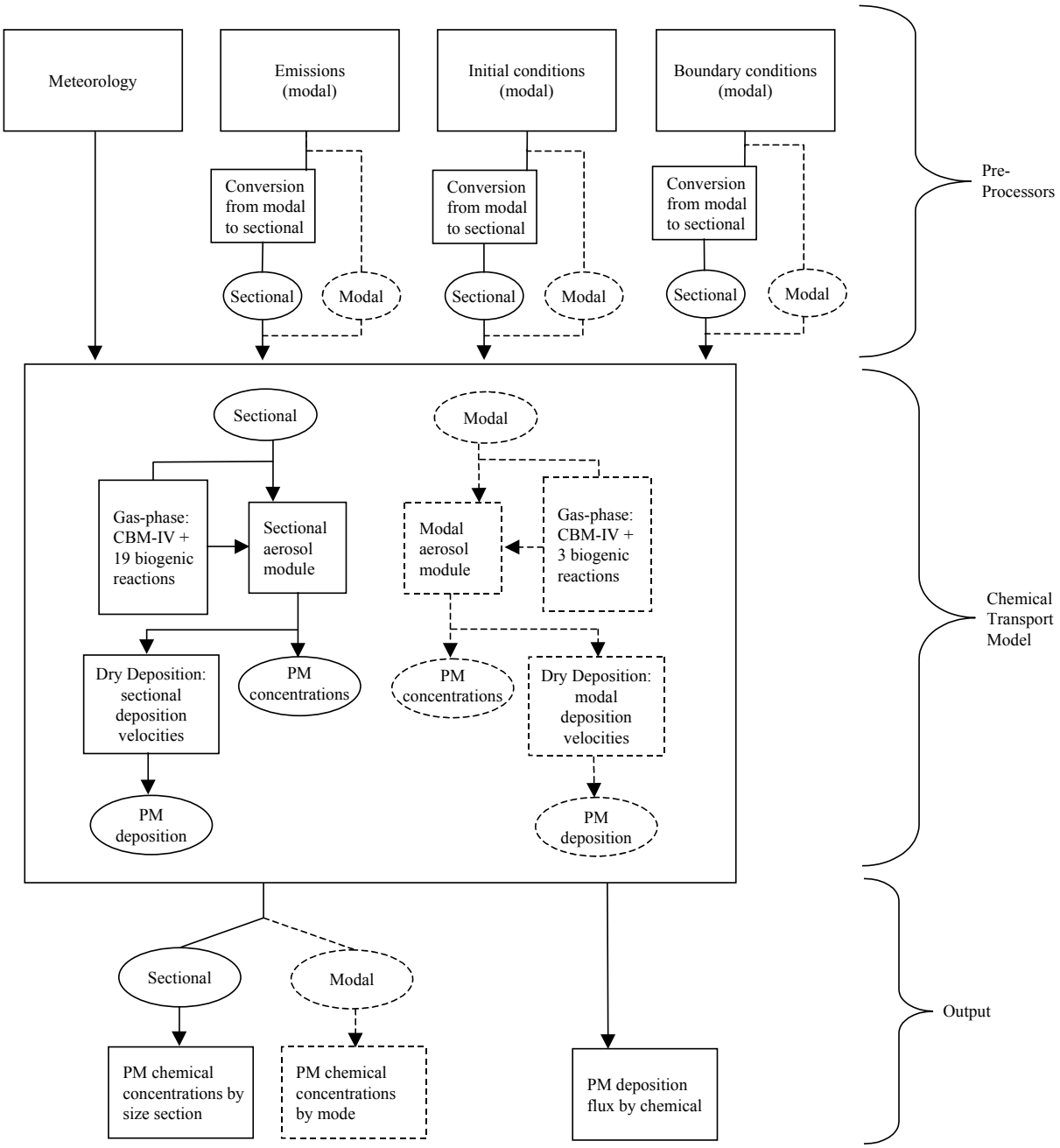

Figure 1-1
Schematic description of the incorporation of the new aerosol module MADRID into CMAQ. Only the components pertinent to the aerosol module are shown. The components specific to the original modal option are shown in dashed lines.

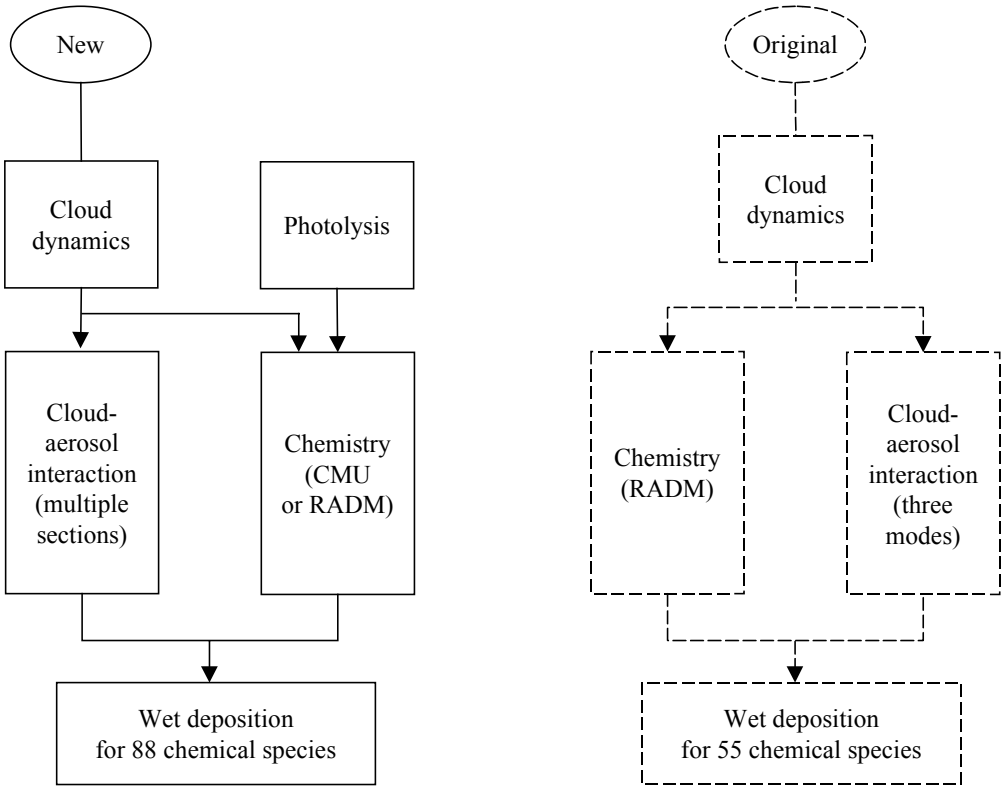

Figure 1-2
Schematic description of the incorporation of the new cloud module into CMAQ. Only the components pertinent to the cloud module are shown. The components specific to the modal option are shown in dashed lines.

1.4 Outline

We present first the gas-phase chemical kinetic mechanisms. We describe the treatment of condensable organic compounds that lead to secondary organic aerosol (SOA) formation in the original CMAQ mechanisms, as well as the new mechanism, CACM. Second, we describe the treatment of the chemical composition of PM for inorganic species and for organic species. Third, we describe the treatment of aerosol dynamics including the representation of the particle size distribution and the processes that govern it in MADRID; i.e., new particle formation, condensational growth (or shrinkage by volatilization), and mass transfer between the bulk gas phase and the particles. Fourth, we discuss cloud processes including particle scavenging, aqueous-phase chemistry, and particle formation after cloud evaporation. Fifth, we present the treatment of heterogeneous reactions taking place at the surface of particles or droplets. Finally, the treatment of dry deposition and wet deposition of particles and condensable organic species is described.

2
GAS-PHASE CHEMISTRY

Three gas-phase chemical kinetic mechanisms are available in CMAQ-MADRID: the Carbon-Bond Mechanism Version IV (CBM-IV), the Regional Acid Deposition Mechanism Version 2 (RADM2) and the Caltech Atmospheric Chemistry Mechanism (CACM). CBM-IV and RADM2 are compatible with the formulation of the secondary organic aerosol (SOA) formation of MADRID 1 whereas CACM is compatible with the formulation of SOA formation of MADRID 2. The versions of CBM-IV and RADM2 of CMAQ-MADRID differ from the original versions of CMAQ by several additional organic species and reactions that allow compatibility with the formulation of MADRID 1. We describe below these new versions as well as the new mechanism, CACM.

2.1 CBM-IV

The original formulation of CBM-IV is provided in the CMAQ technical documentation (Byun and Ching, 1999). The CMAQ-MADRID version includes some additional organic species and reactions that pertain to SOA formation. This augmentation of CBM-IV is designed in a manner that preserves the integrity of the mechanism for predicting O_3 formation. That is, the additional chemical species and reactions do not affect the chemical kinetics of SOA precursors, such as aromatics and terpenes, for O_3 formation. This is accomplished by expressing reactions in a manner that does not affect the concentrations of the chemical species involved in the CBM-IV O_3 chemistry. For example, the reaction of a new VOC precursor with an oxidant (OH, NO_3 or O_3) is written with the oxidant as a reactant as well as a product. Thus, the oxidant concentration is unaffected by this new reaction which affects only the precursor and the condensable organic product.

The MADRID 1 formulation for SOA includes two anthropogenic VOC precursors, which are characterized as one with low SOA yield and one with high SOA yield. The existing CBM-IV species TOL and XYL represent the high-yield and low-yield anthropogenic precursors, respectively. The products of the reactions of these two species with OH include the additional SOA products.

Biogenic precursors of SOA do not appear explicitly in the original version of CBM-IV because they are decomposed into their functional groups (i.e., ALD2, OLE and PAR). In the original CMAQ, CBM-IV was modified for the simulation of PM and the formation of biogenic SOA from terpenes is represented using one terpene species that does not participate in O_3 chemistry. In the CMAQ-MADRID version, twelve biogenic precursors and their corresponding reactions leading to SOA formation are included. Table 2-1 presents these chemical reactions. The

stoichiometric coefficients of the condensable organic products were obtained from the smog chamber experimental results of Odum et al. (1997) and Griffin et al. (1999). The kinetic rate constants for the first oxidation step of the VOC precursor (which is assumed to be the rate-limiting step) were obtained from the review by Lamb et al. (1999).

2.2 RADM2

The original formulation of RADM2 is provided in the CMAQ technical documentation (Byun and Ching, 1999). The CMAQ-MADRID version includes the same additional organic species and reactions that pertain to SOA formation as those added to the original CBM-IV.

TOL and YXL represent high-yield and low-yield anthropogenic SOA precursors, respectively. The reactions of these two species with OH lead to SOA products. The other reactions forming SOA include nineteen reactions distributed among twelve biogenic precursors. Table 2-1 presents these chemical reactions added to RADM2.

2.3 CACM

CACM was developed by Griffin et al. (2002a) to explicitly represent SOA formation. This mechanism contains 361 reactions of 191 species and provides detailed descriptions of several generations of products from alkanes (3 classes), alkenes (2 classes), aromatics (2 classes), alcohols (3 classes), isoprene, and terpenes (2 classes). This mechanism is uniquely suitable for modeling SOA formation because 42 condensable second- and third-generation products are explicitly represented. Its core chemical kinetic mechanism is based on RADM2. Major additions include the formation of condensable organic compounds from several anthropogenic precursors (aromatic compounds, TOL and XYL; PAH; long chain alkenes and alkene) and from two biogenic precursors. The biogenic precursors include a high-yield precursor, terpinene, and a low-yield precursor, terpinenol. Table 2-2 presents CACM.

Table 2-1
Modifications to the original CBM-IV and RADM2 gas-phase mechanisms based on the SOA formulation of MADRID 1.

Anthropogenic reactions with new products for CBM-IV		
TOL + OH → 0.08 XO2 + 0.36 CRES + 0.44 HO2 + 0.56 TO2 + 0.071 TOLAERI + 0.138 TOLAER2		
XYL + OH → 0.7 HO2 + 0.5 XO2 + 0.2 CRES + 0.8 MGLY + 1.1 PAR + 0.3 TO2 + 0.038 XYLAER1 + 0.167 XYLAER2		
Anthropogenic reactions with new products for RADM2		
TOL + OH → 0.75 TOLP + 0.25 CSL + 0.25 HO2 + 0.071 TOLAER1 + 0.138 TOLAER2		
XYL + OH → 0.83 XYLP + 0.71 CSL + 0.17 HO2 + 0.038 XYLAER1 + 0.167 XYLAER2		
Biogenic precursor (molecular weight)	**New biogenic reactions for CBM-IV and RADM2**	**Rate constants(1) (cm^3 $molec^{-1}$ s^{-1})**
Carene (136)	CAR + OH → 0.054 CARAER1 + 0.517 CARAER2 + OH	8.8×10^{-11}
	CAR + O3 → 0.128 CARAER3 + 0.068 CARAER4 + O3	3.7×10^{-17}
	CAR + NO3 → 0.743 CARAER5 + 0.254 CARAER6 + NO3	9.1×10^{-12}
Caryophyllene (204)	CRP + OH → 1.0 CRPAER + OH	1.97×10^{-10}
Humulene (206)	HUM + OH → 1.0 HUMAER + OH	2.93×10^{-10}
Limonene (136)	LIM + OH → 0.239 LIMAER1 + 0.363 LIMAER2 + OH	1.71×10^{-10}
Linalool (154)	LNL + OH → 0.073 LNLAER1 + 0.053 LNLAER2 + OH	1.59×10^{-10}
Ocimene (136)	OCI + OH → 0.045 OCIAER1 + 0.149 OCIAER2 + OH	2.52×10^{-10}
α-Pinene (136)	APIN + OH → 0.038 APINAER1 + 0.326 APINAER2 + OH	5.37×10^{-11}
	APIN + O3 → 0.125 APINAER3 + 0.102 APINAER4 + O3	8.66×10^{-17}
β-Pinene (136)	BPIN + OH → 0.13 BPINAER1 + 0.0406 BPINAER2 + OH	7.89×10^{-11}
	BPIN + O3 → 0.026 BPINAER3 + 0.485 BPINAER4 + O3	1.36×10^{-17}
	BPIN + NO3 → 1.0 BPINAER5 + NO3	2.31×10^{-12}
Sabinene (136)	SAB + OH → 0.067 SABAER1 + 0.399 SABAER2 + OH	1.17×10^{-10}
	SAB + O3 → 0.037 SABAER3 + 0.239 SABAER4 + O3	8.6×10^{-17}
	SAB + NO3 → 1.0 SABAER5 + NO3	1.0×10^{-11}
Terpinene (136)	TER + OH → 0.091 TERAER1 + 0.367 TERAER2 + OH	2.7×10^{-10}
Terpinenol (154)	TPO + OH → 0.049 TPOAER1 + 0.063 TPOAER2 + OH	1.59×10^{-10}
Terpinolene (136)	TPL + OH → 0.046 TPLAER1 + 0.034 TPLAER2 + OH	2.25×10^{-10}

(1) Lamb et al. (1999)

2.4 Spatial Resolution for the Photolytic Rates

Photolysis reactions play a very important role in the production of photochemical smog. Some of these reactions initiate the chain of atmospheric radical reactions. For example, the photolysis of formaldehyde creates two radicals that propagate atmospheric reactions, ultimately leading to the formation of ambient O_3.

$$HCHO + h\nu \rightarrow H + HCO$$

$$H + O_2 \rightarrow HO_2$$

$$HCO + O_2 \rightarrow CO + HO_2$$

The photolysis of HONO is an important source for both OH and NO early in the morning.

$$HONO + h\nu \rightarrow OH + NO$$

In addition, photolysis of NO_2 is the prelude to the formation of O_3.

$$NO_2 + h\nu \rightarrow NO + O$$

$$O + O_2 \rightarrow O_3$$

Sensitivity and uncertainty studies have identified many of these reactions to have significant influence towards the prediction of O_3 in air quality models (e.g., Zhang et al., 1998; Pun, 1998). Therefore, increasing the accuracy of the photolytic reaction rates helps improve model predictions of O_3 and other oxidants.

Table 2-2
Reactions of the Caltech Atmospheric Chemistry Mechanism[(a)].

Reaction	Reactants	Products
1	$NO_2 + h\nu$	$NO + O$
2	$O + O_2 + M$	$O_3 + M$
3	$O + NO_2$	$NO + O_2$
4	$O + NO_2 + M$	$NO_3 + M$
5	$NO + O_3$	$NO_2 + O_2$
6	$NO_2 + O_3$	$NO_3 + O_2$
7	$NO + NO_3$	$2\ NO_2$
8	$NO + NO + O_2$	$2\ NO_2$
9	$NO_2 + NO_3 + M$	$N_2O_5 + M$
10	N_2O_5	$NO_2 + NO_3$
11	$N_2O_5 + H_2O$	$2\ HNO_3$
12	$NO_2 + NO_3$	$NO + NO_2 + O_2$
13	$NO_3 + h\nu$	$NO + O_2$
14	$NO_3 + h\nu$	$NO_2 + O$
15	$O_3 + h\nu$	$O + O_2$
16	$O_3 + h\nu$	$OSD + O_2$
17	$OSD + H_2O$	$2\ OH$
18	$OSD + M$	$O + M$
19	$NO + OH + M$	$HONO + M$
20	$HONO + h\nu$	$0.9\ NO + 0.1\ NO_2 + 0.9\ OH + 0.1\ HO_2$
21	$NO_2 + H_2O$	$HONO - NO_2 + HNO_3$
22	$NO_2 + OH + M$	$HNO_3 + M$
23	$HNO_3 + OH$	$NO_3 + H_2O$
24	$CO + OH$	$HO_2 + CO_2$
25	$O_3 + OH$	$HO_2 + O_2$
26	$NO + HO_2$	$NO_2 + OH$
27	$NO_2 + HO_2 + M$	$HNO_4 + M$
28	HNO_4	$NO_2 + HO_2$
29	$HNO_4 + OH$	$NO_2 + O_2 + H_2O$
30	$O_3 + HO_2$	$OH + 2\ O_2$
31	$HO_2 + HO_2$	H_2O_2
32	$HO_2 + HO_2 + H_2O$	$H_2O_2 + O_2 + H_2O$
33	$NO_3 + HO_2$	$0.8\ NO_2 + 0.2\ HNO_3 + 0.8\ OH + O_2$
34	$O + O_3$	$2\ O_2$
35	$SO_2 + OH$	H_2SO_4 (via SO_3) $+ HO_2$
36	$H_2O_2 + h\nu$	$2\ OH$
37	$H_2O_2 + OH$	$HO_2 + H_2O$
38	$O + NO + M$	$NO_2 + M$
39	$HONO + OH$	$NO_2 + H_2O$
40	$NO_3 + OH$	$NO_2 + HO_2$
41	$NO_3 + NO_3$	$2\ NO_2 + O_2$
42	$OH + HO_2$	$H_2O + O_2$
43	$CH_4 + OH$	$RO_21 + RO_2T + H_2O$
44	$HCHO + h\nu$	$CO + 2\ HO_2$
45	$HCHO + h\nu$	$CO + H_2$
46	$HCHO + OH$	$CO + HO_2 + H_2O$
47	$HCHO + NO_3$	$HNO_3 + CO + HO_2$
48	$MEOH + OH$	$HO_2 + HCHO + H_2O$
49	$ETHE + OH$	$RO_22 + RO_2T$
50	$ETHE + NO_3$	$RO_23 + RO_2T$
51	$ETHE + O_3$	$0.315\ CO + 0.06\ HO_2 + 0.06\ OH + 0.185$ ACID $+$ 0.5 HCHO $+ 0.07\ H_2O$
52	$ETHE + O$	$0.6\ CO + HO_2 + 0.6\ RO_21 + 0.4\ RO_24 + RO_2T$

Table 2-2
Reactions of the Caltech Atmospheric Chemistry Mechanism[a]. (continued)

Reaction	Reactants	Products
53	ETOH + OH	CF(1) HO_2 + CF(1) ALD2 + CF(2) $RO_2$2 + CF(2) RO_2T + H_2O
54	OLEL + OH	$RO_2$2 + RO_2T
55	OLEL + NO_3	$RO_2$3 + RO_2T
56	OLEL + O_3	0.56 CO + 0.2 CO_2 + 0.36 OH + 0.28 HO_2 + 0.5 HCHO + 0.5 ALD2 + 0.24 ACID + 0.1 ALKL + 0.28 $RO_2$5 + 0.28 RO_2T
57	OLEL + O	0.5 ALKL + 0.4 ALD2 + 0.1 $RO_2$4 + 0.1 $RO_2$5 + 0.2 RO_2T
58	ALKL + OH	$RO_2$5 + RO_2T + H_2O
59	ALD2 + *hν*	CO + HO_2 + $RO_2$5 + RO_2T
60	ALD2 + OH	$RO_2$6 + RO_2T + H_2O
61	ALD2 + NO_3	HNO_3 + $RO_2$6 + RO_2T
62	KETL + OH	$RO_2$7 +RO_2T + H_2O
63	KETL + *hν*	$RO_2$5 + $RO_2$8 + 2 RO_2T
64	ISOP + OH	0.66 $RO_2$9 + 0.34 $RO_2$10 + RO_2T
65	ISOP + NO_3	0.66 $RO_2$11 + 0.34 $RO_2$12 + RO_2T
66	ISOP + O_3	0.068 CO_2 + 0.461 CO + 0.5 HCHO + 0.664 OH + 0.366 HO_2 + 0.054 OLEL + 0.121 ACID + 0.389 MVK + 0.17 MCR + 0.271 $RO_2$13 + 0.095 $RO_2$14 + 0.366 RO_2T
67	ISOP + O	0.925 OLEL + 0.075 ALD2
68	MTBE + OH	$RO_2$15 + RO_2T + H_2O
69	ALCH + OH	$RO_2$2 + RO_2T+ H_2O
70	KETH + OH	$RO_2$16 + RO_2T + H_2O
71	KETH + *hν*	$RO_2$5 + $RO_2$8 + 2 RO_2T
72	AROO + NO_3	HNO_3 + RAD1
73	AROO + OH	0.16 HO_2 + 0.16 AROO + 0.1 $RO_2$17 + 0.1 RO_2T + 0.74 RAD2 + 0.1 H_2O
74	OLEH + OH	$RO_2$18 + RO_2T
75	OLEH + NO_3	$RO_2$19 + RO_2T
76	OLEH + O_3	0.56 CO + 0.2 CO_2 + 0.36 OH + 0.28 HO_2 + 0.5 HCHO + 0.5 RPR1 + 0.12 ACID + 0.12 UR1 + 0.1 ALKM + 0.28 $RO_2$20 + 0.28 RO_2T
77	OLEH + O	0.5 ALKM + 0.4 RPR1 + 0.1 $RO_2$4 + 0.1 $RO_2$20 + 0.2 RO_2T
78	ALKM + OH	$RO_2$20 + RO_2T + H_2O
79	AROL + OH	0.16 HO_2 + 0.16 AROO + 0.06 $RO_2$21 + 0.78 RAD3 + 0.06 RO_2T+ 0.06 H_2O
80	AROH + OH	0.16 HO_2 + 0.16 AROO + 0.84 RAD4
81	ARAL + NO_3	HNO_3 + O_3 – HO_2 + ARAC
82	ARAL + OH	(0.16-CF(39)) HO_2 + CF(39) O_3 + CF(39) ARAC + CF(45) $RO_2$22 + CF(40) RAD5 + CF(45) RO_2T + (CF(39) + CF(45))H_2O
83	ARAC + OH	0.16 HO_2 + 0.16 UR2 + 0.1 $RO_2$23 + 0.74 RAD6 + 0.1 RO_2T+ 0.1 H_2O
84	BIOL + OH	$RO_2$24 + RO_2T
85	BIOL + NO_3	$RO_2$25 + RO_2T
86	BIOL + O_3	0.445 CO + 0.055 H_2O_2 + 0.445 HO_2 + 0.89 OH + 0.055 UR3 + 0.445 UR4 + 0.055 RPR3 + 0.445 $RO_2$26 + 0.445 RO_2T
87	BIOL + O	0.75 UR5 + 0.25 UR6
88	BIOH + OH	$RO_2$27 + RO_2T

Table 2-2
Reactions of the Caltech Atmospheric Chemistry Mechanism[a]. (continued)

Reaction	Reactants	Products
89	BIOH + NO_3	$RO_2$28 + RO_2T
90	BIOH + O_3	0.445 CO + 0.055 H_2O_2 + 0.89 OH + 0.055 UR7 + 0.055 UR8 + 0.445 $RO_2$29 + 0.445 $RO_2$30 + 0.89 RO_2T
91	BIOH + O	0.75 UR9 + 0.25 UR10
92	PAH + OH	0.16 HO_2 + 0.16 UR11 + 0.1 $RO_2$31 + 0.74 RAD7 + 0.1 RO_2T + 0.1 H_2O
93	ALKH + OH	$RO_2$32 + RO_2T + H_2O
94	RO_2T + HO_2	HO_2
95	RO_2T + NO	NO
96	RO_2T + RO_2T	RO_2T
97	RAD2 + O_2	$RO_2$33 + RO_2T
98	RAD3 + O_2	$RO_2$34 + RO_2T
99	RAD4 + O_2	$RO_2$35 + RO_2T
100	RAD5 + O_2	$RO_2$36 + RO_2T
101	RAD6 + O_2	$RO_2$37 + RO_2T
102	RAD7 + O_2	$RO_2$38 + RO_2T
103	RAD1 + NO_2	RPR4
104	RAD2 + NO_2	RPR4 + H_2O
105	RAD3 + NO_2	UR12 + H_2O
106	RAD4 + NO_2	UR13 + H_2O
107	RAD5 + NO_2	RPR5 + H_2O
108	RAD6 + NO_2	UR14 + H_2O
109	RAD7 + NO_2	UR15 + H_2O
110	$RO_2$1 + NO	NO_2 + HO_2 + HCHO
111	$RO_2$1 + RO_2T	HO_2 + HCHO + RO_2T + O_2
112	$RO_2$1 + HO_2	HO_2 + OH + HCHO
113	$RO_2$2 + NO	NO_2 + HO_2 + HCHO + ALD2
114	$RO_2$2 + RO_2T	HO_2 + HCHO + ALD2 + RO_2T + O_2
115	$RO_2$2 + HO_2	OH + HO_2 + HCHO + ALD2
116	$RO_2$3 + NO	2 NO_2 + HCHO + ALD2
117	$RO_2$3 + RO_2T	NO_2 + HO_2 + HCHO + ALD2 + O_2 + RO_2T
118	$RO_2$3 + HO_2	NO_2 + HO_2 + OH + HCHO + ALD2
119	$RO_2$4 + NO	NO_2 + CO + HO_2 + HCHO
120	$RO_2$4 + RO_2T	CO + HO_2 + HCHO + RO_2T + O_2
121	$RO_2$4 + HO_2	CO + HO_2 + OH + HCHO
122	$RO_2$5 + NO	CF(3) ALKL + CF(4) NO_2 + CF(4) HO_2 + CF(4) ALD2
123	$RO_2$5 + RO_2T	HO_2 + ALD2 + RO_2T + O_2
124	$RO_2$5 + HO_2	HO_2 + OH + ALD2
125	$RO_2$6 + NO	NO_2 + CO_2 + $RO_2$5 + RO_2T
126	$RO_2$6 + NO_2 + M	PAN1 + M
127	PAN1	NO_2 + $RO_2$6 + RO_2T
128	$RO_2$6 + HO_2	O_3 + ACID
129	$RO_2$6 + RO_2T	CO_2 + $RO_2$5 + 2 RO_2T + O_2
130	$RO_2$7 + NO	NO_2 + ALD2 + $RO_2$8 + RO_2T
131	$RO_2$7 + RO_2T	ALD2 + $RO_2$8 + 2 RO_2T + O_2
132	$RO_2$7 + HO_2	OH + ALD2 + $RO_2$8 + RO_2T
133	$RO_2$8 + NO	NO_2 + CO_2 + $RO_2$1 + RO_2T
134	$RO_2$8 + NO_2 + M	PAN2 + M
135	PAN2	NO_2 + $RO_2$8 + RO_2T
136	$RO_2$8 + HO_2	O_3 + ACID
137	$RO_2$8 + RO_2T	CO_2 + $RO_2$1 + 2 RO_2T + O_2

Table 2-2
Reactions of the Caltech Atmospheric Chemistry Mechanism[a]. (continued)

Reaction	Reactants	Products
138	$RO_2$9 + NO	CF(5) OLEL + CF(6) NO_2 + CF(6) HO_2 + CF(6) HCHO + CF(6) MVK
139	$RO_2$9 + RO_2T	HO_2 + MVK + HCHO + RO_2T + O_2
140	$RO_2$9 + HO_2	HO_2 + OH + MVK + HCHO
141	$RO_2$10 + NO	NO_2 + HO_2 + HCHO + MCR
142	$RO_2$10 + RO_2T	HO_2 + HCHO + MCR + RO_2T + O_2
143	$RO_2$10 + HO_2	HO_2 + OH + HCHO + MCR
144	$RO_2$11 + NO	2 NO_2 + HCHO + MVK
145	$RO_2$11 + RO_2T	NO_2 + HCHO + MVK + RO_2T + O_2
146	$RO_2$11 + HO_2	NO_2 + OH + HCHO + MVK
147	$RO_2$12 + NO	2 NO_2 + HCHO + MCR
148	$RO_2$12 + RO_2T	NO_2 + HCHO + MCR + RO_2T + O_2
149	$RO_2$12 + HO_2	NO_2 + OH + HCHO + MCR
150	$RO_2$13 + NO	NO_2 + HCHO + $RO_2$39 + RO_2T
151	$RO_2$13 + RO_2T	HCHO + $RO_2$39 + 2 RO_2T + O_2
152	$RO_2$13 + HO_2	HCHO + OH + $RO_2$39 + RO_2T
153	$RO_2$39 + NO	NO_2 + CO_2 + $RO_2$14 + RO_2T
154	$RO_2$39 + NO_2 + M	PAN3 + M
155	PAN3	NO_2 + $RO_2$39 + RO_2T
156	$RO_2$39 + HO_2	O_3 + 0.5 OLEL + 0.5 ACID
157	$RO_2$39 + RO_2T	CO_2 + $RO_2$14 + 2 RO_2T + O_2
158	$RO_2$14 + NO	CF(7) OLEL + CF(8) NO_2 + CF(8) $RO_2$7 + CF(8) RO_2T
159	$RO_2$14 + RO_2T	$RO_2$7 + 2 RO_2T + O_2
160	$RO_2$14 + HO_2	OH + $RO_2$7 + RO_2T
161	$RO_2$15 + NO	NO_2 + HO_2 + CF(9) ALD2 + CF(10) HCHO + CF(11) KETL + CF(12) ALKL
162	$RO_2$15 + RO_2T	HO_2 + CF(13) ALD2 + CF(14) HCHO + CF(15) KETL + CF(16) ALKL + RO_2T + O_2
163	$RO_2$15 + HO_2	OH + HO_2 + CF(13) ALD2 + CF(14) HCHO + CF(15) KETL + CF(16) ALKL
164	$RO_2$16 + NO	NO_2 + ALD2 + $RO_2$8 + RO_2T
165	$RO_2$16 + RO_2T	ALD2 + $RO_2$8 + 2 RO_2T +O_2
166	$RO_2$16 + HO_2	OH + ALD2 + $RO_2$8 + RO_2T
167	$RO_2$17 + NO	CF(21) AP1 + CF(22) NO_2 + CF(22) HO_2 + CF(22) RPR2
168	$RO_2$17 + RO_2T	HO_2 + RPR2 + RO_2T + O_2
169	$RO_2$17 + HO_2	HO_2 + OH + RPR2
170	$RO_2$18 + NO	CF(19) AP2 + CF(20) NO_2 + CF(20) HO_2 + CF(20) UR16
171	$RO_2$18 + RO_2T	HO_2 + UR16 + RO_2T + O_2
172	$RO_2$18 + HO_2	HO_2 + OH + UR16
173	$RO_2$19 + NO	2 NO_2 + HCHO + RPR1
174	$RO_2$19 + RO_2T	NO_2 + HCHO + RPR1 + RO_2T + O_2
175	$RO_2$19 + HO_2	NO_2 + OH + HCHO + RPR1
176	$RO_2$20 + NO	CF(17) AP3 + CF(18) NO_2 + CF(18) $RO_2$18 + CF(18) RO_2T
177	$RO_2$20 + RO_2T	$RO_2$18 + 2 RO_2T + O_2
178	$RO_2$20 + HO_2	OH + $RO_2$18 + RO_2T
179	$RO_2$21 + NO	CF(23) AP4 + CF(24) NO_2 + CF(24) HO_2 + CF(24) ARAL
180	$RO_2$21 + RO_2T	HO_2 + ARAL + RO_2T + O_2
181	$RO_2$21 + HO_2	HO_2 + OH + ARAL

Table 2-2
Reactions of the Caltech Atmospheric Chemistry Mechanism[(a)]. (continued)

Reaction	Reactants	Products
182	$RO_2$22 + NO	CF(41) AP5 + CF(42) NO_2 + CF(42) HO_2 + CF(42) RPR6
183	$RO_2$22 + RO_2T	HO_2 + RPR6 + RO_2T + O_2
184	$RO_2$22 + HO_2	HO_2 + OH + RPR6
185	$RO_2$23 + NO	CF(43) AP6 + CF(44) NO_2 + CF(44) HO_2 + CF(44) RPR7
186	$RO_2$23 + RO_2T	HO_2 + RPR7 + RO_2T + O_2
187	$RO_2$23 + HO_2	HO_2 + OH + RPR7
188	$RO_2$24 + NO	CF(25) AP7 + CF(26) NO_2 + CF(26) HO_2 + CF(26) RPR3
189	$RO_2$24 + RO_2T	HO_2 + RPR3 + RO_2T + O_2
190	$RO_2$24 + HO_2	HO_2 + OH + RPR3
191	$RO_2$25 + NO	2 NO_2 + RPR3
192	$RO_2$25 + RO_2T	NO_2 + RPR3 + RO_2T + O_2
193	$RO_2$25 + HO_2	NO_2 + OH + RPR3
194	$RO_2$26 + NO	NO_2 + UR17 + $RO_2$8 + RO_2T
195	$RO_2$26 + RO_2T	UR17 + $RO_2$8 + 2 RO_2T + O_2
196	$RO_2$26 + HO_2	UR17 + OH + $RO_2$8 + RO_2T
197	$RO_2$27 + NO	CF(27) AP8 + CF(28) NO_2 + CF(28) HO_2 + CF(28) UR7
198	$RO_2$27 + RO_2T	HO_2 + UR7 + RO_2T + O_2
199	$RO_2$27 + HO_2	HO_2 + OH + UR7
200	$RO_2$28 + NO	2 NO_2 + UR7
201	$RO_2$28 + RO_2T	NO_2 + UR7 + RO_2T + O_2
202	$RO_2$28 + HO_2	NO_2 + OH + UR7
203	$RO_2$29 + NO	CF(29) AP9 + CF(30) NO_2 + CF(30) $RO_2$40 + CF(30) RO_2T
204	$RO_2$29 + RO_2T	$RO_2$40 + 2 RO_2T + O_2
205	$RO_2$29 + HO_2	OH + $RO_2$40 + RO_2T
206	$RO_2$40 + NO	NO_2 + RPR8 + $RO_2$8 + RO_2T
207	$RO_2$40 + RO_2T	RPR8+ $RO_2$8 + 2 RO_2T + O_2
208	$RO_2$40 + HO_2	OH + RPR8 + $RO_2$8 + RO_2T
209	$RO_2$30 + NO	NO_2 + UR18 + $RO_2$8 + RO_2T
210	$RO_2$30 + RO_2T	UR18 + $RO_2$8 + 2 RO_2T + O_2
211	$RO_2$30 + HO_2	OH + UR18 + $RO_2$8 + RO_2T
212	$RO_2$31 + NO	CF(31) AP10 + CF(32) NO_2 + CF(32) HO_2 + CF(32) UR19
213	$RO_2$31 + RO_2T	HO_2 + UR19 + RO_2T + O_2
214	$RO_2$31 + HO_2	HO_2 + OH + UR19
215	$RO_2$32 + NO	CF(33) AP11 + CF(34) NO_2 + CF(34) $RO_2$41 + CF(34) RO_2T
216	$RO_2$32 + RO_2T	$RO_2$41 + 2 RO_2T + O_2
217	$RO_2$32 + HO_2	OH + $RO_2$41 + RO_2T
218	$RO_2$41 + NO	CF(35) AP12 + CF(36) NO_2 + CF(36) HO_2 + CF(36) UR20
219	$RO_2$41 + RO_2T	HO_2 + UR20 + RO_2T+ O_2
220	$RO_2$41 + HO_2	HO_2 + OH + UR20
221	$RO_2$33	$RO_2$42 + RO_2T
222	$RO_2$33 + NO	NO_2 + HO_2 + RPR9
223	$RO_2$33 + RO_2T	HO_2 + RPR9 + RO_2T + O_2
224	$RO_2$33 + HO_2	HO_2 + OH + RPR9
225	$RO_2$42 + NO	NO_2 + HO_2 + RP10 + MGLY
226	$RO_2$42 + RO_2T	HO_2 + RP10 + MGLY + O_2 + RO_2T
227	$RO_2$42 + HO_2	HO_2 + OH + RP10 + MGLY
228	$RO_2$34	$RO_2$43 + RO_2T
229	$RO_2$34 + NO	NO_2 + HO_2 + RP11

Table 2-2
Reactions of the Caltech Atmospheric Chemistry Mechanism[a]. (continued)

Reaction	Reactants	Products
230	$RO_2$34 + RO_2T	HO_2 + RP11 + RO_2T + O_2
231	$RO_2$34 + HO_2	HO_2 + OH + RP11
232	$RO_2$43 + NO	NO_2 + HO_2 + RP10 + MGLY
233	$RO_2$43 + RO_2T	HO_2 + RP10 + MGLY + O_2 + RO_2T
234	$RO_2$43 + HO_2	HO_2 + OH + RP10 + MGLY
235	$RO_2$35	$RO_2$44 + RO_2T
236	$RO_2$35 + NO	NO_2 + HO_2 + RP11
237	$RO_2$35 + RO_2T	HO_2 + RP11 + RO_2T + O_2
238	$RO_2$35 + HO_2	HO_2 + OH + RP11
239	$RO_2$44 + NO	NO_2 + HO_2 + RP10 + MGLY
240	$RO_2$44 + RO_2T	HO_2 + RP10 + MGLY + O_2 + RO_2T
241	$RO_2$44 + HO_2	HO_2 + OH + RP10 + MGLY
242	$RO_2$36	$RO_2$45 + RO_2T
243	$RO_2$36 + NO	NO_2 + HO_2 + RP12
244	$RO_2$36 + RO_2T	HO_2 + RP12 + RO_2T + O_2
245	$RO_2$36 + HO_2	HO_2 + OH + RP12
246	$RO_2$45 + NO	NO_2 + HO_2 + RP10 + MGLY
247	$RO_2$45 + RO_2T	HO_2 + RP10 + MGLY + O_2 + RO_2T
248	$RO_2$45 + HO_2	HO_2 + OH + RP10 + MGLY
249	$RO_2$37	$RO_2$46 + RO_2T
250	$RO_2$37 + NO	NO_2 + HO_2 + RP13
251	$RO_2$37 + RO_2T	HO_2 + RP13 + RO_2T + O_2
252	$RO_2$37 + HO_2	HO_2 + OH + RP13
253	$RO_2$46 + NO	NO_2 + HO_2 + RP10 + MGLY
254	$RO_2$46 + RO_2T	HO_2 + RP10 + MGLY + O_2 + RO_2T
255	$RO_2$46 + HO_2	HO_2 + OH + RP10 + MGLY
256	$RO_2$38	$RO_2$47 + RO_2T
257	$RO_2$38 + NO	NO_2 + HO_2 + RP14
258	$RO_2$38 + RO_2T	HO_2 + RP14 + RO_2T + O_2
259	$RO_2$38 + HO_2	HO_2 + OH + RP14
260	$RO_2$47 + NO	NO_2 + HO_2 + RP15 + MGLY
261	$RO_2$47 + RO_2T	HO_2 + RP15 + MGLY + O_2 + RO_2T
262	$RO_2$47 + HO_2	HO_2 + OH + RP15 + MGLY
263	MGLY + OH	$RO_2$48 + RO_2T + H_2O
264	MGLY + NO_3	HNO_3 + $RO_2$48 + RO_2T
265	MGLY + *hν*	CO + HO_2 + $RO_2$8 + RO_2T
266	$RO_2$48 + NO	NO_2 + CO_2 + $RO_2$8 + RO_2T
267	$RO_2$48 + NO_2 + M	PAN4 + M
268	PAN4	NO_2 + $RO_2$48 + RO_2T
269	$RO_2$48 + HO_2	O_3 + UR21
270	$RO_2$48 + RO_2T	CO_2 + $RO_2$8 + 2 RO_2T + O_2
271	MVK + OH	$RO_2$49 + RO_2T
272	MVK + O_3	0.56 CO + 0.2 CO_2 + 0.28 HO_2 + 0.36 OH + 0.5 MGLY + 0.5 HCHO + 0.12 ACID + 0.1 ALD2 + 0.12 UR21 + 0.28 $RO_2$8 + 0.28 RO_2T + 0.2 H_2O
273	MVK + O	0.85 KETL + 0.15 $RO_2$4 + 0.15 $RO_2$8 + 0.3 RO_2T
274	$RO_2$49 + NO	NO_2 + HO_2 + MGLY + HCHO
275	$RO_2$49 + RO_2T	HO_2 + MGLY + HCHO + RO_2T + O_2
276	$RO_2$49 + HO_2	HO_2 + OH + MGLY + HCHO
277	MCR + OH	CF(46) $RO_2$50 + CF(46) H_2O + CF(47) $RO_2$51 + RO_2T
278	MCR + NO_3	CF(46) HNO_3 + CF(46) $RO_2$50 + CF(47) $RO_2$52 + RO_2T

Table 2-2
Reactions of the Caltech Atmospheric Chemistry Mechanism[(a)]. (continued)

Reaction	Reactants	Products
279	MCR + O_3	0.41 CO + 0.41 HO_2 + 0.82 OH + 0.5 HCHO + 0.59 MGLY + 0.09 ACID + 0.41 $RO_2$53 + 0.41 RO_2T
280	MCR + O	0.15 CO + 0.15 HO_2 + 0.85 ALD2 + 0.15 $RO_2$7 + 0.15 RO_2T
281	$RO_2$50 + NO	CO_2 + NO_2 + $RO_2$14 + RO_2T
282	$RO_2$50 + NO_2 + M	PAN5 + M
283	PAN5	NO_2 + $RO_2$50 + RO_2T
284	$RO_2$50 + HO_2	O_3 + 0.5 ACID + 0.5 OLEL
285	$RO_2$50 + RO_2T	CO_2 + $RO_2$14 + 2 RO_2T + O_2
286	$RO_2$51 + NO	NO_2 + HO_2 + HCHO + MGLY
287	$RO_2$51 + HO_2	HO_2 + HCHO + MGLY + RO_2T + O_2
288	$RO_2$51 + RO_2T	HO_2 + OH + MGLY + HCHO
289	$RO_2$52 + NO	2 NO_2 + MGLY + HCHO
290	$RO_2$52 + HO_2	NO_2 + MGLY + HCHO + RO_2T + O_2
291	$RO_2$52 + RO_2T	NO_2 + OH + MGLY + HCHO
292	$RO_2$53 + NO	NO_2 + HCHO + $RO_2$54 + RO_2T
293	$RO_2$53 + HO_2	HCHO + $RO_2$54 + 2 RO_2T + O_2
294	$RO_2$53 + RO_2T	OH + HCHO + $RO_2$54 + RO_2T
295	$RO_2$54 + NO	CO_2 + CO + NO_2 + HO_2
296	$RO_2$54 + NO_2 + M	PAN6 + M
297	PAN6	NO_2 + $RO_2$54 + NO_2
298	$RO_2$54 + HO_2	O_3 + RP16
299	$RO_2$54 + RO_2T	CO_2 + CO + HO_2 + RO_2T + O_2
300	RPR1 + OH	$RO_2$55 + RO_2T + H_2O
301	RPR1 + NO_3	HNO_3 + $RO_2$55 + RO_2T
302	RPR1 + *hν*	CO + HO_2 + $RO_2$20 + RO_2T
303	$RO_2$55 + NO	NO_2 + CO_2 + $RO_2$20 + RO_2T
304	$RO_2$55 + NO_2 + M	PAN7 + M
305	PAN7	NO_2 + $RO_2$55 + RO_2T
306	$RO_2$55 + HO_2	O_3 + UR1
307	$RO_2$55 + RO_2T	CO_2 + $RO_2$20 + RO_2T + O_2
308	RPR2 + OH	O_3 – HO_2 + UR2 + H_2O
309	RPR3 + OH	$RO_2$56 + RO_2T + H_2O
310	RPR3 + NO_3	HNO_3 + $RO_2$56 + RO_2T
311	RPR3 + *hν*	CO + 2 HO_2 + UR4
312	$RO_2$56 + NO	NO_2 + CO_2 + HO_2 + UR4
313	$RO_2$56 + NO_2 + M	PAN8 + M
314	PAN8	NO_2 + $RO_2$56 + RO_2T
315	$RO_2$56 + HO_2	O_3 + UR3
316	$RO_2$56 + RO_2T	CO_2 + HO_2 + UR4 + RO_2T + O_2
317	RPR4 + NO_3	HNO_3 + RAD8
318	RAD8 + NO_2	UR22 + H_2O
319	RPR5 + OH	O_3 – HO_2 + UR14 + H_2O
320	RPR6 + OH	O_3 – HO_2 + RPR7 + H_2O
321	RPR7 + OH	O_3 – HO_2 + ADAC + H_2O
322	RPR8 + OH	$RO_2$57 + RO_2T + H_2O
323	RPR8 + NO_3	HNO_3 + $RO_2$57 + RO_2T
324	RPR8 + *hν*	CO + HO_2 + $RO_2$9 + RO_2T
325	RPR8 + *hν*	HO_2 + $RO_2$57 + RO_2T
326	$RO_2$57 + NO	NO_2 + CO_2 + $RO_2$9 + RO_2T
327	$RO_2$57 + NO_2	PAN9
328	PAN9	NO_2 + $RO_2$57 + RO_2T
329	$RO_2$57+ HO_2	UR23 + O_3
330	$RO_2$57 + RO_2T	CO_2 + $RO_2$9 + 2 RO_2T + O_2

Table 2-2
Reactions of the Caltech Atmospheric Chemistry Mechanism[(a)]. (continued)

Reaction	Reactants	Products
331	RPR9 + OH	$O_3 - HO_2$ + RP17 + H_2O
332	RP10 + OH	HO_2 + UR24 + H_2O
333	RP10 + *hν*	UR25
334	RP11 + OH	$O_3 - HO_2$ + UR26 + H_2O
335	RP12 + OH	$O_3 - HO_2$ + RP13 + H_2O
336	RP13 + OH	$O_3 - HO_2$ + RP18 + H_2O
337	RP14 + OH	$O_3 - HO_2$ + RP19 + H_2O
338	RP15 + OH	$O_3 - HO_2$ + UR27 + H_2O
339	RP16 + OH	$RO_2$58 + RO_2T + H_2O
340	RP16 + NO_3	HNO_3 + $RO_2$58 + RO_2T
341	RP16 + *hν*	2 CO + OH + HO_2
342	$RO_2$58 + NO	CO + CO_2 + NO_2 + OH
343	$RO_2$58 + NO_2 + M	PN10 + M
344	PN10	NO_2 + $RO_2$58 + RO_2T
345	$RO_2$58 + HO_2	O_3 + UR28
346	$RO_2$58 + RO_2T	CO + CO_2 + OH + RO_2T + O_2
347	RP17 + OH	$O_3 - HO_2$ + UR29 + H_2O
348	RP18 + OH	$O_3 - HO_2$ + UR30 + H_2O
349	RP19 + OH	$O_3 - HO_2$ + UR31 + H_2O
350	AP1 + OH	NO_2 + RPR2 + H_2O
351	AP2 + OH	NO_2 + UR16 + H_2O
352	AP3 + OH	NO_2 + UR32 + H_2O
353	AP4 + OH	NO_2 + ARAL + H_2O
354	AP5 + OH	NO_2 + RPR6 + H_2O
355	AP6 + OH	NO_2 + RPR7 + H_2O
356	AP7 + OH	NO_2 + RPR3 + H_2O
357	AP8 + OH	NO_2 + UR7 + H_2O
358	AP9 + OH	NO_2 + UR33 + H_2O
359	AP10 + OH	NO_2 + UR19 + H_2O
360	AP11 + OH	NO_2 + UR34 + H_2O
361	AP12 + OH	NO_2 + UR20 + H_2O

(a) Refer to Griffin et al. (2002a) for reaction rate constants and reference.

Current models typically use look-up tables to store photolytic rates. The photolysis rate constant j_i for compound *i*, which absorbs light between wavelengths λ_1 and λ_2, is calculated as follows:

$$j_i = \int_{\lambda_1}^{\lambda_2} F(\lambda)\,\sigma_i(\lambda)\,\phi_i(\lambda)\,d\lambda \qquad (2\text{-}1)$$

where $F(\lambda)$ is the actinic flux (photons cm^{-2} min^{-1} nm^{-1}) as a function of wavelength λ, $\sigma_i(\lambda)$ is the absorption cross section of the molecule undergoing photodissociation (cm^2 $molecule^{-1}$), and $\phi_i(\lambda)$ is the quantum yield of the photolysis reaction (molecules $photon^{-1}$). All three quantities are functions of wavelength. The integration is performed in a preprocessor, which creates a lookup table for use in the three-dimensional air quality model. For urban-scale simulations, the lookup table is typically based on time (or solar zenith angle). For regional-scale simulations, photolysis rates are stored as functions of both time and (horizontal and vertical) location.

In Models-3/CMAQ, the preprocessor JPROC is used to generate a lookup table for clear-sky photolysis rate constants based on altitude, latitude, and hours from local noon (Byun and Ching, 1999). Photolysis rate constants are then calculated within CMAQ by interpolation to the specific grid cell location and time of day and are corrected for cloud cover. In particular, photolysis rates are calculated and stored in the lookup table for 6 latitude bands from 10°N to 60°N (i.e., with 10° resolution). In CMAQ-MADRID, a 1° resolution can be used to calculate the photolysis rate constants.

The organization of JPROC is shown in Figure 2-1. The Delta-Eddington two-stream radiative transfer model is used to calculate the actinic flux used in Equation 2-1. Other inputs to the photolysis rate constant calculations include absorption cross section, quantum yields of photolytic reactions (see Equation 2-1), and profiles of temperature and pressure, since some absorption cross section and quantum yields may be functions of temperature and pressure. The actinic flux is calculated by the radiative transfer model as a function of wavelength, latitude, and altitude. The variations in actinic flux and photolysis rate constants with respect to longitude are expected to be small compared to diurnal variations. The actinic flux is calculated from (1) the extra-terrestrial irradiance, (2) oxygen (O_2) and O_3 absorption, (3) Rayleigh scattering, and (4) surface albedo. The calculation of O_2 and O_3 absorption requires the absorption cross section of these molecules, a vertical O_3 profile, and total column O_3 data (TOMS data), which are optional. Data on the vertical profile of aerosol concentrations are required to calculate albedo. Of these data, only the TOMS data and the profiles of temperature, pressure, O_3, and aerosols are functions of location. The TOMS data are available from the National Satellite Service Data Center with a resolution of 1° latitude (http://jwocky.gsfc.nasa.gov). These data are used to calculate photolysis rate constants with 1° resolution. Other input data (vertical profile data on O_3, aerosols, temperature, and pressure) use the usual 10° resolution although 1° resolution can be used if available.

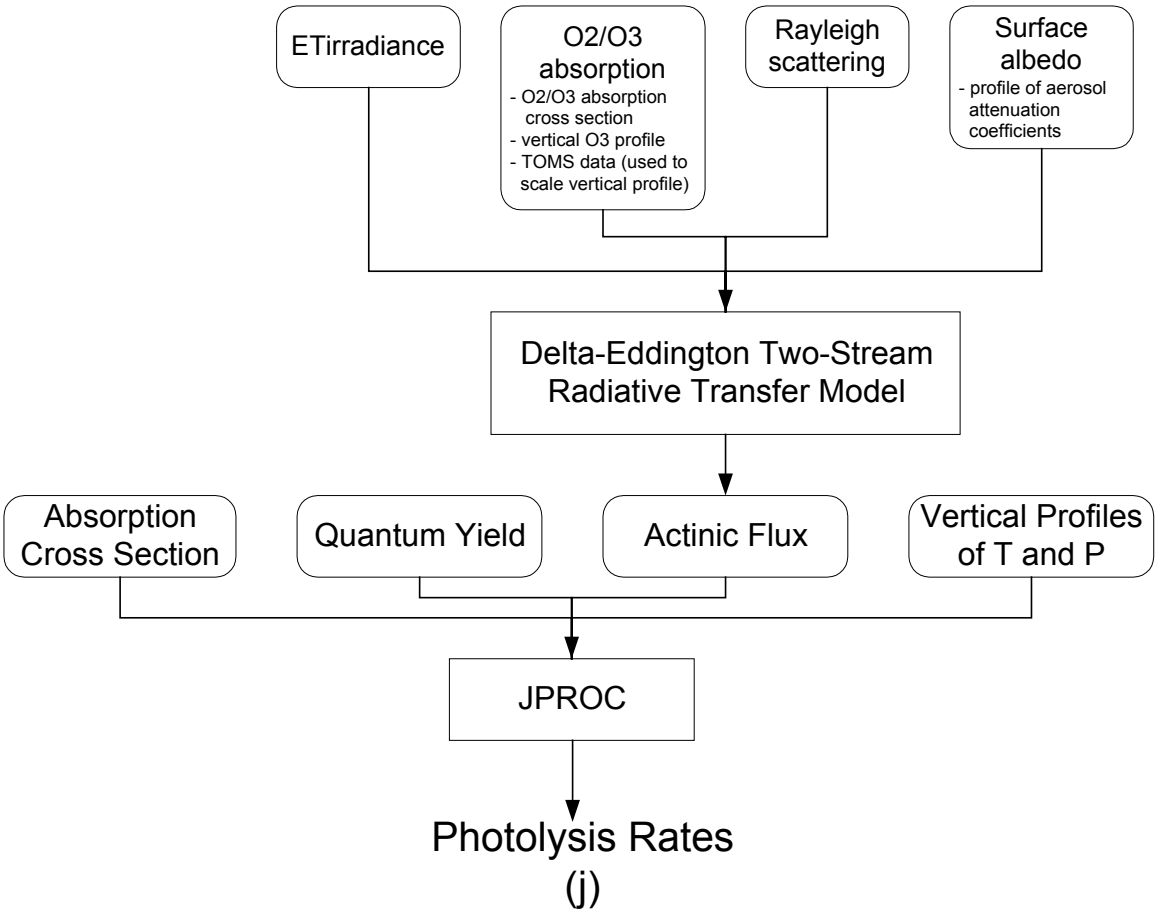

Figure 2-1
Schematic representation of the JPROC preprocessor.

Figure 2-2 presents the photolysis of NO_2 at different hour angles as a function of latitude with 1° and 10° resolution. The general behaviors of the photolysis rates are very similar despite changes in the resolution of the calculation. Figure 2-3 shows a magnified plot of j_{NO2} at local noon and at hour angle = 5 between 30° and 40° latitude, comparing the data obtained using the two different resolutions. As can be seen, the differences in the photolysis rates of NO_2 are quite small but noticeable. The one degree resolution photolysis rates can be higher or lower than the values interpolated from 10° resolution values for j_{NO2}.

The 27-28 August 1987 SCAQS episode in the Los Angeles basin was simulated to test the difference attributable to a difference in the resolution of the photolysis rate lookup files. The SCAQS domain spans 33.3 to 34.6 °N latitude. The results discussed below for three typical locations were obtained with CBM-IV. The maximum differences between the two cases were 6 ppb in Hawthorne, 8 ppb in Central Los Angeles, and 8 ppb in Riverside, respectively. In all three locations, the simulation with finer resolution for photolysis rate lookup table predicted lower peak O_3 concentrations. The maximum percentage difference in the peak O_3 concentrations at these sites is 6%. The maximum differences tend to occur in the early afternoon at the upwind sites of Hawthorne and Central Los Angeles, but later in the afternoon at

the downwind site of Riverside. During several afternoon periods, the higher resolution of photolysis rates results in slightly higher O_3 predictions at Hawthorne.

In general, the spatial resolution of the photolysis rate lookup table should be commensurate with the size of the simulation domain. For an urban-scale domain like the Los Angeles basin, a higher resolution should be used for the photolysis rate lookup table. For regional domains, the gain in accuracy with the use of a higher resolution photolysis rate lookup table must be balanced against the additional computational burden.

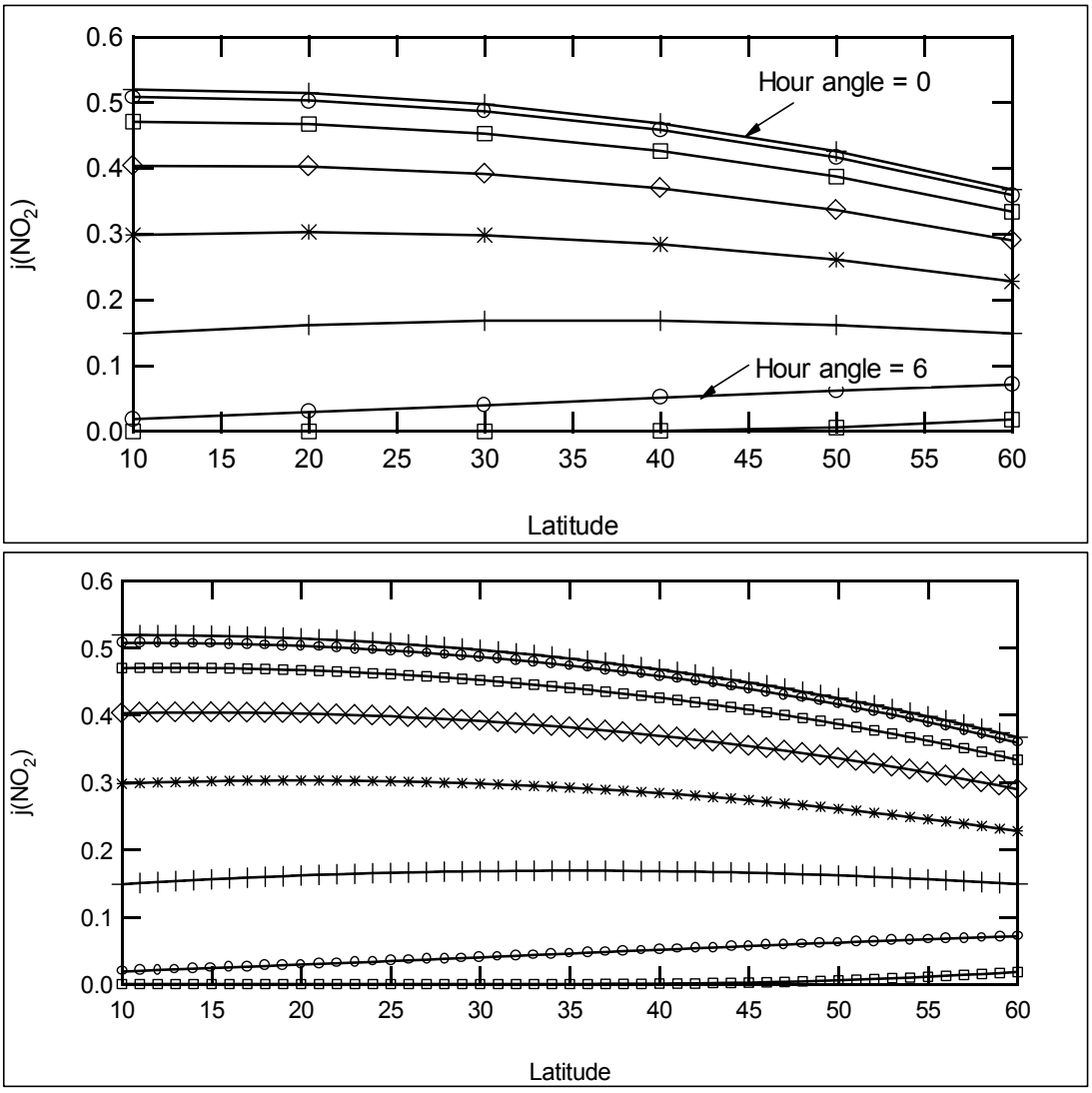

Figure 2-2
j_{NO2} (min^{-1}) as a function of latitude with (top) 10° latitude resolution and (bottom) 1° latitude resolution.

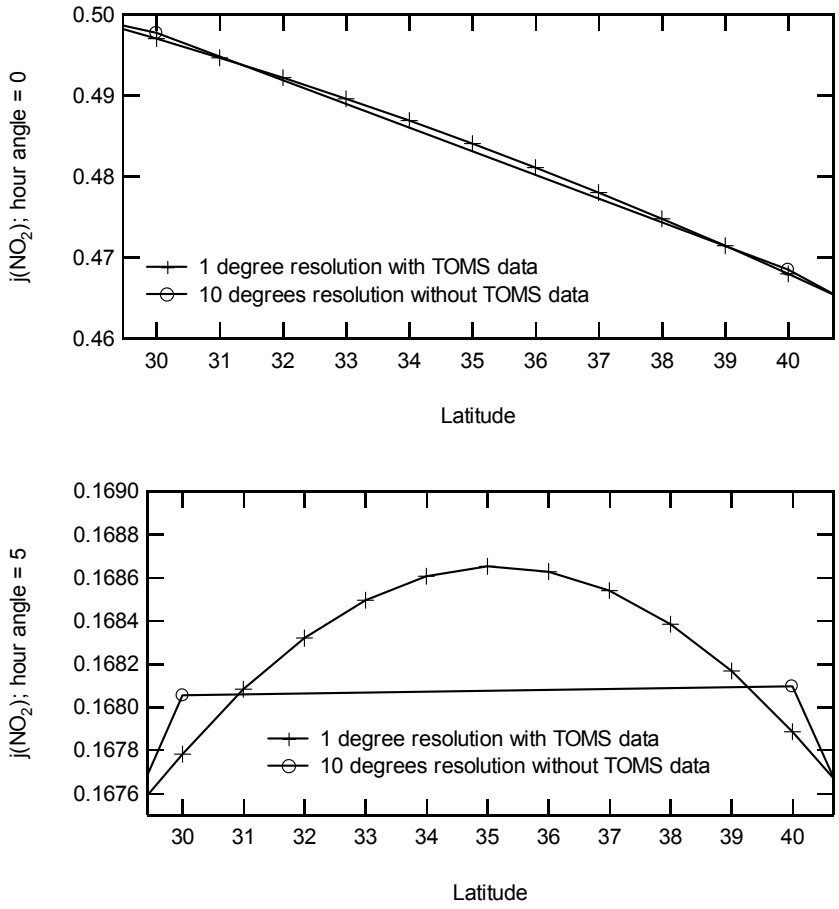

Figure 2-3
j_{NO2} (min^{-1}) at hour angle = 0 (local noon, top) and at hour angle = 5 (bottom) as a function of latitude for both 10° latitude resolution and 1° latitude resolution.

3
CHEMICAL COMPOSITION OF PARTICULATE MATTER

Particulate matter (PM) consists of primary components that have been emitted directly into the atmosphere as PM and of secondary components that have been formed as PM in the atmosphere by nucleation or condensation of gaseous species. Both primary and secondary PM species can be either inorganic or organic. They can also be of anthropogenic or biogenic origins. The formation of secondary PM is in some cases a function of the chemical composition of existing PM.

We present in this section the simulation of the formation of secondary PM in MADRID. We first describe the simulation of the chemical composition of inorganic PM. Next, we describe the simulation of the chemical composition of organic PM using either an empirical approach (MADRID 1) or a mechanistic approach (MADRID 2).

The chemical composition of PM is a function of the thermodynamic equilibrium between the particulate phase and the gas phase at the surface of the particles and a mass transfer step between the bulk gas phase and the surface of the particles. This mass transfer step can be rate limiting and can lead to non-equilibrium conditions, particularly for coarse particles. We describe here the treatment of thermodynamic equilibrium conditions. The simulation of non-equilibrium conditions due to mass transfer is described in the next section on aerosol dynamics.

3.1 Thermodynamic Equilibrium for Inorganic Species

A comprehensive review of the existing algorithms available to simulate the gas/particle equilibrium thermodynamics of inorganic species was conducted by Zhang et al. (2000) and updated as one candidate algorithm underwent some improvements. This review is summarized below.

Six modules that simulate the gas/particle partitioning of inorganic species were compared using 400 different case studies. These six modules included MARS-A (Binkowski and Shankar, 1995), SEQUILIB (Pilinis and Seinfeld, 1987), SCAPE2 (Kim and Seinfeld, 1995; Meng et al., 1995), EQUISOLV II (Jacobson, 1999), AIM2 (Clegg et al., 1998a, b) and ISORROPIA (Nenes et al., 1999). All modules treat sulfate, nitrate, ammonium and water. Except for MARS-A, all modules also treat sodium and chloride. In addition, SCAPE2 and EQUISOLV II treat crustal soluble species: calcium, magnesium, potassium and carbonate. The conclusions of this comprehensive review are summarized in Table 3-1.

AIM2 does not simulate alkaline systems and was therefore not considered for incorporation into CMAQ. MARS-A is the default module of CMAQ (the newest version of CMAQ also includes ISORROPIA). Among the computationally efficient modules, ISORROPIA was judged superior to SEQUILIB (see Table 3-1). For a comprehensive treatment of the aerosol system, both SCAPE2 and EQUISOLV II were considered suitable. They are, however, more computationally demanding than ISORROPIA. Moreover, PM emission inventories do not yet include the chemical composition of crustal species that are treated in these two modules. Therefore, ISORROPIA is used to simulate the thermodynamics of inorganic PM species in CMAQ-MADRID. Version 1.5 of ISORROPIA is currently used in CMAQ-MADRID.

Table 3-2 presents the thermodynamic equilibria that are simulated by ISORROPIA. The entire concentration domain is divided into several subdomains such as sulfate rich (free acid), sulfate rich (non free acid), sulfate poor and sodium poor, and sulfate poor and sodium rich. The systems of non-linear equations for each subdomain are ordered and manipulated so that analytical solutions could be obtained for as many equations as possible. Adopting this approach, most cases can be solved using only one level of iteration, which increases computational efficiency considerably. The bisection method is used to obtain the solution. Another factor that contributes to computational efficiency in ISORROPIA is the use of precalculated tables for binary activity coefficients for each salt and for a wide range of ionic strengths.

3.2 Thermodynamic Equilibrium for Organic Species in MADRID 1

MADRID 1 uses an empirical representation of secondary organic aerosol (SOA) formation that is based on data obtained in smog chamber experiments (Odum et al., 1997; Griffin et al., 1999). The following equation governs the gas/particle partitioning of each of the condensable species:

Table 3-1
Comparison of existing modules for gas/particle partitioning of inorganic chemical species (after Zhang et al., 2000).

	MARS-A	SEQUILIB	ISORROPIA	SCAPE2	EQUISOLV II	AIM2
Performance	Higher H_2O for medium RHs and higher NH_4NO_3 for sulfate-poor cases and low RHs	Poor NO_3^- and H^+ predictions for some sulfate-rich cases; higher NH_4NO_3 for sulfate-poor cases and low RHs	Lower NO_3^-, Cl^- and H^+ at some medium to high RHs (above 50%) for various conditions including some acidic, neutral and alkaline cases	Higher H^+ for some sulfate-rich cases and low RHs	Higher NH_4Cl for cases with NaCl and low RHs	Not valid for alkaline systems
Stability	Good	Poor for some sulfate-rich/neutral cases and high RHs cases	Good	Non-convergence for some sulfate-rich cases and low RHs	Incomplete convergence for low RHs	Numerical difficulties for very low initial H^+ and NO_3^-
Speed	Fast	Fast	Fast	Moderately fast	Slow for one cell, fast for multiple cells	Relatively slow

Table 3-2
Thermodynamic equilibria simulated in ISORROPIA (Source: Nenes et al., 1998).

Reaction	K° (298.15 K)	$\frac{\Delta H^0(T_0)}{RT_0}$	$\frac{\Delta C_p^0}{R}$	Units
$HSO_{4\,(aq)}^- \xleftrightarrow{K_1} H_{(aq)}^+ + SO_{4(aq)}^{2-}$	1.015 x 10^{-2}	8.85	25.14	mol kg^{-1}
$NH_{3(g)} \xleftrightarrow{K_{21}} NH_{3(aq)}$	5.764 x 10^{1}	13.79	–5.39	mol kg^{-1} atm^{-1}
$NH_{3(aq)} + H_2O_{(aq)} \xleftrightarrow{K_{22}} NH_{4(aq)}^+ + OH_{(aq)}^-$	1.805 x 10^{-5}	–1.50	26.92	mol kg^{-1}
$HNO_{3(g)} \xleftrightarrow{K_4} H_{(aq)}^+ + NO_{3(aq)}^-$	2.511 x 10^{6}	29.17	16.83	mol^2 kg^{-2} atm^{-1}
$HCl_{(g)} \xleftrightarrow{K_3} H^+{}_{(aq)} + Cl_{(aq)}^-$	1.971 x 10^{6}	30.20	19.91	mol^2 kg^{-2} atm^{-1}
$H_2O_{(aq)} \xleftrightarrow{K_w} H^+{}_{(aq)} + OH_{(aq)}^-$	1.010 x 10^{-14}	–22.52	26.92	mol^2 kg^{-2}
$Na_2SO_{4(s)} \xleftrightarrow{K_5} 2Na_{(aq)}^+ + SO_{4(aq)}^{2-}$	4.799 x 10^{-1}	0.98	39.75	mol^3 kg^{-3}
$(NH_4)_2SO_{4(s)} \xleftrightarrow{K_7} 2NH_{4(aq)}^+ + SO_{4(aq)}^{2-}$	1.871 x 10^{0}	–2.65	38.57	mol^3 kg^{-3}
$NH_4Cl_{(s)} \xleftrightarrow{K_6} NH_{3(g)} + HCl_{(g)}$	1.086 x 10^{-16}	–71.00	2.40	atm^2
$NaNO_{3\,(s)} \xleftrightarrow{K_9} Na_{(aq)}^+ + NO_{3(aq)}^-$	1.197 x 10^{1}	–8.22	16.01	mol^2 kg^{-2}
$NaCl_{(s)} \xleftrightarrow{K_8} Na_{(aq)}^+ + Cl_{(aq)}^-$	3.766 x 10^{1}	–1.56	16.90	mol^2 kg^{-2}
$NaHSO_{4(s)} \xleftrightarrow{K_{11}} Na_{(aq)}^+ + HSO_{4(aq)}^-$	2.413 x 10^{4}	0.79	14.75	mol^2 kg^{-2}
$NH_4NO_{3(s)} \xleftrightarrow{K_{10}} NH_{3(g)} + HNO_{3(g)}$	5.746 x 10^{-17}	–74.38	6.12	atm^2
$NH_4HSO_{4(s)} \xleftrightarrow{K_{12}} NH_{4(aq)}^+ + HSO_{4(aq)}^-$	1.383 x 10^{0}	–2.87	15.83	mol^2 kg^{-2}
$(NH_4)_3H(SO_4)_{2(s)} \xleftrightarrow{K_{13}} 3NH_{4(aq)}^+ + HSO_{4(aq)}^+ + SO_{4(aq)}^{2-}$	2.972 x 10^{1}	–5.19	54.40	mol^5 kg^{-5}

$$K_i = \left(\frac{A_i / M_{sum}}{G_i} \right) \tag{3-1}$$

where K_i ($m^3/\mu g$) is the partition coefficient obtained from the smog chamber experiments, A_i ($\mu g/m^3$ air) is the mass concentration of species *i* in the particulate phase, G_i ($\mu g/m^3$ air) is the mass concentration of species *i* in the gas phase, and M_{sum} ($\mu g/m^3$ air) is the sum of primary organic carbon (OC) (non-volatile) and secondary OC (semi-volatile) in the particulate phase that serve as the organic absorbing medium. The SOA yields for the 4 anthropogenic SOA and the 34 biogenic SOA were presented in Table 2-1. The gas/particle partitioning coefficients at experimental temperatures are presented in Table 3-3.

The smog chamber experiments from which K_i and stoichiometric coefficients were derived were conducted at temperatures higher (301 K to 316 K) than the typical ambient temperatures. Based on Pankow (1994), K_i can be related to temperature and saturation vapor pressure, which is also a function of temperature.

$$K_i = \frac{760RT}{10^6 P_i^{sat} \gamma_i (MW_{om})} \tag{3-2}$$

where R (= 8.2 x 10^{-5} m^3 atm/mol/K) is the gas constant, T (K) is temperature, P_i^{sat} (torr) is the saturation vapor pressure, γ_i is the activity coefficient of compound *i* in the liquid phase, and MW_{om} (g/mol) is the average molecular weight of the organic absorbing medium.

The Clausius-Clapeyron equation is used to account for the temperature dependence of the saturation vapor pressure

$$P_i^{sat} = B_i \exp - \left(\frac{\Delta H_{vap}}{RT} \right) \tag{3-3}$$

where B_i is the proportionality constant and ΔH_{vap} is the enthalpy of vaporization. B_i is defined from the value of the saturation vapor pressure at the reference temperature. A value of 88 kJ/mole is used for the ΔH_{vap} of condensable products from terpenes and aromatics (< C10). A value of 175 kJ/mole is used for the ΔH_{vap} of the condensable products of sesquiterpenes. The values for ΔH_{vap} correspond to the arithmetic mean of available literature data for < C10 and > C10 compounds (Tao and McMurry, 1989; Bilde and Pandis, 2001).

Table 3-3
Gas/particle partitioning coefficients of SOA in MADRID 1.

Condensable Species	K ($m^3/\mu g$) (1)
TOLAER1	0.053
TOLAER2	0.0019
XYLAER1	0.042
XYLAER2	0.0014
CARAER1	0.043
CARAER2	0.0042
CARAER3	0.337
CARAER4	0.0036
CARAER5	0.0088
CARAER6	0.0091
CRPAER	0.0416
HUMAER	0.0501
LIMAER1	0.055
LIMAER2	0.0053
LNLAER1	0.049
LNLAER2	0.0210
APINAER1	0.171
APINAER2	0.0040
APINAER3	0.088
APINAER4	0.0788
BPINAER1	0.044
BPINAER2	0.0049
BPINAER3	0.195
BPINAER4	0.0030
BPINAER5	0.0163
SABAER1	0.258
SABAER2	0.0038
SABAER3	0.819
SABAER4	0.0001
SABAER5	0.0115
OCIAER1	0.174
OCIAER2	0.0041
TPOAER1	0.159
TPOAER2	0.0045
TERAER1	0.081
TERAER2	0.0046
TPLAER1	0.185
TPLAER2	0.0024

(1) at experimental temperatures ranging from 301 to 316K.

3.3 Thermodynamic Equilibrium for Organic Species in MADRID 2

MADRID 2 uses a mechanistic representation of SOA formation. The formulation of this SOA module was developed by AER under funding from EPRI (1999) and ARB (Seinfeld et al., 2002). This AER/EPRI/Caltech SOA module is hereafter referred to as the AEC module (Pun et al., 2002a). The AEC module simulates an external mixture of hydrophilic and hydrophobic organic compounds, as shown in Figure 3-1. We describe below the generic technical approaches used to simulate the partitioning of hydrophilic and hydrophobic compounds. We also describe the specific implementation of the AEC module in CMAQ-MADRID 2 where it is coupled with CACM.

3.3.1 Partitioning of Hydrophilic Compounds

The overall structure of the hydrophilic module is depicted in Figure 3-2. Hydrophilic compounds are miscible with inorganic solutes, such as sulfate and nitrate, at relative humidities above their deliquescence. Therefore, they dissolve in existing particles that contain an aqueous phase of inorganic compounds. In this mixture, organic solutes may be present as molecules or ions (in the case of electrolytes like organic acids) in the aqueous phase. The relationship between gas-phase organic compounds and the dissolved molecules is governed by Henry's law.

$$H_{HA} = \left\{HA_{(aq)}\right\} / P_{HA} \tag{3-4}$$

where H_{HA} is the Henry's law coefficient, $\{HA_{(aq)}\}$ is the activity of the molecule in the aqueous phase and P_{HA} is the partial pressure of HA in the gas phase. The solubility of organic acids is enhanced by the dissociation of the molecules into ions. Therefore, the acid dissociation equations must also be satisfied.

$$K_A = \frac{\left\{H^+\right\}\left\{A^-\right\}}{\left\{HA_{(aq)}\right\}} \tag{3-5}$$

where K_A is the dissociation constant and $\{H^+\}$, $\{A^-\}$ and $\{HA_{(aq)}\}$ are the activities of the proton, the acid anion and acid molecule, respectively.

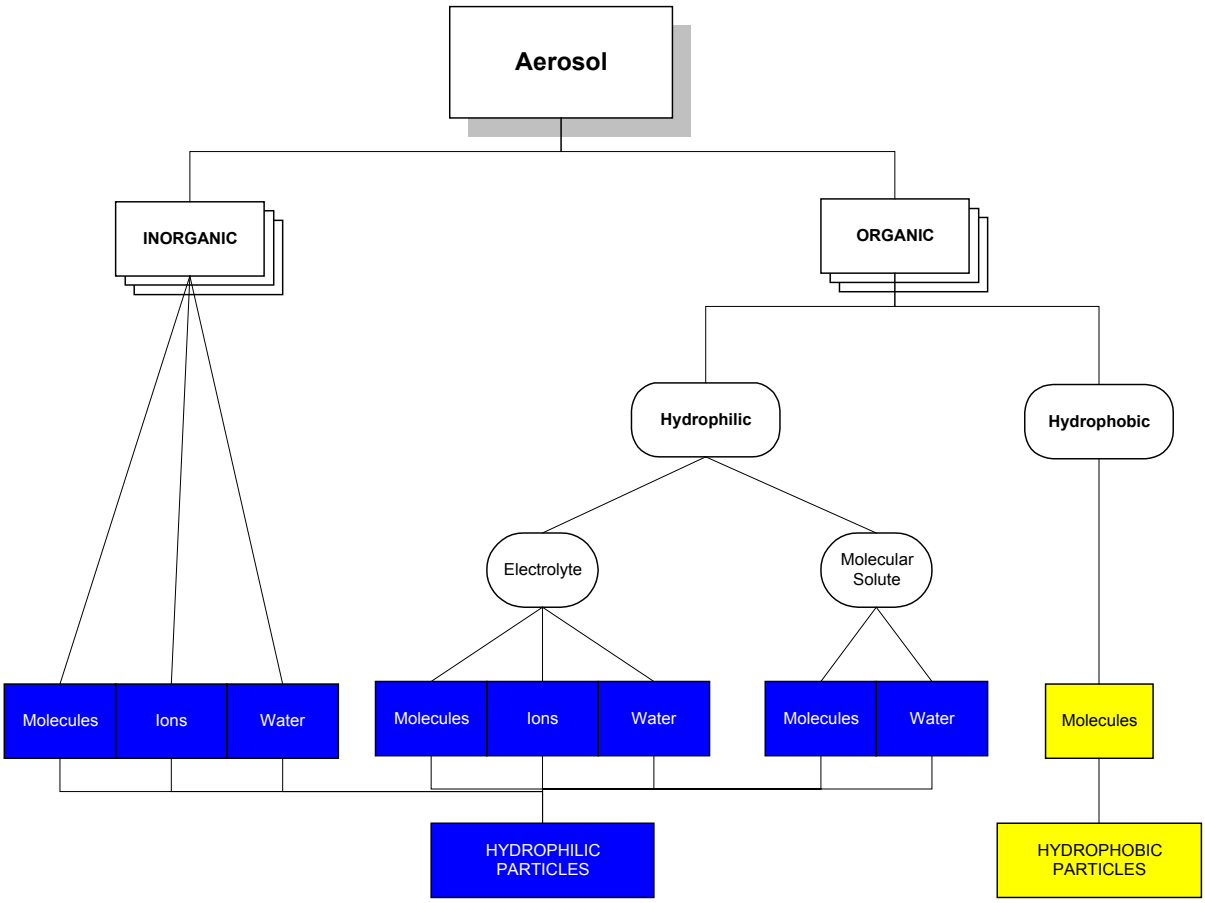

Figure 3-1
The aerosol system modeled in MADRID 2.

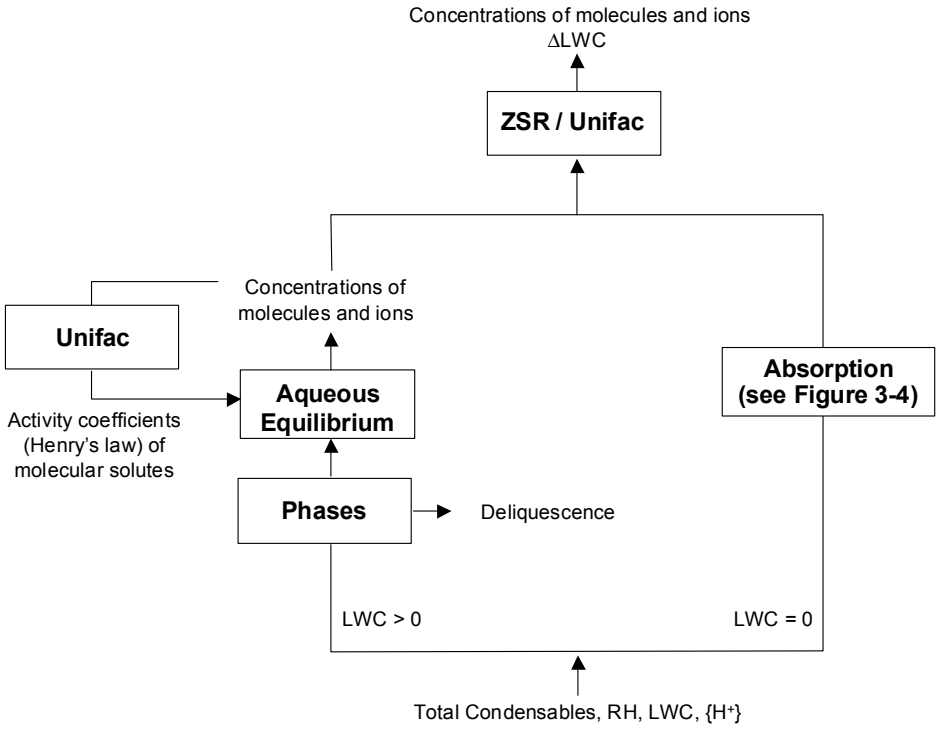

Figure 3-2
Hydrophilic module flow diagram.

The activity of a species is calculated as the product of its concentration and the activity coefficient, which characterizes the deviation from ideality. At present, there is no satisfactory way to estimate activity coefficients in a mixed electrolyte/molecular system of organic and inorganic solutes. Therefore, organic-inorganic interactions are not modeled in the activity calculations. Of the methodologies available to calculate activity coefficients of organic compounds, UNIFAC is the most versatile, because it requires only properties of functional groups within the molecule and no molecule-specific experimental data (such data are not available for many of the complex organic compounds present in the atmosphere). The UNIFAC method is used to estimate the activity coefficients of both molecular organic solutes and organic ions in the hydrophilic module. A globally convergent Newton/line search method (Press et al., 1992) is used to solve the system of partition equations.

Organic solutes that partition into the particulate phase are associated with additional water. Two options are provided to calculate the water associated with organic compounds: (1) the ZSR equation can be used to determine the additional water based on UNIFAC-generated data on binary solutions of the solutes in water or (2) UNIFAC can be used to determine the concentration of particulate water such that its activity equals the ambient relative humidity.

When the relative humidity is below the deliquescence point of an organic compound, that compound does not dissolve in the existing aqueous phase and is not associated with additional water.

If no water is associated with inorganic compounds, organic compounds may still partition into the particulate phase if they dissolve into an organic-phase solution. The formation of organic-phase liquid aerosols follows the absorption theory used in the hydrophobic subroutine (discussed below). Additional water may be associated with the hydrophilic compounds that enter the particulate phase through absorption.

Hydrophilic compounds dissolve into an aqueous phase that also contains inorganic species such as sodium, ammonium, sulfate, nitrate, and chloride. Computationally, the aqueous organic aerosol module interacts with the inorganic aerosol module (i.e., ISORROPIA) to calculate the pH and liquid water content (LWC) of the aqueous particles (see Figure 3-3). In EPRI (1999), a procedure to link the hydrophilic organic aerosol module with SCAPE2 was presented. Due to its superior computational stability, ISORROPIA is used in CMAQ-MADRID. ISORROPIA (version 1.5) accounts for the effect of organic anions in the charge balance equation, the increased liquid water content associated with organic solutes, and the effect of the additional anions on the ionic strength of the solution (a parameter used in calculating the activity coefficient of inorganic ions).

3.3.2 Partitioning of Hydrophobic Compounds

Hydrophobic surrogate compounds are absorbed into an organic phase, which contains both primary and secondary components. The absorption equation is as follows.

$$K_i = \frac{A_i}{\left(M_0 + \sum_j A_j \right) G_i} \tag{3-6}$$

where K_i ($m^3/\mu g$) is the partition coefficient between the gas and particle phases, A_i is the mass concentration in the particle phase ($\mu g/m^3$ air), G_i is the mass concentration in the gas phase ($\mu g/m^3$ air), and M_0 is the mass concentration ($\mu g/m^3$ air) of primary organic compounds that form a part of the absorbing organic medium. The primary organic matter in the absorbing medium is represented by five surrogate compounds, including saturated and unsaturated fatty acids, substituted phenols, long-chain alkanes, and aromatic dicaboxylic acids. K_i depends on the characteristics of the partitioning compound as well as those of the organic mixture in the particulate phase. Pankow's (1994) formula is used for K_i (Equation 3-2). A globally convergent Newton/line search method (Press et al., 1992) is used to solve the system of partition equations. The design of the hydrophobic module is shown in Figure 3-4.

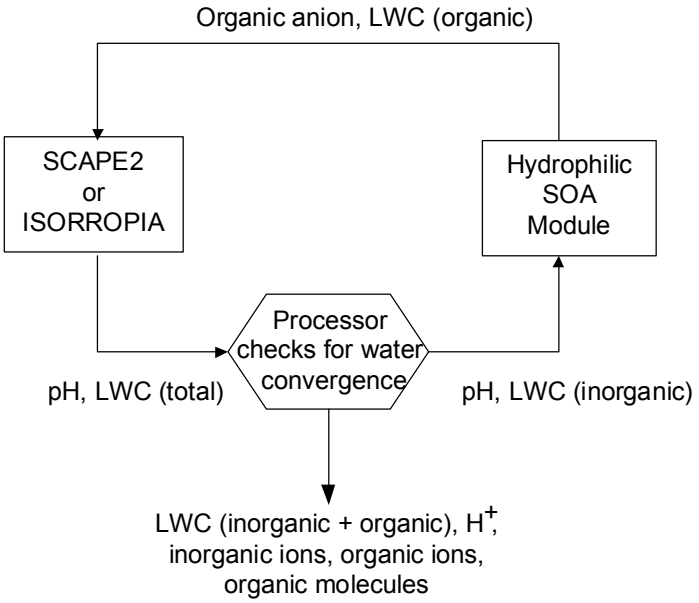

Figure 3-3
Flow chart of the iterative procedure used to solve the hydrophilic SOA-inorganic system.

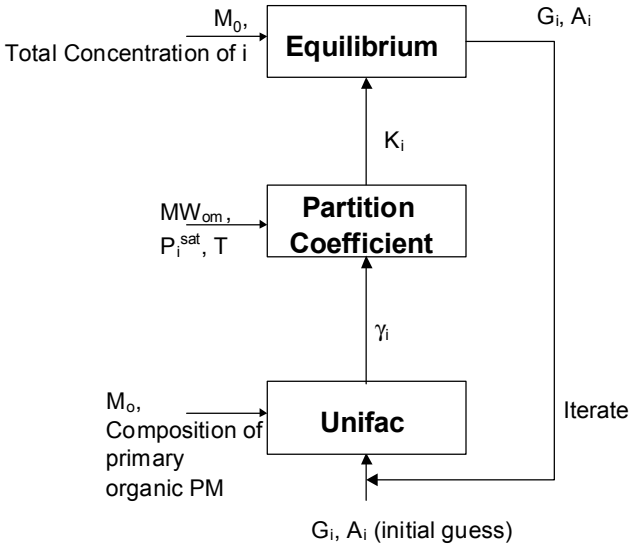

Figure 3-4
Hydrophobic SOA module flow diagram.

3.3.3 Coupling of the AEC Module with CACM

In its current implementation, the AEC module simulates the partition of five hydrophilic and five hydrophobic surrogate compounds that represent 42 organic condensable species produced in the Caltech Atmospheric Chemistry Mechanism (CACM) (Griffin et al., 2002).

The condensable compounds of CACM are classified as hydrophilic or hydrophobic. Hydrophilic compounds have (1) a short carbon chain (≤ 7 carbons; or ≤ 10 carbons with three or more functional groups), (2) high solubility (≥ 1 g solute / 100 g water), and (3) a high effective Henry's law constant ($H^* \geq 1 \times 10^6$ M atm^{-1}). Hydrophobic compounds are identified by their estimated octanol-water partition coefficient (K_{ow}) values. Many of the aromatic acid compounds are associated with sufficiently high H* and solubilities to partition into the aqueous phase, according to the H* and solubility criteria set forth by Saxena and Hildemann (1996). However, K_{ow} estimates indicate that these aromatic compounds are moderately hydrophobic and they are, therefore, assigned to the hydrophobic group.

Next, the 14 hydrophilic and 28 hydrophobic compounds of CACM are grouped into subgroups based on their origins, i.e., whether they are anthropogenic or biogenic. For hydrophilic compounds, three surrogates are used to represent anthropogenic compounds based on dissociative properties and molecular weight (MW): dissociative and low MW, dissociative and high MW, non-dissociative. There are two surrogates, dissociative and non-dissociative, for biogenic hydrophilic compounds. Anthropogenic hydrophobic compounds are represented by four surrogates, which are benzene-based, nathphalene-based, or aliphatic. The benzene-based category is further divided into high and low vapor pressure compounds. There is only one biogenic hydrophobic surrogate compound and it is aliphatic in nature. In addition to surrogate secondary compounds, the model is also set up for butanedioic acid, a chemically inert hydrophilic species that may be present as a primary aerosol component.

Each surrogate compound is assigned a molecular structure that represents an "average" structure of the compounds that it represents (see Figure 3-5). Thermodynamic properties of the surrogate compounds are defined as follows. Henry's law constants and saturation vapor pressures are estimated for individual condensing compounds using group contribution methods (Drefahl and Reinhard, 1995). The property of the surrogate compound is the mean value of the properties of the individual compounds. Acid dissociation constants and deliquescence relative humidity are assigned by analogy due to the lack of experimental data and estimation methods. Activity coefficients of the surrogate compounds are estimated using UNIFAC based on the surrogate structure.

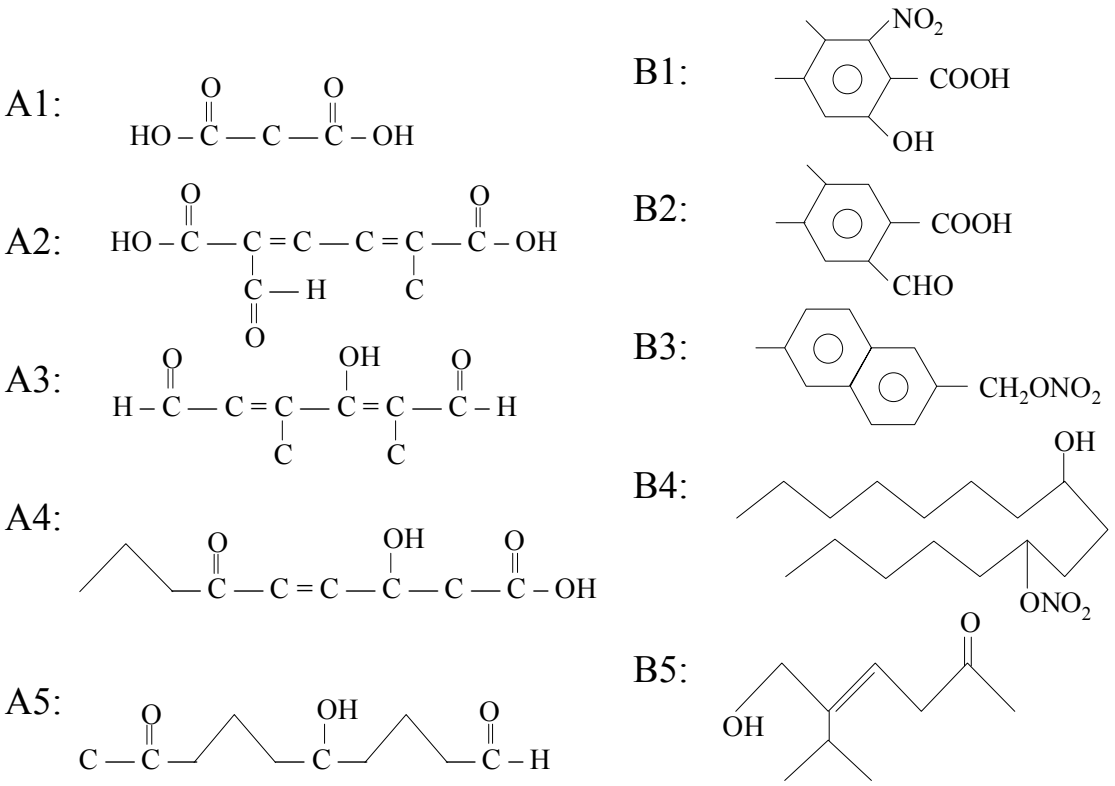

Figure 3-5
Surrogate structures modeled in MADRID 2. Compounds A1 through A5 are hydrophilic; compounds B1 through B5 are hydrophobic. Compounds A1 through A3 and B1 through B4 are of anthropogenic origin. Compounds A4, A5 and B5 are of biogenic origin.

4
AEROSOL DYNAMICS

4.1 Particle Size Distribution

The simulation of aerosol dynamics consists in representing the processes that govern the particle size distribution. Two major approaches have been used to represent the particle size distribution: the modal approach and the sectional approach. In the modal approach, the particle size distribution is represented by several modes (e.g., Aitken nuclei, accumulation and coarse modes) and an analytical function (typically, a lognormal distribution) is used to represent the particle size distribution of each mode. The aerosol dynamic processes that govern the evolution of the particle size distribution can then be solved analytically. In the sectional approach, the particle size distribution is approximated by a discrete number of size sections. Some properties of the particle size distribution (e.g., mass of individual chemical species) are then assumed to be uniform within each size section and to be conserved as the aerosol general dynamic equation is solved. The modal approach is used in the original CMAQ. A sectional approach is used to represent the particle size distribution in CMAQ-MADRID. The processes that govern aerosol dynamics include coagulation, nucleation (i.e., the formation of new particles), growth due to condensation, shrinkage due to volatilization and the mass transfer of chemical species between the bulk gas phase and the particle surface.

Coagulation can be neglected under most circumstances because its time scales are long compared to those of other processes such as condensation and its influence on the particle mass size distribution is, therefore, seldom dominant. The other processes are treated explicitly in MADRID. Note that MADRID uses the Stokes particle diameter in its formulation whereas the $PM_{2.5}$ and PM_{10} regulations use the aerodynamic diameter. These two diameters are related by the square root of the particle density. For example, for a particle density of 1.35 g/cm^3, the aerodynamic diameter of 2.5 μm corresponds to a Stokes diameter of 2.15 μm. The density of atmospheric particles typically varies between 1 g/cm^3 (density of water) and about 2 g/cm^3 (solid particles).

There are two major options to represent the particle size distribution in MADRID.

In the first option, two particle size sections are selected. The most common approach is to select two size sections that represent fine and coarse particles. In this option, particle growth by condensation and particle shrinkage by volatilization are not simulated because there is minimal exchange via growth/shrinkage between the fine and coarse particle modes. Simulating this exchange is not feasible with only two sections and a multi-sectional representation is required (see below). Also, the treatment of new particle formation is not recommended since the particle

size resolution is not sufficient to resolve ultrafine particles from fine particles (nevertheless, it can be selected by the user if desired). Therefore, gas/particle mass transfer is the only aerosol dynamic process that is relevant in the case of a two-section representation.

In the second option, a multi-sectional (i.e., more than two) representation is selected. A minimum number of eight sections is recommended to provide sufficient resolution of particle sizes for the simulation of aerosol dynamic processes to be meaningful. New particle formation, growth by condensation, shrinkage by volatilization and gas/particle mass transfer are simulated.

We describe below the formulations used in MADRID to simulate new particle formation, condensational growth (or shrinkage by volatilization) and gas/particle mass transfer.

4.2 Formation of New Particles

The algorithm of McMurry and Friedlander (1979) is used in MADRID to represent the formation of new particles based on the review of Zhang et al. (1999). Six algorithms currently used in 3-D air quality models to calculate the absolute rate of particle nucleation were compared (Zhang et al., 1999). Although all algorithms were formulated from the same theoretical basis, they gave highly variable results under typical conditions. Therefore, the use of these parameterizations of the absolute nucleation rates is associated with significant uncertainties at present. Consequently, Zhang et al. (1999) recommended the use of a method that calculates the relative rates of new particle formation and condensation on existing particles (McMurry and Friedlander, 1979) instead of calculating the absolute rate of nucleation.

Unlike other nucleation parameterizations (e.g., Pandis et al., 1994; Kerminen and Wexler, 1994; Fitzgerald et al., 1998; Harrington and Kreidenweis, 1998) in which only the absolute nucleation rates of particles are calculated, the approach of McMurry and Friedlander calculates the relative rates of new particle formation and condensation. The rate of change in the number concentration of condensable molecules is calculated as follows.

$$\frac{dN_1}{dt} = R_m - \beta_{1,1} N_1^2 - \sum_{j=2}^{k-1} \beta_{1,j} N_j N_1 - \gamma A N_1 \qquad (4\text{-}1)$$

where R_m is the production rate of condensable molecules (monomers) by gas-phase chemical reactions; N_1 is the number concentration of monomers; N_j is the number concentration of molecular clusters containing monomers of size j; k is the number of monomers at the minimum detectable particle size; A is the existing particle surface area per volume of gas for particles of size k and larger; γ, $\beta_{1,1}$, and $\beta_{1,j}$ are collision coefficients for collisions among monomers, between monomers and molecular clusters, and between monomers and existing particles larger than size k-1, respectively. They can be calculated based on kinetic theory. The second term on the right hand side of Equation 4-1 is the rate at which monomers collide with themselves, and the third term is the rate at which they collide with molecular clusters formed by nucleation. The fourth term is the rate at which monomers are lost by condensation on particles larger than size k-1. Two major assumptions are used to derive the above equation: (1) condensable molecules

stick to other condensable molecules, clusters, or particles with which they collide; and (2) reevaporation from clusters and particles is slow compared with the rate of condensational growth. These assumptions are appropriate for sulfuric acid.

The rate of change in the number concentrations of molecular clusters is calculated as follows.

$$\frac{dN_j}{dt} = \beta_{1,j-1} N_1 N_{j-1} - \beta_{1,j} N_1 N_j - \frac{\gamma A}{\sqrt{j}} N_j \tag{4-2}$$

The first term on the right hand side of Equation 4-2 is the rate at which monomers collide with molecular clusters of size *j*-1 to form molecular clusters of size *j*, the second term is the rate at which molecular clusters of size *j* collide with monomers. The third term is the rate at which molecular clusters are lost by condensation on particles larger than size *k*-1. Two major assumptions are used to derive the above equation: (1) the concentrations of molecular clusters are present in quasi-steady state (typically achieved on a time scale of minutes); and (2) collisions between molecular clusters can be ignored (because of their very low rate of collision compared to collision with monomers or large particles). Only the condensation of monomers on clusters and scavenging of clusters by large particles are considered.

The rate of formation of new particles of size *k*, $G(k)$, is calculated as follows.

$$G(k) = \beta_{1,k-1} N_1 N_{k-1} \tag{4-3}$$

Equation 4-3 can be expressed in the following dimensionless form.

$$\frac{G(k)}{R} = c_{k-1} L \tilde{N}_{k-1} \tilde{N}_1 \tag{4-4}$$

where $c_{k\text{-}1} = \beta_{1,k\text{-}1}/\beta_{1,1}$, and $\tilde{N}_1$ and $\tilde{N}_{k\text{-}1}$ are the dimensionless monomer and cluster concentrations, respectively. They can be calculated from N_1 and N_j, respectively, as follows.

$$\tilde{N}_j = \frac{\beta_{1,1}}{\gamma A} N_j \tag{4-5}$$

L is the product of two ratios at steady state: $\gamma A\, N_1/R$, which is the ratio of the rate at which monomers collide with pre-existing particles to the rate at which they are produced, and $\gamma A\, N_1/\beta_{1,1}\, N_1^2$, which is the ratio of the rate at which monomers collide with pre-existing particles to the rate at which they collide with themselves. The former ratio has a maximum value of 1, which occurs when new particle formation is completely suppressed. When the latter ratio is large compared to 1, heterogeneous condensation dominates. The relative importance of nucleation and condensation can therefore be determined by the magnitude of *L*. McMurry and Friedlander (1979) reported a value of 0.1 as a threshold value for *L*, below which new particle formation is important, and above which condensation on pre-existing particles dominates.

The parameter L is a key parameter in the nucleation theory of McMurry and Friedlander (1979) because the dimensionless rate of particle formation depends on L, $\tilde{N}_1$ and $\tilde{N}_{k\text{-}1,}$ and the latter two variables in turn depend only on L. By definition, L can be calculated as follows.

$$L = \frac{\gamma A N_1}{R_m} \frac{\gamma A N_1}{\beta_{1,1} N_1^2} = \frac{1}{16\sqrt{3}\pi} \left(\frac{4\pi}{3}\right)^{1/6} \frac{(k_b T)^{1/2} A^2}{\upsilon_1^{7/6} \rho^{1/2} R_m} \tag{4-6}$$

where k_b is the Boltzmann's constant, T is temperature, ρ is the particle density, and υ_1 is the molecular volume of monomers. Assuming that steady state monomer concentrations can be established on a time scale of minutes, L can be derived from Equation 4-1.

$$L = \frac{1}{\tilde{N}_1^2 + \tilde{N}_1 + \sum_{j=2}^{k-1} c_i \tilde{N}_1 \tilde{N}_j} \tag{4-7}$$

Assuming that the cluster concentrations are in a quasi-steady state, a relationship between $\tilde{N}_j$ and $\tilde{N}_1$ can be derived from Equation 4-2.

$$\frac{\tilde{N}_j}{\tilde{N}_1} = \prod_{i=2}^{j} \frac{c_{i-1} \tilde{N}_1}{c_i \tilde{N}_1 + \frac{1}{\sqrt{i}}} \tag{4-8}$$

Substituting Equation 4-8 into Equation 4-7 for cluster concentrations, a relationship between L and $\tilde{N}_1$ can be obtained. However, since L is not an explicit function of $\tilde{N}_1$, numerical iteration is needed to solve Equations 4-6 and 4-7. In MADRID, an initial concentration of N_1 has to be assumed. $\tilde{N}_1$, $\tilde{N}_{k\text{-}1,}$ and the corresponding L are then calculated according to Equations 4-5, 4-8 and 4-7, respectively. This calculated value of L is compared to the value of L calculated based on Equation 4-6. If the difference between the two L values is within the given error tolerance, the assumed N_1 and the calculated $N_{k\text{-}1}$ are used to calculate the rate of new particle formation, $G(k)$. The number concentrations of the newly-formed particles are then converted to the equivalent number concentrations of particles with the lower diameter of the smallest particle size section and added to that section.

The new particle parameterization of McMurry and Friedlander (1979) is computationally demanding because it involves iteration among Equations 4-5 through 4-8. Consequently, a parameterized version that uses a look-up table with precalculated rates for given values of L and k is used as the default option in CMAQ-MADRID. Figure 4-1 depicts this parameterization where the relative rate of new particle formation (i.e., ratio of new particle formation rate and total gas-to-particle conversion rate) is presented as a function of L (see Equation 4-7) and k. The value of k (number of H_2SO_4 molecules in a new particle) depends on the lowest diameter of the modeled particle size distribution ($d_{p,min}$ and relative humidity (RH)). For example, k=1900 for $d_{p,min}$=0.01 μm and RH=50%. New particle formation becomes negligible for L>0.1.

An option for neglecting the calculation of new particle formation (e.g., in the case of a two-section representation) is provided in CMAQ-MADRID.

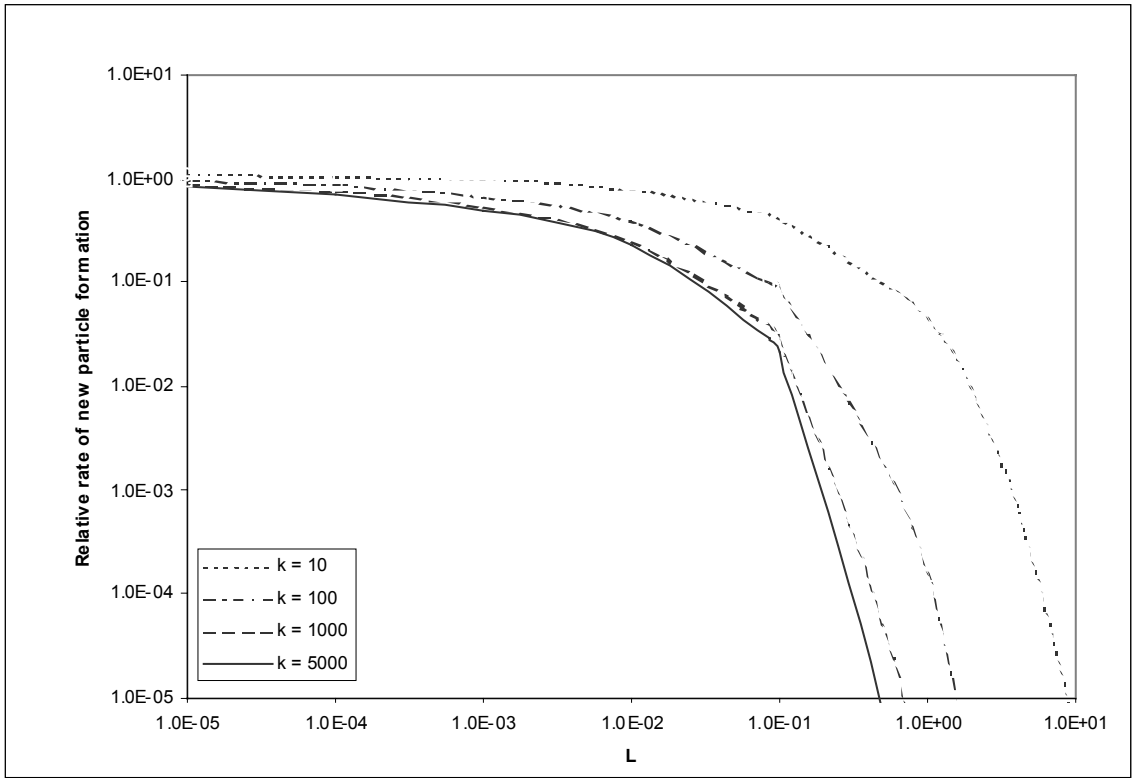

Figure 4-1
Parameterized ratio of new particle formation rate to total gas-to-particle conversion rate as a function of *L* and *k* (see text for details).

4.3 Condensational Growth

The simulation of growth by condensation or shrinkage by volatilization is challenging with a sectional representation because, in 3-D simulations, it typically leads to numerical diffusion. Three basic approaches have been used to simulate condensational growth:

(1) Semi-Lagrangian techniques that calculate the mass (or number) flux from one section to the next. The basic finite-difference method (e.g., Seigneur, 1982) is the simplest example of a semi-Lagrangian technique. Bott's scheme (Bott, 1989), the scheme of Chock and Winkler (2000) and that of Nguyenand Dabdub (2002) are more advanced examples of semi-Lagrangian techniques.

(2) Lagrangian techniques that calculate the movement of the section boundaries according to the growth law and redistribute the resulting sectional distribution onto the fixed sectional representation. The UAM-AERO scheme (Lurmann et al., 1997) is an example of a Lagrangian technique where a spline function is used for the redistribution of the sectional representation.

(3) The moving-center technique of Jacobson (Jacobson and Turco, 1995; Jacobson, 1997a) where the diameter representative of the section moves according to the growth law. Mass is transferred between sections only when the section representative diameter reaches one of the section boundaries (i.e., the equivalent of an Eulerian technique since transfer of mass between sections is minimized).

Semi-Lagrangian and Lagrangian techniques were shown to lead to significant numerical diffusion and among the algorithms tested, the moving center approach appeared to be the most accurate (Zhang et al., 1999).

Consequently, the moving-center technique is used to simulate condensational growth in MADRID. In the moving-center technique, the diameter representation of the particle size section moves according to the increase (or decrease) in mass within the section. Note that this process is simulated only when more than two particle size sections are selected by the user.

The following growth law is used in MADRID (Capaldo et al., 2000) to simulate the flux between the gas phase and particles,

$$J_{i,j} = 2\pi d_p D_{gi} N_j \left(C_{\infty,i} - C_{si,j}\right) \frac{1 + K_{n_{i,j}}}{1 + 2K_{n_{i,j}} \frac{\left(1 + K_{n_{i,j}}\right)}{\alpha_{i,j}}} \qquad (4\text{-}9)$$

where $J_{i,j}$ is the growth/evaporation rate of species i in a particle in section j, $d_{p,j}$ is the characteristic diameter of particles in section j, N_j is the number density of particles in section j, D_{gi} is the molecular diffusivity of species i in air, $C_{\infty,i}$ is the concentration of species i in the bulk gas phase, $C_{si,j}$ is the concentrations of species i at the surface of particles in section j, $K_{ni,j} = 2\lambda/d_p$, λ is the air mean free path, and $\alpha_{i,j}$ is the accommodation coefficient for species i on the particle in section j, a value of $\alpha_{i,j} = 0.1$ is used for all species and all sections.

Each section center moves according to the change in mass in the section, increasing in the case of condensation and decreasing in the case of volatilization. As a section center reaches one of the boundaries of the section (upper boundary in the case of condensation; lower boundary in the case of volatilization), the particulate mass contained in that section moves into the next section. Then, a new section center is calculated for that next section as the weighted (by mass) average of the previous center of that section and of the center that moved from the lower section. This technique minimizes numerical diffusion since particulate mass is transferred from one section to the next only in the case where a section center reaches one of the section boundaries.

It is important to note that this technique allows the simultaneous tracking of particulate mass and particulate number. Only one variable, typically particulate mass, can be tracked in sectional representations that use a fixed section center.

The mass and number concentrations in a given section j (m_j and n_j, respectively) are related through the following equation.

$$n_j = \frac{6m_j}{\pi (d_{p,j})^3 \rho_p} \tag{4-10}$$

where ρ_p is the density of the particle.

In a three-dimensional air quality model, one must account for mixing PM populations within a given grid cell via advection, turbulent diffusion, convection, emissions and sedimentation. For a given size section, PM populations that are mixed within a grid cell are likely to originally have different section centers. An initial particle size distribution is assumed for newly-emitted particles. Since the changes in both mass and number concentrations of particles due to various atmospheric processes (e.g., emission, advection, turbulent diffusion, and nucleation) are explicitly treated in CMAQ-MADRID, the new common section center for the mixed particles in a given size section is calculated using the particle mass and number concentrations in the same size section, namely,

$$d_{p,j} = \sqrt[3]{\frac{6m_j}{\pi \cdot n_j \cdot \rho_p}} \tag{4-11}$$

4.4 Gas/Particle Mass Transfer

Particles are not always at equilibrium with the gas phase. The time scale for the diffusion of a molecule from the bulk gas phase to the surface of a particle increases with the diameter of the particle. Therefore, fine particles will tend to reach equilibrium rapidly whereas coarse particles can remain in non-equilibrium conditions (Wexler and Seinfeld, 1990; Dassios and Pandis, 1999). Algorithms that treat the mass transfer between the bulk gas phase and particles explicitly are computationally demanding. On the other hand, assuming full gas/particle equilibrium can lead to erroneous results if coarse particles play an active role in the chemical composition of the particulate phase. This will be the case, for example, when coarse sea salt particles and alkaline dust particles react with acidic gases such as HNO_3 and H_2SO_4. An hybrid approach that offers compromise between accuracy and computational efficiency is therefore desirable.

Two hybrid approaches are used in MADRID: the CIT hybrid approach of Meng et al. (1998) and the CMU hybrid approach of Capaldo et al. (2000). The CIT hybrid approach assumes full equilibrium between the bulk gas phase and the bulk particulate phase but distributes the condensing mass according to a growth law that depends on particle size. The CMU hybrid approach consists in treating mass transfer explicitly for the coarse particles and assuming gas/particle equilibrium for the fine particles. It has been modified for its implementation in MADRID as discussed below.

The CMU hybrid approach treats mass transfer explicitly for particles above a certain threshold size and assumes full equilibrium for particles below that threshold size. We tested two Stokes diameters of 1 μm and 2.15 μm as threshold sizes. 1 μm was the original recommendation of Capaldo et al. (2000) and 2.15 μm was used to increase computational efficiencies of the model. The maximum difference in PM concentrations in a given size section obtained between these two simulations was only 3%. Therefore, it appears that a suitable compromise between computational efficiency and accuracy can be obtained for a Stokes diameter of 2.15 μm. A threshold value of 2.15 μm is used when two or eight size sections are selected in MADRID. For a different section number and/or distribution, a section cut off size between 1 and 2.15 μm should be selected by the user to be the threshold value.

For particles in size sections above the threshold value in diameter, the mass transfer equation is solved according to the growth law of Equation 4-9 (Capaldo et al., 2000).

The chemical concentration $C_{si,j}$ is calculated by solving the gas/particle thermodynamic equilibrium knowing the particulate chemical concentrations. This calculation is conducted using ISORROPIA (see Section 3). If the bulk gas-phase chemical concentration exceeds the concentration at the surface of the particle, the mass transfer occurs from the bulk gas phase toward the particle, and vice-versa. The mass transfer and thermodynamic equilibrium equations are solved iteratively until convergence is attained.

For particles in size sections below 2.15 μm in diameter, mass transfer is assumed to be instantaneous.

$$C_{si,j} = C_{\infty,i} \tag{4-12}$$

Thus, ISORROPIA is used to calculate the bulk particulate chemical concentrations knowing the bulk gas-phase chemical concentrations. The material transferred between phases is distributed over the fine particle size sections by using weighting factors, w_j, for section j that are defined according to the growth law given in Equation 4-13.

$$w_j = \frac{N_j d_{p,j}}{1 + \dfrac{\lambda}{\alpha_{i,j} d_{p,j}}} \tag{4-13}$$

As chemical species either condense to or volatize from the particles, these particles grow or shrink accordingly. Therefore, in the case where more than two sections are selected, the hybrid mass transfer algorithm must be coupled with a growth/shrinkage algorithm. The original formulation of the mass transfer algorithm of Capaldo et al. (2000) uses a finite difference scheme to treat growth/shrinkage of the particles. As discussed in Section 4.3, such schemes can lead to numerical diffusion. Therefore, the moving-center algorithm described in Section 4.3 is used in CMAQ-MADRID.

The user can also select the option where full equilibrium (i.e., Equation 4-12) applies to all size sections. This option is computationally more efficient than the hybrid mass transfer option and is appropriate if concentrations of coarse sea salt and alkaline dust particles are low.

5
CLOUD PROCESSES

The treatment of cloud processes in CMAQ-MADRID differs from that in the original formulation of CMAQ as follows. First, a comprehensive aqueous-phase chemical kinetic mechanism is used for cloud chemistry. Second, the treatment of aerosols in cloud, which includes particle activation and scavenging as well as particle formation from droplet evaporation, is based on a sectional representation of the particle size distribution. We describe the formulations of these processes below.

5.1 Aqueous-Phase Chemistry

The aqueous-phase chemical kinetic mechanism available in CMAQ is the RADM mechanism; it includes five reactions for the oxidation of SO_2 to sulfate. CMAQ-MADRID offers as an option a more comprehensive chemical kinetic mechanism. Santos et al. (1999) reviewed four aqueous-phase chemical mechanisms:

- RADM, the mechanism currently in Models-3/CMAQ (Walcek and Taylor, 1986)
- the aqueous chemistry module of the plume model ROME (Seigneur and Saxena, 1984, 1988)
- MatChM, a detailed mechanism that uses LSODE for its numerical solution (Zhang et al., 1998)
- the Carnegie-Mellon University (CMU) mechanism, another detailed mechanism that uses VODE for its numerical solution (Strader et al., 1998)

The requirements for the aqueous-phase chemistry module of CMAQ-MADRID were (1) a robust and efficient numerical solver and (2) a relatively complete representation of the aqueous chemistry of sulfur and nitrogen species. Because the solubility of SO_2 and the oxidation rates of dissolved SO_2 species depend on the acidity of the cloud or fog droplet, the selected aqueous chemistry mechanism needs to include a fairly long list of species that can affect the acidity of atmospheric droplets. Santos et al. (1999) concluded that the formulations of the two detailed mechanisms were appropriate and that the CMU mechanism was preferable because it was computationally more efficient. Consequently, the Carnegie Mellon University (CMU) Cloud Chemistry Mechanism (Strader et al., 1998), hereafter referred to as the CMU mechanism, is used in CMAQ-MADRID. This mechanism was originally developed by Seinfeld and Pandis (1998) and later modified at Carnegie-Mellon University (CMU) by Strader et al. (1998). The CMU mechanism includes 17 gas-aqueous equilibrium reactions, 17 aqueous equilibrium reactions, and 99 aqueous-phase kinetic reactions among 18 gas-phase species and 27 aqueous-

phase species. Like all available aqueous-phase mechanisms, it is designed to simulate sulfate production from SO_2 in atmospheric liquid water and includes the three dominant pathways for S(IV) oxidation: hydrogen peroxide, ozone, and oxygen catalyzed by iron and manganese. In addition, it includes other reactions for the oxidation of S(IV) to sulfate, the oxidation of nitrogen species to nitrate, and reactions for carbonate, chlorine, organic and oxygen species that are involved in the formation of sulfate and/or nitrate species. The scope of the mechanism is summarized in the following tables.

- Table 5-1 lists the aqueous-phase and gas-phase species, along with their treatment, in the CMU module.
- Table 5-2 lists the Henry's law constants for the gaseous species considered in the CMU module.
- Table 5-3 lists the aqueous-phase dissociation or equilibrium reactions included in the CMU mechanism.
- Table 5-4 lists the aqueous-phase kinetic reactions included in the CMU mechanism. These are separated into oxygen-hydrogen reactions, carbonate reactions, chlorine reactions, nitrite and nitrate reactions, organic reactions, and sulfur reactions. Note that, in addition to the 99 kinetic reactions activated in the CMU mechanism, Table 5-4 includes 10 reactions representing the aqueous-phase chemistry of CH_3OOH, CH_3OH, and $CH_3C(O)OOH$. These reactions, although included in the CMU computer code, are believed to be minor and are deactivated to improve computational efficiency by setting the concentrations of the above 3 species to zero.

Table 5-1
Species included in the CMU aqueous-phase chemistry module[(a)].

Aqueous-Phase Species	Treatment	Gas-Phase Species	Treatment
S(IV)	Kinetic	SO_2	Kinetic
S(VI)	Kinetic	H_2SO_4	Dissolution
N(III)	Henry's law	HNO_2	Henry's law
N(V)	Kinetic	HNO_3	Dissolution
CO_2	Henry's law	CO_2	Constant
H_2O_2	Kinetic	H_2O_2	Kinetic
HCHO	Kinetic	HCHO	Henry's law
HCOOH	Kinetic	HCOOH	Henry's law
NO	Constant	NO	Constant
NO_2	Constant	NO_2	Constant
O_3	Constant	O_3	Constant
PAN	Constant	PAN	Constant
HCl	Kinetic	HCl	Dissolution
OH	Steady-state	OH	Steady-state
HO_2	Steady-state	HO_2	Steady-state
NO_3	Steady-state	NO_3	Steady-state
NH_3	Kinetic	NH_3	Kinetic
CH_3O_2	Constant	CH_3O_2	Constant
$ClOH^-$	Steady-state		
SO_4^-	Steady-state		
SO_5^-	Steady-state		
HSO_5^-	Kinetic		
HMSA	Kinetic		
CO_3^-	Steady-state		
Na^+	Constant		
Fe^{3+}	Constant		
Mn^{2+}	Constant		

(a) Kinetic: concentration is solved as a function of time; Henry's law: gas/droplet partitioning is calculated; constant: initial gas-phase concentration is used to calculate aqueous-phase concentration without gas/droplet repartitioning because of low solubility; steady-state: concentrations are calculated from other species concentrations assuming steady state; dissolution: species is assumed to be totally in the aqueous phase.

Table 5-2
Henry's law constants for the gaseous species considered in the CMU aqueous-phase chemistry module.

Gas-Phase Species[a]	Henry's Law Constant ($M\ atm^{-1}$, at 298 K)[b]
SO_2	1.23
HNO_2	49
HNO_3	2.1×10^5
CO_2	3.4×10^{-2}
H_2O_2	7.45×10^4
HCHO[c]	2.5
HCOOH	3.5×10^3
NO	1.9×10^{-3}
NO_2	1.0×10^{-2}
O_3	1.13×10^{-2}
PAN	2.9
HCl	727
OH	25
HO_2	2.0×10^3
NO_3	2.1×10^5
NH_3	75
CH_3O_2[d]	6

[a] The values given reflect only the physical solubility of the gas regardless of the subsequent fate of the dissolved species. The above constants do not account for dissociation or other aqueous-phase transformations. See Table 2-3 for the dissociation reactions.

[b] For data on the temperature dependence of these constants, see Pandis and Seinfeld (1989).

[c] Formaldehyde, upon dissolution in water, undergoes hydrolysis to yield the gem-diol, methylene glycol.

$HCHO\ (aq) + H_2O \leftrightarrow H_2C(OH)_2\ (aq)$

If this reaction is included, the effective Henry's law constant of formaldehyde becomes 6.3×10^3 (Seinfeld and Pandis, 1998). The mechanism implemented here includes the effect of this reaction.

[d] For the SAPRC chemical mechanism, the total alkyl peroxy radicals (RO2) can be used as an upper-limit estimate of CH_3O_2. For the CB-IV mechanism, the CH_3O_2 concentration is estimated as the sum of the XO_2 and TO_2 radicals.

Table 5-3
Equilibrium reactions included in the CMU aqueous-phase chemical mechanism.

Equilibrium Reaction	$K_{298}(M \text{ or } M\ atm^{-1})^a$	$-\Delta H / R(K)$
$SO_2 \cdot H_2O \leftrightarrow HSO_3^- + H^+$	1.23 x 10^{-2}	1960
$HSO_3^- \leftrightarrow SO_3^{2-} + H^+$	6.61 x 10^{-8}	1500
$H_2SO_4(aq) \leftrightarrow HSO_4^- + H^+$	1000	
$HSO_4^- \leftrightarrow SO_4^{2-} + H^+$	1.02 x 10^{-2}	2720
$H_2O_2(aq) \leftrightarrow HO_2^- + H^+$	2.2 x 10^{-12}	-3730
$HNO_3(aq) \leftrightarrow NO_3^- + H^+$	15.4	8700[b]
$HNO_2(aq) \leftrightarrow NO_2^- + H^+$	5.1 x 10^{-4}	-1260
$CO_2 \cdot H_2O \leftrightarrow HCO_3^- + H^+$	4.46 x 10^{-7}	-1000
$HCO_3^- \leftrightarrow CO_3^{2-} + H^+$	4.68 x 10^{-11}	-1760
$NH_4OH \leftrightarrow NH_4^+ + OH^-$	1.75 x 10^{-5}	-450
$H_2O \leftrightarrow H^+ + OH^-$	1.0 x 10^{-14}	-6710
$HCHO(aq) \overset{H_2O}{\leftrightarrow} H_2C(OH)_2(aq)$	1.82 x 10^{3}	4020
$HCOOH(aq) \leftrightarrow HCOO^- + H^+$	1.78 x 10^{-4}	-20
$HCl(aq) \leftrightarrow H^+ + Cl^-$	1.74 x 10^{6}	6900
$Cl_2^- \leftrightarrow Cl + Cl^-$	5.26 x 10^{-6}	
$HO_2(aq) \leftrightarrow H^+ + O_2^-$	3.50 x 10^{-5}	
$HOCH_2SO_3^- \leftrightarrow {}^-OCH_2SO_3^- + H^+$	2.00 x 10^{-12}	

[a] The temperature dependence is represented by

$$K = K_{298} \exp\left[\frac{-\Delta H}{R}\left(\frac{1}{T} - \frac{1}{298}\right)\right]$$

where *K* is the equilibrium constant at temperature *T* (in K).

[b] Value for equilibrium: $HNO_3(g) \leftrightarrow NO_3^- + H^+$.

Table 5-4
Kinetic reactions included in the CMU aqueous-phase chemical mechanism.

Oxygen-Hydrogen Chemistry			
	Reaction	$k_{298}{}^{a}$	$-E/R(K)$
1.	$H_2O_2 \xrightarrow{h\nu} 2\,OH$	e	
2.	$O_3 \xrightarrow{h\nu, H_2O} H_2O_2 + O_2$	e	
3.	$OH + HO_2 \rightarrow H_2O + O_2$	7.0×10^{9}	-1500
4.	$OH + O_2^- \rightarrow OH^- + O_2$	1.0×10^{10}	-1500
5.	$OH + H_2O_2 \rightarrow H_2O + HO_2$	2.7×10^{7}	-1700
6.	$HO_2 + HO_2 \rightarrow H_2O_2 + O_2$	8.6×10^{5}	-2365
7.	$HO_2 + O_2^- \xrightarrow{H_2O} H_2O_2 + O_2 + OH^-$	1.0×10^{8}	-1500
8.	$O_2^- + O_2^- \xrightarrow{2H_2O} H_2O_2 + O_2 + 2OH^-$	<0.3	
9.	$HO_2 + H_2O_2 \rightarrow OH + O_2 + H_2O$	0.5	
10.	$O_2^- + H_2O_2 \rightarrow OH + O_2 + OH^-$	0.13	
11.	$OH + O_3 \rightarrow HO_2 + O_2$	2×10^{9}	
12.	$HO_2 + O_3 \rightarrow OH + 2\,O_2$	$<1\times10^{4}$	
13.	$O_2^- + O_3 \xrightarrow{H_2O} OH + 2\,O_2 + OH^-$	1.5×10^{9}	-1500
14.	$OH^- + O_3 \xrightarrow{H_2O} O_2^- + HO_2$	70	
15.	$HO_2^- + O_3 \rightarrow OH + O_2^- + O_2$	2.8×10^{6}	-2520
16.	$H_2O_2 + O_3 \rightarrow H_2O + 2\,O_2$	$7.8\times10^{-3}[O_3]^{-0.5}$	

Table 5-4
Kinetic reactions included in the CMU aqueous-phase chemical mechanism. (continued)

Carbonate Chemistry			
	Reaction	k_{298}	$-E/R\ (K)$
17.	$HCO_3^- + OH \rightarrow H_2O + CO_3^-$	1.5×10^7	-1910
18.	$HCO_3^- + O_2^- \rightarrow HO_2^- + CO_3^-$	1.5×10^6	0
19.	$CO_3^- + O_2^- \xrightarrow{H_2O} HCO_3^- + O_2 + OH^-$	4.0×10^8	-1500
20.	$CO_3^- + H_2O_2 \rightarrow HO_2 + HCO_3^-$	8.0×10^5	-2820

Chlorine Chemistry			
	Reaction	k_{298}	$-E/R(K)$
21.	$Cl^- + OH \rightarrow ClOH^-$	4.3×10^9	-1500
22.	$ClOH^- \rightarrow Cl^- + OH$	6.1×10^9	0
23.	$ClOH^- \xrightarrow{H^+} Cl + H_2O$	$2.1\times10^{10}[H^+]$	0
24.	$Cl \xrightarrow{H_2O} ClOH^- + H^+$	1.3×10^3	0
25.	$HO_2 + Cl_2^- \rightarrow 2\ Cl^- + O_2 + H^+$	4.5×10^9	-1500
26.	$O_2^- + Cl_2^- \rightarrow 2\ Cl^- + O_2$	1.0×10^9	-1500
27.	$HO_2 + Cl \rightarrow Cl^- + O_2 + H^+$	3.1×10^9	-1500
28.	$H_2O_2 + Cl_2^- \rightarrow 2\ Cl^- + HO_2 + H^+$	1.4×10^5	-3370
29.	$H_2O_2 + Cl \rightarrow Cl^- + HO_2 + H^+$	4.5×10^7	0
30.	$OH^- + Cl_2^- \rightarrow 2\ Cl^- + OH$	7.3×10^6	-2160

Table 5-4
Kinetic reactions included in the CMU aqueous-phase chemical mechanism. (continued)

Nitrite and Nitrate Chemistry			
	Reaction	k_{298}	$-E/R(K)$
31.	$NO + NO_2 \xrightarrow{H_2O} 2\ NO_2^- + 2H^+$	2.0×10^8	-1500
32.	$NO_2 + NO_2 \xrightarrow{H_2O} NO_2^- + NO_3^- + 2\ H^+$	1.0×10^8	-1500
33.	$NO + OH \rightarrow NO_2^- + H^+$	2.0×10^{10}	-1500
34.	$NO_2 + OH \rightarrow NO_3^- + H^+$	1.3×10^9	-1500
35.	$HNO_2 \xrightarrow{h\nu} NO + OH$	e	
36.	$NO_2^- \xrightarrow{h\nu, H_2O} NO + OH + OH^-$	e	
37.	$HNO_2 + OH \rightarrow NO_2 + H_2O$	1.0×10^9	-1500
38.	$NO_2^- + OH \rightarrow NO_2 + OH^-$	1.0×10^{10}	-1500
39.	$HNO_2 + H_2O_2 \xrightarrow{H^+} NO_3^- + 2\ H^+ + H_2O$	$6.3\times10^3[H^+]$	-6693
40.	$NO_2^- + O_3 \rightarrow NO_3^- + O_2$	5.0×10^5	-6950
41.	$NO_2^- + CO_3^- \rightarrow NO_2 + CO_3^{2-}$	4.0×10^5	0
42.	$NO_2^- + Cl_2^- \rightarrow NO_2 + 2\ Cl^-$	2.5×10^8	-1500
43.	$NO_2^- + NO_3 \rightarrow NO_2 + NO_3^-$	1.2×10^9	-1500
44.	$NO_3^- \xrightarrow{h\nu, H_2O} NO_2 + OH + OH^-$	e	
45.	$NO_3 \xrightarrow{h\nu} NO + O_2$	e	
46.	$NO_3 + HO_2 \rightarrow NO_3^- + H^+ + O_2$	4.5×10^9	-1500
47.	$NO_3 + O_2^- \rightarrow NO_3^- + O_2$	1.0×10^9	-1500
48.	$NO_3 + H_2O_2 \rightarrow NO_3^- + H^+ + HO_2$	1.0×10^6	-2800
49.	$NO_3 + Cl^- \rightarrow NO_3^- + Cl$	1.0×10^8	-1500

Table 5-4
Kinetic reactions included in the CMU aqueous-phase chemical mechanism. (continued)

Organic Chemistry			
	Reaction	k_{298}	$-E/R(K)$
50.	$H_2C(OH)_2 + OH \xrightarrow{O_2} HCOOH + HO_2 + H_2O$	2.0×10^{9}	-1500
51.	$H_2C(OH)_2 + O_3 \rightarrow Products$	0.1	0
52.	$HCOOH + OH \xrightarrow{O_2} CO_2 + HO_2 + H_2O$	1.6×10^{8}	-1500
53.	$HCOOH + H_2O_2 \rightarrow Product + H_2O$	4.6×10^{-6}	-5180
54.	$HCOOH + NO_3 \xrightarrow{O_2} NO_3^- + H^+ + CO_2 + HO_2$	2.1×10^{5}	-3200
55.	$HCOOH + O_3 \rightarrow CO_2 + HO_2 + OH$	5.0	0
56.	$HCOOH + Cl_2^- \xrightarrow{O_2} CO_2 + HO_2 + 2\,Cl^- + H^+$	6.7×10^{3}	-4300
57.	$HCOO^- + OH \xrightarrow{O_2} CO_2 + HO_2 + OH^-$	2.5×10^{9}	-1500
58.	$HCOO^- + O_3 \rightarrow CO_2 + OH + O_2^-$	100.0	0
59.	$HCOO^- + NO_3 \xrightarrow{O_2} NO_3^- + CO_2 + HO_2$	6.0×10^{7}	-1500
60.	$HCOO^- + CO_3^- \xrightarrow{O_2,H_2O} CO_2 + HCO_3^- + HO_2 + OH^-$	1.1×10^{5}	-3400
61.	$HCOO^- + Cl_2^- \xrightarrow{O_2} CO_2 + HO_2 + 2\,Cl^-$	1.9×10^{6}	-2600
62.	$CH_3C(O)O_2NO_2 \rightarrow NO_3^- + Products$	4.0×10^{-4}	0
63.	$CH_3O_2 + HO_2 \rightarrow CH_3OOH + O_2$	7.6×10^{5}	-3000
64.	$CH_3O_2 + O_2^- \xrightarrow{H_2O} CH_3OOH + O_2 + OH^-$	5.0×10^{7}	-1600
65.[f]	$CH_3OOH \xrightarrow{h\nu,O_2} HCHO + OH + HO_2$	[e]	
66.[f]	$CH_3OOH + OH \rightarrow CH_3O_2 + H_2O$	2.7×10^{7}	-1700
67.[f]	$CH_3OH + OH \rightarrow HCHO + HO_2 + H_2O$	4.5×10^{8}	-1500
68.[f]	$CH_3OH + CO_3^- \xrightarrow{O_2} HCHO + HO_2 + HCO_3^-$	2.6×10^{3}	-4500
69.[f]	$CH_3OH + Cl_2^- \xrightarrow{O_2} HCHO + HO_2 + H^+ + 2Cl^-$	3.5×10^{3}	-4400
70.[f]	$CH_3OOH + OH \rightarrow HCHO + OH + H_2O$	1.9×10^{7}	-1800
71.[f]	$CH_3OH + NO_3 \xrightarrow{O_2} NO_3^- + H^+ + HCHO + HO_2$	1.0×10^{6}	-2800

Table 5-4
Kinetic reactions included in the CMU aqueous-phase chemical mechanism. (continued)

Sulfur Chemistry			
	Reaction	k_{298}	$-E/R(K)$
72.[b]	$S(IV)+O_3 \rightarrow S(VI)+O_2$	2.4×10^4 3.7×10^5 1.5×10^9	 -5530 -5280
73.[b]	$S(IV)+H_2O_2 \rightarrow S(VI)+H_2O$	1.3×10^6	-4430
74.[b]	$S(IV)+\frac{1}{2}O_2 \xrightarrow{Mn^{2+},Fe^{3+}} S(VI)$	(Complex expression from Martin et al., 1991)	
75.	$SO_3^{2-}+OH \xrightarrow{O_2} SO_5^- + OH^-$	4.6×10^9	-1500
76.	$HSO_3^- + OH \xrightarrow{O_2} SO_5^- + H_2O$	4.2×10^9	-1500
77.	$SO_5^- + HSO_3^- \xrightarrow{O_2,H_2O} HSO_5^- + SO_5^-$ $SO_5^- + SO_3^{2-} \xrightarrow{O_2} HSO_5^- + SO_5^- + OH^-$	3.0×10^5 2.5×10^4	-3100 -2000
78.	$SO_5^- + O_2^- \xrightarrow{H_2O} HSO_5^- + OH^- + O_2$	1.0×10^8	-1500
79.	$SO_5^- + HCOOH \xrightarrow{O_2} HSO_5^- + CO_2 + HO_2$	200	-5300
80.	$SO_5^- + HCOO^- \xrightarrow{O_2} HSO_5^- + CO_2 + O_2^-$	1.4×10^4	-4000
81.	$SO_5^- + SO_5^- \rightarrow 2\ SO_4^- + O_2$	2.0×10^8	-1500
82.	$HSO_5^- + HSO_3^- + H^+ \rightarrow 2\ SO_4^{2-} + 3H^+$	7.5×10^7	-4760
83.	$HSO_5^- + OH \rightarrow SO_5^- + H_2O$	1.7×10^7	-1900
84.	$HSO_5^- + SO_4^- \rightarrow SO_5^- + SO_4^{2-} + H^+$	$<1.0\times10^5$	0
85.	$HSO_5^- + NO_2^- \rightarrow HSO_4^- + NO_3^-$	0.31	-6650
86.	$HSO_5^- + Cl^- \rightarrow SO_4^{2-} + Product$	1.8×10^{-3}	-7050
87.	$SO_4^- + HSO_3^- \xrightarrow{O_2} SO_4^{2-} + H^+ + SO_5^-$	1.3×10^9	-1500
88.	$SO_4^- + SO_3^{2-} \xrightarrow{O_2} SO_4^{2-} + SO_5^-$	5.3×10^8	-1500
89.	$SO_4^- + HO_2 \rightarrow SO_4^{2-} + H^+ + O_2$	5.0×10^9	-1500
90.	$SO_4^- + O_2^- \rightarrow SO_4^{2-} + O_2$	5.0×10^9	-1500

Table 5-4
Kinetic reactions included in the CMU aqueous-phase chemical mechanism. (continued)

Sulfur Chemistry (continued)			
	Reaction	k_{298}	$-E/R(K)$
91.	$SO_4^- + OH^- \rightarrow SO_4^{2-} + OH$	8.0×10^7	-1500
92.	$SO_4^- + H_2O_2 \rightarrow SO_4^{2-} + H^+ + HO_2$	1.2×10^7	-2000
93.	$SO_4^- + NO_2^- \rightarrow SO_4^{2-} + NO_2$	8.8×10^8	-1500
94.	$SO_4^- + HCO_3^- \rightarrow SO_4^{2-} + H^+ + CO_3^-$	9.1×10^6	-2100
95.	$SO_4^- + HCOO^- \xrightarrow{O_2} SO_4^{2-} + CO_2 + HO_2$	1.7×10^8	-1500
96.	$SO_4^- + Cl^- \rightarrow SO_4^{2-} + Cl$	2.0×10^8	-1500
97.	$SO_4^- + HCOOH \xrightarrow{O_2} SO_4^{2-} + H^+ + CO_2 + HO_2$	1.4×10^6	-2700
98.[b]	$S(IV) + CH_3C(O)O_2NO_2 \rightarrow S(VI)$	6.7×10^{-3}	0
99.[f]	$HSO_3^- + CH_3OOH \xrightarrow{H^+} SO_4^{2-} + 2H^+ + Product$	1.9×10^7	-3800
100.[b,f]	$HSO_3^- + CH_3C(O)OOH \rightarrow SO_4^{2-} + H^+ + Product$	5.0×10^7 6.0×10^2	-4000
101.	$S(IV) + HO_2 \rightarrow S(VI) + OH$ $S(IV) + O_2^- \xrightarrow{H_2O} S(VI) + OH + OH^-$	1.0×10^6 1.0×10^5	0 0
102.[f]	$SO_4^- + CH_3OH \xrightarrow{O_2} SO_4^{2-} + HCHO + H^+ + HO_2$	2.5×10^7	-1800
103.	$2HSO_3^- + NO_3 \xrightarrow{O_2} NO_3^- + H^+ + SO_4^{2-} + SO_4^-$	1.0×10^8	0
104.	$2\ NO_2 + HSO_3^- \xrightarrow{H_2O} SO_4^{2-} + 3H^+ + 2\ NO_2^-$	2.0×10^6	0
105a.[c]	$S(IV) + N(III) \rightarrow S(VI) + Product$	1.4×10^2	0
105b.[d]	$2\ HSO_3^- + NO_2^- \rightarrow OH^- + Product$	4.8×10^3	-6100
106.	$HCHO + HSO_3^- \rightarrow HOCH_2SO_3^-$ $HCHO + SO_3^{2-} \xrightarrow{H_2O} HOCH_2SO_3^- + OH^-$	2.9×10^2 2.5×10^7	-4900 -1800
107.	$HOCH_2SO_3^- + OH^- \rightarrow SO_3^{2-} + HCHO + H_2O$	3.6×10^3	-4500

Table 5-4
Kinetic reactions included in the CMU aqueous-phase chemical mechanism. (continued)

Sulfur Chemistry (continued)			
	Reaction	k_{298}	$-E/R(K)$
108.	$HOCH_2SO_3^- + OH \xrightarrow{O_2} SO_5^- + HCHO + H_2O$	1.4×10^9	-1500
109.	$HSO_3^- + Cl_2^- \xrightarrow{O_2} SO_5^- + 2\,Cl^- + H^+$	3.4×10^8	-1500
	$SO_3^{2-} + Cl_2^- \xrightarrow{O_2} SO_5^- + 2\,Cl^-$	3.4×10^8	-1500

(a) In appropriate units of M and s^{-1}.

(b) Reaction with "nonelementary" rate expression; see Seinfeld and Pandis (1998) for expressions.

(c) For pH <= 3.

(d) For pH > 3.

(e) Solar radiation dependent.

(f) Reactions included in the CMU code, but not activated in the CMU mechanism.

The CMU mechanism is implemented with options that allow the user to reduce the number of aqueous-phase chemical reactions used in a particular simulation. The user can select to include or ignore (1) the chlorine chemistry, (2) the radical chemistry, and (3) the iron and manganese catalyzed oxidation of dissolved SO_2. These options are set within the code; they are provided because these portions of the chemistry may have only small effects on the results and sometimes present very stiff numerical conditions that use significant amounts of computer time. In general, we recommend that the radical chemistry be neglected for computational efficiency. The concentrations of radical species (i.e., OH, HO_2, O_2^-, NO_3, $ClOH^-$, SO_4^-, and CO_3^-) become zero in the aqueous phase when the radical chemistry is turned off. The CMU mechanism consists then of 14 gas-aqueous equilibrium reactions, 16 aqueous-equilibrium reactions, and 32 aqueous-phase kinetic reactions among 18 gas-phase species and 19 aqueous-phase species.

The CMU mechanism is incorporated in CMAQ-MADRID as an option for the cloud chemical mechanism. Both the CMU and the RADM chemical mechanisms are coupled with the MADRID 1 aerosol module; the CMU mechanism is also coupled with the MADRID 2 aerosol module.

5.2 Aerosol Dynamics in Clouds

It is necessary to simulate aerosol dynamics in clouds using a sectional representation of the particle size distribution to allow the use of MADRID with cloud processes. Consequently, a

formulation for sectional aerosol dynamics in clouds is used that is compatible with both the RADM and CMU aqueous-phase chemical mechanisms. Aerosol dynamics is decomposed into two major components: (1) activation of particles into droplets during cloud formation and scavenging of particles by cloud droplets and (2) formation of particles after cloud evaporation. We describe the sectional formulation of these two components below.

5.2.1 Aerosol Activation

The parameterization of aerosol activation in CMAQ-MADRID uses a sectional representation of the particle size distribution of MADRID. Below we describe the theoretical basis of this parameterization of aerosol activation by cloud droplets and discuss the major differences between the original CMAQ formulation of aerosol activation and that of CMAQ-MADRID.

Aerosol activation is a cloud process that contributes to the concentrations of chemical species in cloud droplets. When an air parcel enters a cloud, a fraction of the aerosol particles (typically the larger ones) are activated to form cloud droplets, splitting the aerosol into an interstitial aerosol (i.e., unactivated) fraction and an "aerosol in cloud-droplet" (i.e., activated) fraction. These two fractions evolve further due to other cloud processes such as Brownian diffusion scavenging of interstitial particles, growth of activated particles via aqueous reactions, coalescence and precipitation scavenging of cloud droplets. The activated number fraction, F_{num}, is defined as the activated fraction of the total aerosol number concentration. The activated mass fraction, F_{mass}, is defined as the activated fraction of the total aerosol mass concentration. F_{mass} is larger than F_{num} because, according to Kohler theory, larger particles are activated at lower supersaturations, so that for a dispersed distribution of particles the activated mass fraction activated is always higher than the activated number fraction. The activation fraction is influenced by many factors including the types of clouds, cloud supersaturation, the characteristics of aerosols (e.g., number concentration, size distribution, chemical composition and solubility), and updraft velocity.

There are a number of observations for aerosol activation by cloud droplets. Gillani et al. (1995) conducted high-resolution aircraft measurements of accumulation-mode particles (0.17 to 2.07 μm in diameter) and cloud droplets (2 to 35 μm in diameter) in and around continental stratiform clouds to study the partitioning of cloud particles between activated droplets and unactivated interstitial aerosols. They found that F_{num} varied over its full possible range (0 to 1), with F_{num} exceeding 0.9 for 36% of the data and being less than 0.6 for 28% of the data. Leaitch (1996) conducted airborne observations for two types of continental clouds. He found that the accumulation-mode particles were not 100% activated, with F_{num} being ~70% for the cumulus clouds and 15-50% for the stratus clouds. Liu et al. (1996) also estimated that 10-40% of the accumulation-mode mass may have remained unactivated. This corresponds to a value of F_{mass} of 0.6-0.9. The cut-off particle diameter over which the particles can be activated has also been estimated through observations. The estimated minimum diameter of particles activated in marine stratus ranges from 0.14 to 0.31 μm (Leaitch et al., 1996). For continental clouds, the minimum diameter of particles activated can be from 0.25 to 0.37 μm (Gillani et al., 1995;

Leaitch, 1996). Particles with diameter less than 0.08 μm are too small to be activated (Hoppel et al., 1996).

There are several parameterizations or modules available to simulate aerosol activation by cloud droplets. These include the empirical parameterizations of Squires (1958) and Twomey (1959) and the detailed microphysical modules of Ghan et al. (1993; 1995), Abdul-Razzak et al. (1998) and Abdul-Razzak and Ghan (1999). The empirical parameterizations do not take into account fundamental aerosol characteristics such as aerosol number, size and composition, and involve many assumptions. The detailed microphysical modules use approximate analytical expressions and account for the effect of aerosol properties. However, those detailed microphysical modules were developed for a modal representation of the aerosol size distribution with a small number of modes of moderate width and they are not directly applicable to a sectional representation of the aerosol size distribution.

In the original aerosol activation parameterization of CMAQ, the accumulation mode and coarse mode aerosols are assumed to be completely activated into cloud droplets, and the Aitken mode aerosols are treated as interstitial aerosols which are assumed to be slowly absorbed into cloud/rain water (according to an exponential function, see below, Equation 5-2). Note that the initial mass of Aitken mode aerosols is assumed to be 0.1% of total initial $PM_{2.5}$ mass in CMAQ. With this parameterization, 99.9% of $PM_{2.5}$ ($PM_{2.5}$=Aitken mode + accumulation mode) mass is completely activated into cloud droplets, which is not generally consistent with available observations.

The empirical parameterization of CMAQ-MADRID is based on available observations. For a relatively fine resolution of the particle size representation (i.e., 6 or more size sections between 0.02 and 10 μm), particles with aerodynamic diameter greater than 0.35 μm are assumed to be 100% activated (this diameter corresponds to a Stokes diameter of 0.3 μm for a density of 1.35 g cm^{-3}; the Stokes diameter is used in MADRID). This assumption is sound because particles larger than this size are estimated to require a supersaturation less than 0.03% for activation, a prevailing condition for most clouds (Gillani et al., 1995). Particles with aerodynamic diameter greater than 0.1 μm (i.e., a Stokes diameter of 0.086 μm for a density of 1.35 g cm^{-3}) but smaller than 0.35 μm are assumed to be partially activated. There are large uncertainties in the fraction of activation for particles within this size range. Both observations and theoretical calculations have shown that the fraction of activation for particles in this size range can vary from 0 to 1. We assume that 50% of the particle mass in this size range is activated completely into cloud droplets, and that the remaining 50% of particle mass is slowly activated according to the following equation of in-cloud scavenging:

$$\frac{dm_{p,air}(t)}{d_t} = -\beta \cdot m_{p,air}(t) \tag{5-1}$$

with solution

$$m_{p,air}(t+\tau_{cld}) = m_{p,air}(0)(1-f_{mass})\exp(-\beta\tau_{cld}) \tag{5-2}$$

where $m_{p,air}(0)$ and $m_{p,air}\ (t + \tau_{cld})$ are the initial concentration of interstitial particle and its concentration at time $t + \tau_{cld}$, τ_{cld} is the cloud lifetime, f_{mass} is the fraction of activation of the particle mass concentration, $f_{mass} = 0.5$ for particles with an aerodynamic diameter between 0.1 and 0.35 μm. β is the mass scavenging coefficient for interstitial particles. It can be calculated based on the equation of Pruppacher and Keltt (1978) as follows:

$$\beta = 2\pi\, m_{1c}\, \hat{D_p}\, (1 + 0.5\, Pe^{1/3}) \tag{5-3}$$

$$where\ \ m_{1c} = n_c \cdot d_{dg} \exp[\tfrac{1}{2} \ln^2 (\sigma_{dg})] \tag{5-4}$$

n_c, d_{dg}, σ_{dg} are the cloud droplet number concentration, geometric mean diameter and geometric standard deviation of the cloud droplet size distribution, respectively. *Pe* is a Peclet number,

$$Pe = \frac{V_{dc}\, d_{dg}}{\hat{D}_p} \tag{5-5}$$

where V_{dc} is the settling velocity of the cloud droplets, $\hat{D_p}$ is the polydisperse diffusivity, it is given by:

$$\hat{D_p} = \frac{k_b\, T}{3\pi\, \upsilon\, \rho_{air} \cdot d_{dg}} \left\{\exp(-2.5 \ln^2 \sigma_{dg}) + 1.246\, Kn_g \exp(-4 \ln^2 \sigma_g)\right\} \tag{5-6}$$

where k_b is the Boltzman constant, T is the temperature, υ is the dynamic viscosity of air, ρ_{air} is the density of air, Kn_g is the Knudsen number for cloud droplets,

$$Kn_g = 2\lambda / d_{dg} \tag{5-7}$$

where λ is the mean tree path of air.

The rate of change of the concentration of the activated particle in cloud droplets is as follows.

$$\frac{dm_{p,cld}(t)}{dt} = m_{p,air}(0) \cdot f_{mass} + \beta \cdot m_{p,air}(t) + P \tag{5-8}$$

where $m_{p,cld}$ is the concentration of the activated particle in cloud droplets, the first term in the right-hand side of the Equation 5-8 represents the 50% of the particle mass that is completely activated into cloud droplets, the second term represents the remaining 50% of the particle mass that is slowly activated according to the exponential function shown in Equation 5-2, and the third term represents the production of new particle mass by aqueous-phase chemistry. The total aqueous-phase production of particle mass can be obtained by integrating the rate of change due to gas-particle equilibrium reactions and aqueous-phase dissociation and kinetic reactions. The

total mass of new particles is distributed over the particle size distribution according to the initial mass fractions of particles in each size section.

Particles with diameter less than 0.1 μm are assumed to remain as interstitial particles with 0% activated. For a coarse resolution of the particle size distribution (i.e., 2 to 5 size sections between 0.02 and 10 μm), particles with aerodynamic diameter greater than 2.5 μm (i.e., a Stokes diameter of 2.15 μm for a density of 1.35 g cm^{-3}) are assumed to be 100% activated, 80% of particles with aerodynamic diameter less than 2.5 μm (i.e., $PM_{2.5}$) are assumed to be completely activated, and the remaining 20% of $PM_{2.5}$ mass is assumed to be slowly activated or scavenged by cloud droplets according to the exponential function shown in Equation 5-2, with $f_{mass} = 0.8$.

Table 5-5 summarizes the parameterization that is used to simulate aerosol activation by cloud droplets in the cloud processes coupled with MADRID.

Table 5-5
The new parameterization of aerosol activation used in the sectional version of CMAQ.

Particle Size Range, μm	Fraction of Activation, F_{mass}
For 6 or more sections between 0.02 and 10 μm:	
d_p[a] > 0.35	1.0
0.1 < $d_p \leq$ 0.35	0.5[b]
$d_p \leq$ 0.1	0.0
For 2-5 sections between 0.02 and 10 μm:	
d_p > 2.5	1.0
$d_p \leq$ 2.5	0.8[c]

(a) d_p denotes the low-bound aerodynamic diameter of each size section.

(b)The remaining 50% particle mass are activated according to $exp(-\beta \tau)$, where β is the mass scavenging coefficient for particles with 0.1 < $d_p \leq$ 0.35, τ is the cloud lifetime.

(c) The remaining 20% particle mass are activated according to $exp(-\beta \tau)$, where β is the mass scavenging coefficient for particles with $d_p \leq$ 2.5, τ is the cloud lifetime.

5.2.2 Formation of Aerosols After Cloud Evaporation

New particles are formed when clouds evaporate. The particle concentrations after cloud evaporation is calculated as follows. The change in mass concentration of all particulate components (i.e., sulfate, nitrate, ammonium, EC, organic material (OM) and other species) during the cloud lifetime (i.e., between cloud formation and cloud evaporation) is calculated

first. This change in mass concentration is then added to the initial (i.e., before activation in cloud droplets) particle size distribution using a uniform relative change across the particle size distribution. For example, if the total change in sulfate concentration is a 10% increase, the sulfate concentrations in each particle size section are increased by 10%.

If a two-section particle size representation is used, there is no change in the particle size distribution. If a multi-section particle size representation is used, however, it is necessary to account for particle growth that occurs due to the increase in mass in each size section. The moving-center algorithm is used to calculate the new particle size distribution that results from this particulate mass increase.

6
HETEROGENEOUS CHEMISTRY

Heterogeneous reactions on condensed phases (e.g., particles or cloud/fog droplets) may have significant effect on O_3 and PM formation (Jacob, 2000). We present here the treatment of heterogeneous reactions in CMAQ-MADRID. First, we discuss the selection of the reaction probabilities of these species and the formulation of the heterogeneous reaction rate constants. To that end, the sensitivity of the rate constants to several variables such as temperature and cloud liquid water content is analyzed.

6.1 Reaction Probabilities and Heterogeneous Reaction Rate Constants

Jacob (2000) conducted a review of heterogeneous chemistry and recommended that the heterogeneous reactions of HO_2, NO_2, NO_3, and N_2O_5 on the surface of aqueous particles and in cloud droplets be parameterized by a simple reaction probability in standard O_3 models. In this parameterization, the uptake of a gas-phase species by condensed phases is considered as an irreversible loss process with a first-order heterogeneous reaction rate constant. Based on Jacob (2000), we consider the following heterogeneous reactions on the surface of aqueous particles or in cloud/fog droplets:

$$HO_2 \xrightarrow{PM} 0.5H_2O_2$$
$$NO_2 \xrightarrow{PM} 0.5HONO + 0.5HNO_3$$
$$NO_3 \xrightarrow{PM} HNO_3$$
$$N_2O_5 \xrightarrow{PM} 2HNO_3$$
$$HO_2 \xrightarrow{Cloud\ /\ Fog} 0.5H_2O_2$$
$$NO_3 \xrightarrow{Cloud\ /\ Fog} HNO_3$$
$$N_2O_5 \xrightarrow{Cloud\ /\ Fog} 2HNO_3$$

Note that we did not include the heterogeneous reaction of NO_2 on cloud/fog droplets. The rate of that reaction would be relatively fast (NO_2 half-life of 26 min for a typical cloud with liquid water content of 0.2 g m^{-3} and droplet radius of 10 μm, using a reaction probability of 1.0 x 10^{-4}) and, therefore, unrealistic. Moreover, recent experimental data suggest that bulk aqueous-phase chemistry is consistent with the rate of reaction of NO_2 in presence of condensed water (Cheung et al., 2000). Following discussions with Jacob (2001), we elected not to include the heterogeneous reaction of NO_2 on droplets; it is however, included in the bulk aqueous-phase

chemistry of the Carnegie-Mellon University (CMU) mechanism. The first-order rate constant, k, for the heterogeneous loss of a gas to the condensed phase is calculated following Jacob (2000):

$$k = \left(\frac{a}{D_g} + \frac{4}{\nu\gamma}\right)^{-1} A \qquad (6\text{-}1)$$

where a is the radius of particles or cloud/fog droplets in m, D_g is the gas-phase molecular diffusion coefficient of a gaseous chemical species in air in $m^2 s^{-1}$, ν is the mean molecular speed of that species in air in $m\ s^{-1}$, γ is the reaction probability, which represents the likelihood that a gas molecule impacting the surface of the condensed phase will undergo reaction, and A is the surface area of the condensed phase in m^2. For atmospheric particles, A is obtained by integrating over the particle size distribution. The first term on the right-hand side of Equation 6-1 represents the uptake by diffusion from the bulk gas phase to the surface of the condensed phase and the second term represents the uptake by free molecular collisions of gas molecules with the surface. If $k \rightarrow (D_g A/a)$, the uptake of a gas molecule by the condensed phase is diffusion-limited and shows little dependence on the value of γ. On the other hand, if $k \rightarrow (\nu\gamma A/4)$, the uptake of a gas molecule tends to be limited by free molecular collision and depends strongly on the magnitude of γ.

As shown in Equation 6-1, there are several important yet uncertain variables in the calculation of k, such as γ and A. The quantity γ has been measured in the laboratory for a number of gases on various condensed phases and its values may differ by several orders of magnitudes for a given species on different types of surfaces. The surface area of particles depends on the particle number concentrations and size distribution, which exhibit high temporal and spatial variabilities. The surface area of cloud/fog droplets depends on the radii of cloud/fog droplets and the cloud/fog liquid water content, which are quite different for different types of clouds/fogs. In addition, k is a function of ambient temperature and pressure because ν is temperature-dependent and D_g is temperature- and pressure-dependent.

6.2 Sensitivity Studies

We conducted a number of sensitivity calculations to study the heterogeneous reaction rate constants over a plausible range of atmospheric conditions. In these calculations, the sensitivity of k to several variables including γ, D_g, temperature, cloud droplet radius, cloud liquid water content, and particle radius and size distributions was investigated. The values of the variables used in the base and sensitivity calculations are provided in Tables 6-1 and 6-2. Table 6-1 lists the base, upper limit, and lower limit values of the reaction probabilities (γ) of HO_2, NO_2, NO_3, and N_2O_5 used in the calculations. Those values were taken from Jacob (2000). Table 6-2 lists the values of D_g, temperature, cloud/fog droplet radii, cloud/fog liquid water contents, and particle size distributions used in the calculations. The typical tropospheric values of D_g for various species are in the range of 0.1 to 0.2 $cm^2\ s^{-1}$. We assumed a constant value of D_g for all the species; values of 0.1 or 0.2 $cm^2\ s^{-1}$ were selected. The temperatures used in our calculations

were 273 K, 283 K, 293 K, 298 K, and 303 K. Cloud droplet radii vary from a few μm to 25 μm, with average radii usually in the 5 to 10 μm range and the liquid water content varies from 0.05 to 3 g m^{-3} for typical clouds and 0.02 to 0.5 g m^{-3} for fogs (Seinfeld and Pandis, 1998). A cloud droplet radius of 5, 10, and 20 μm and a liquid water content of 0.02, 0.2, and 3 g m^{-3} were used in the calculations of first-order rate constants for heterogeneous reaction in cloud/fog droplets. The surface areas of cloud/fog droplets with these values of radii and liquid water contents range from 30 to 1800 cm^2 m^{-3}. In calculating first-order rate constants for the heterogeneous reactions on the surface of atmospheric particles, we used the log-normal particle size distributions typical of clear, hazy, and urban conditions as described in Seigneur et al. (1986). The total particle mass concentrations under these conditions ranged from 11 to 126 μg m^{-3}. The atmospheric particle concentrations can reach up to several hundreds to several thousands μg m^{-3} under dust storm conditions due to high emissions of dust particles from deserts and arid areas and their long-range-transport to downwind regions or high relative humidity conditions due to a large amount of water uptake (e.g., Zhang and Carmichael, 1999). We also calculated the first-order rate constants under such high particle loading conditions (referred to as high aerosol conditions thereafter), with a total particle mass concentration of 1010 μg m^{-3}. Figure 6-1 shows the surface area and volume size distributions of particles under clear, hazy, urban, and high aerosol conditions. The accumulation mode particles have the maximum surface area under all conditions and the maximum volume concentration under the urban and high aerosol conditions. The sharp decrease in the surface and volume concentrations under hazy conditions is characteristic of an aged air mass where ultrafine particles have coagulated with larger particles. The total particle surface areas under the four conditions are 0.5, 2.2, 11.3, and 144 cm^2 m^{-3}, respectively.

Table 6-1
Reaction probabilities (γ) used in the base and sensitivity calculations of the heterogeneous reaction rate constants (Source: Jacob, 2000).

Species	Base value	Lower limit value	Upper limit value
HO_2	0.2	0.1	1.0
NO_2	1.0×10^{-4}	1.0×10^{-6}	1.0×10^{-3}
NO_3	1.0×10^{-3}	2.0×10^{-4}	1.0×10^{-2}
N_2O_5	0.1	0.01	1.0

Table 6-2
Variables used in the base and sensitivity calculations of the heterogeneous reaction rate constants.

Variable	Base value/case	Sensitivity values/cases
Gas-phase diffusivity, cm^2 s^{-1}	0.1	0.2
Temperature, K	298.15	273, 283, 293, 303, 313
Droplet radius μm	10	5, 20
Liquid water content, g m^{-3}	0.2	0.02, 3.0
Particle size distribution	Urban conditions	Clear, hazy, and high aerosol conditions

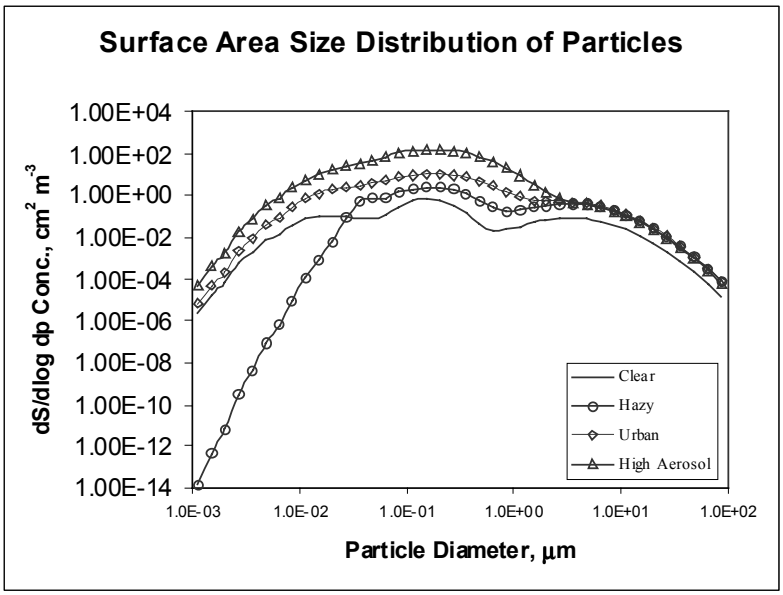

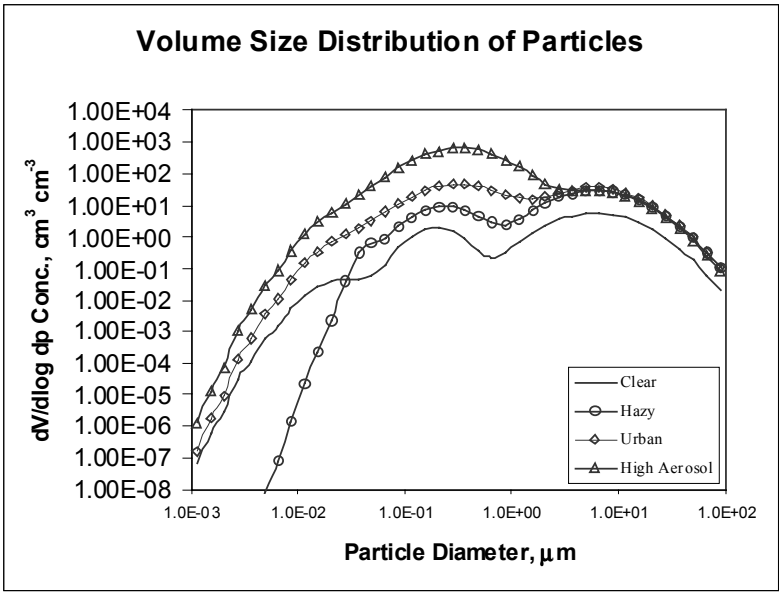

Figure 6-1
The surface area (top) and volume (bottom) size distributions of particles under clear, hazy, urban, and high aerosol conditions.

We discuss below the first-order rate constants of heterogeneous reactions on the surface of particles and in the cloud/fog droplets and their sensitivities to several variables.

6.2.1 Heterogeneous Rate Constants for Gas-Particle Reactions

Figure 6-2 shows the size-resolved first-order loss rate constant k of HO_2, NO_2, NO_3, and N_2O_5 as a function of particle size under the clear, hazy, urban, and high aerosol conditions. A value of D_g of 0.1 $cm^2\ s^{-1}$, a temperature of 298.15 K, and the base γ values of each species shown in Table 6-1 were used in the calculation. Given D_g, γ, and ν, the first-order loss rate constant k is a strong function of the particle diameter. The maximum value of k occurs for particles in the accumulation mode and the minimum value occurs for particles either in the lower diameter range (e.g., under hazy conditions for all species) or the higher diameter range (e.g., under all other conditions for HO_2). The maximum value of k results from the fact that k is proportional to the total surface area of particles, which peaks for accumulation-mode particles (see Figure 6-1). Under each set of atmospheric conditions, the values of k for each species differ by at least 6 orders of magnitudes among particles with different diameters, due to significantly different magnitudes of the surface areas for these particles. For particles with the same diameter, the values of k differ by several orders of magnitude for different species. For example, for particles with a diameter of 2.0 μm under urban conditions, the values of k are 4.4 x 10^{-5} s^{-1} for HO_2 and 6.0 x 10^{-8} s^{-1} for NO_2.

The magnitude of k is largely dependent on the relative magnitude of the gas-phase diffusion term and the free molecular collision term in Equation 6-1, which in turn depend on the values of the particle radius a, the gas-phase diffusion coefficient D_g, and the reaction probability γ used. For a value of D_g of 0.1 $cm^2\ s^{-1}$, a diameter of 2 μm, and a value of γ of 0.2, the uptake of HO_2 on the particle surface is diffusion-limited, with $k \rightarrow (D_g A/a)$. For the same values of D_g and particle diameter but a value of γ of 1.0 x 10^{-4}, the uptake of NO_2 on the particle surface is limited by the free molecular collision, with $k \rightarrow (\nu\gamma A/4)$.

This feature is illustrated in Figure 6-3, which shows the sensitivity of size-resolved k to the reaction probability γ for HO_2, NO_2, NO_3, and N_2O_5. The uptake of HO_2 is diffusion-limited over the entire range of γ values considered here, for particles with diameter greater than 2 μm. As a result, k shows little dependence on the values of γ used for this size range. For particles with diameters smaller than 2 μm, the uptake of HO_2 lies in the transition regime between gas-phase diffusion and free molecular collision, resulting in k increasing with an increased γ. The uptake of N_2O_5 is diffusion-limited with γ values of 0.1 and 1.0 for particles with diameter greater than 4 μm. However, for $\gamma = 0.01$, the uptake of N_2O_5 is diffusion-limited only for particles with diameter greater than ~30 μm. For NO_2 and NO_3, since the γ values used were either 0.01 or smaller, the uptake of NO_2 and NO_3 is either limited by free molecular collision (e.g., for particles with diameter less than 0.01 μm) or in the transition regime between gas-phase diffusion and free molecular collision. Higher values of γ always result in significantly higher values of k if the uptake of a species is not diffusion-limited.

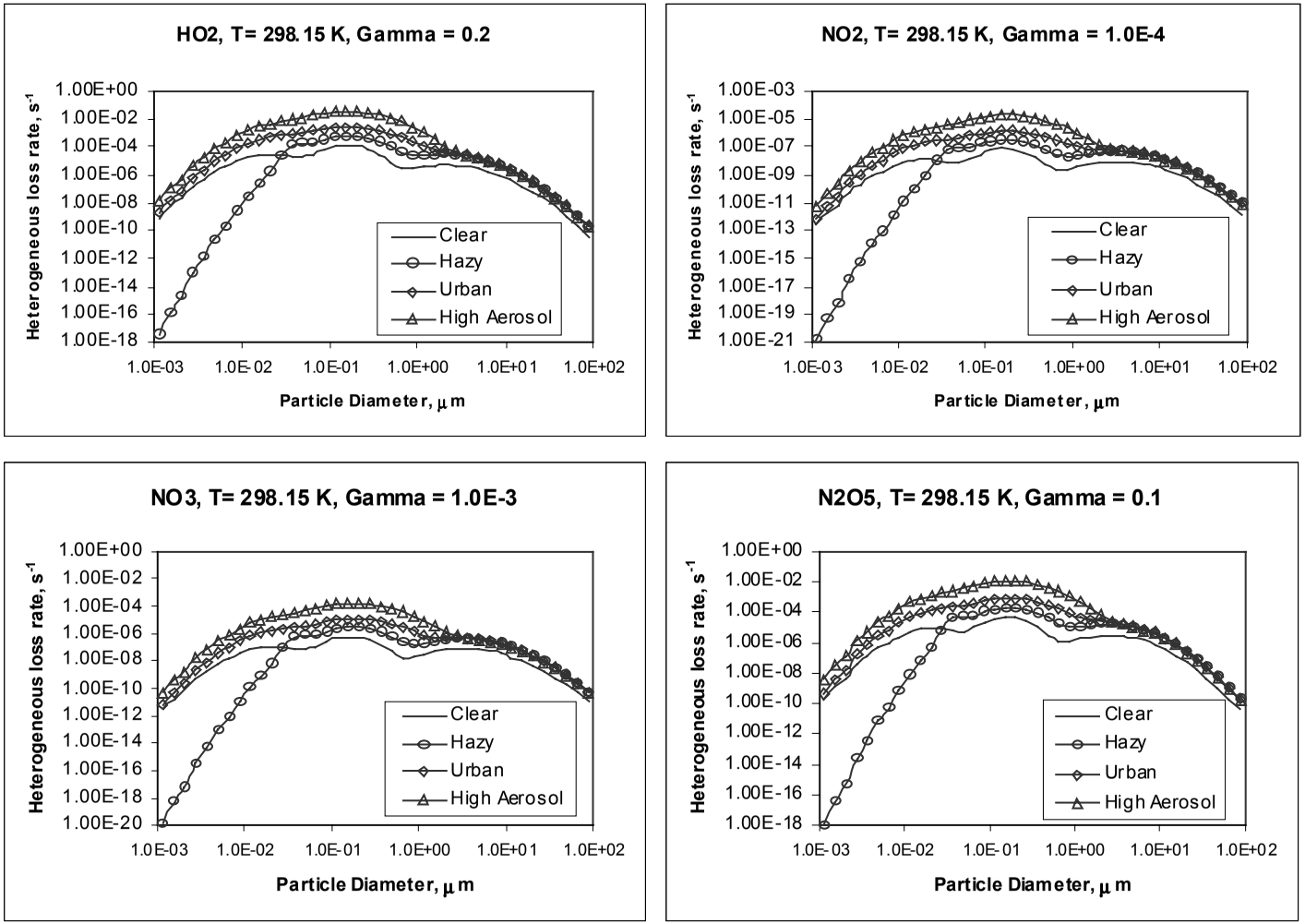

Figure 6-2
The size-resolved first-order loss rate constant k_{HO2}, k_{NO2}, k_{NO3}, and k_{N2O5} as a function of the particle size distribution under the clear, hazy, urban, and high aerosol conditions with their base γ values and a temperature of 298.15 K.

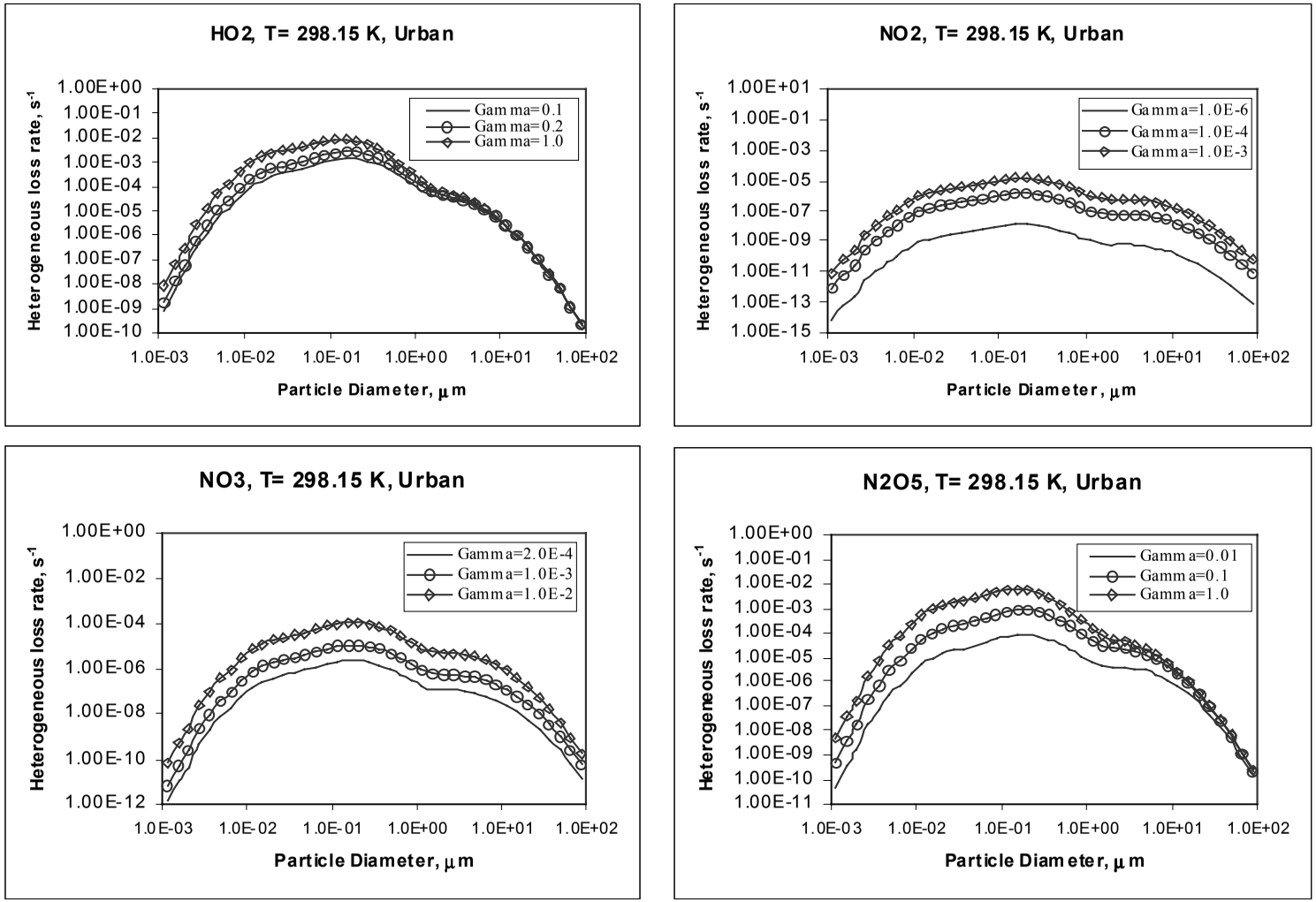

Figure 6-3
The sensitivity of size-resolved first-order loss rate constant k_{HO2}, k_{NO2}, k_{NO3}, and k_{N2O5} as a function of the particle size distribution to their reaction probability γ values.

Figures 6-4 and 6-5 show the sensitivity of k (integrated over the particle size distribution) to the particle size distribution (i.e., the particle surface area A), γ, D_g, and temperature, respectively. In evaluating the sensitivity of k to changes in γ, D_g, and temperature, a particle size distribution representative of urban conditions was used. As shown in Figure 6-4, k is very sensitive to changes in the total particle surface area A. The value of k for all species increases by a factor of about 300, when the particle surface area increases from 0.5 cm^2 m^{-3} under clear conditions to 144 cm^2 m^{-3} under high aerosol conditions.

The values of k for NO_2, NO_3, and N_2O_5 increase by factors of 1000, 50, and 65, respectively, when their γ values increase from the lower limit to the higher limit, whereas the value of k for HO_2 only increases by a factor of 6. The uptake of NO_2, NO_3, and N_2O_5 is largely limited by free molecular collision with their lower limit values of γ; changing γ from its lower limit to upper limit results in a large response in the value of k. On the other hand, the uptake of HO_2 on particles with diameter larger than 2 μm is limited by gas-phase diffusion and shows little dependence on γ, resulting in a small response in k.

Since the uptake of HO_2 and N_2O_5 is diffusion-limited for larger particle size range (diameter greater than 2 and 4 μm, respectively), using the base γ values under urban conditions, the values of k for HO_2 and N_2O_5 increase by 9% and 3%, respectively, when D_g increases from 0.1 to 0.2 cm^2s^{-1}. By contrast, the values of k for NO_2 and NO_3 remain unchanged when D_g doubles, because the uptake of NO_2 and NO_3 is not diffusion-limited.

As shown in Figure 6-5, k_{HO2}, k_{NO2}, k_{NO3}, and k_{N2O5} increase by 10%, 7%, 7%, and 8%, respectively, when the temperature increases from 273 to 313 K.

6.2.2 Heterogeneous Rate Constants for Gas-Droplet Reactions

The droplet size distribution is not simulated in CMAQ. In calculating the first-order heterogeneous loss rate in cloud/fog droplets, we assume that cloud or fog droplets are monodispersed, namely, all droplets have the same diameter. A droplet diameter of 20 μm was used in the base calculation. Figures 6-6 and 6-7 show the sensitivity of k in cloud/fog droplets to changes in the reaction probability γ, gas-phase diffusion coefficient D_g, droplet radius a, liquid water content LWC, and temperature.

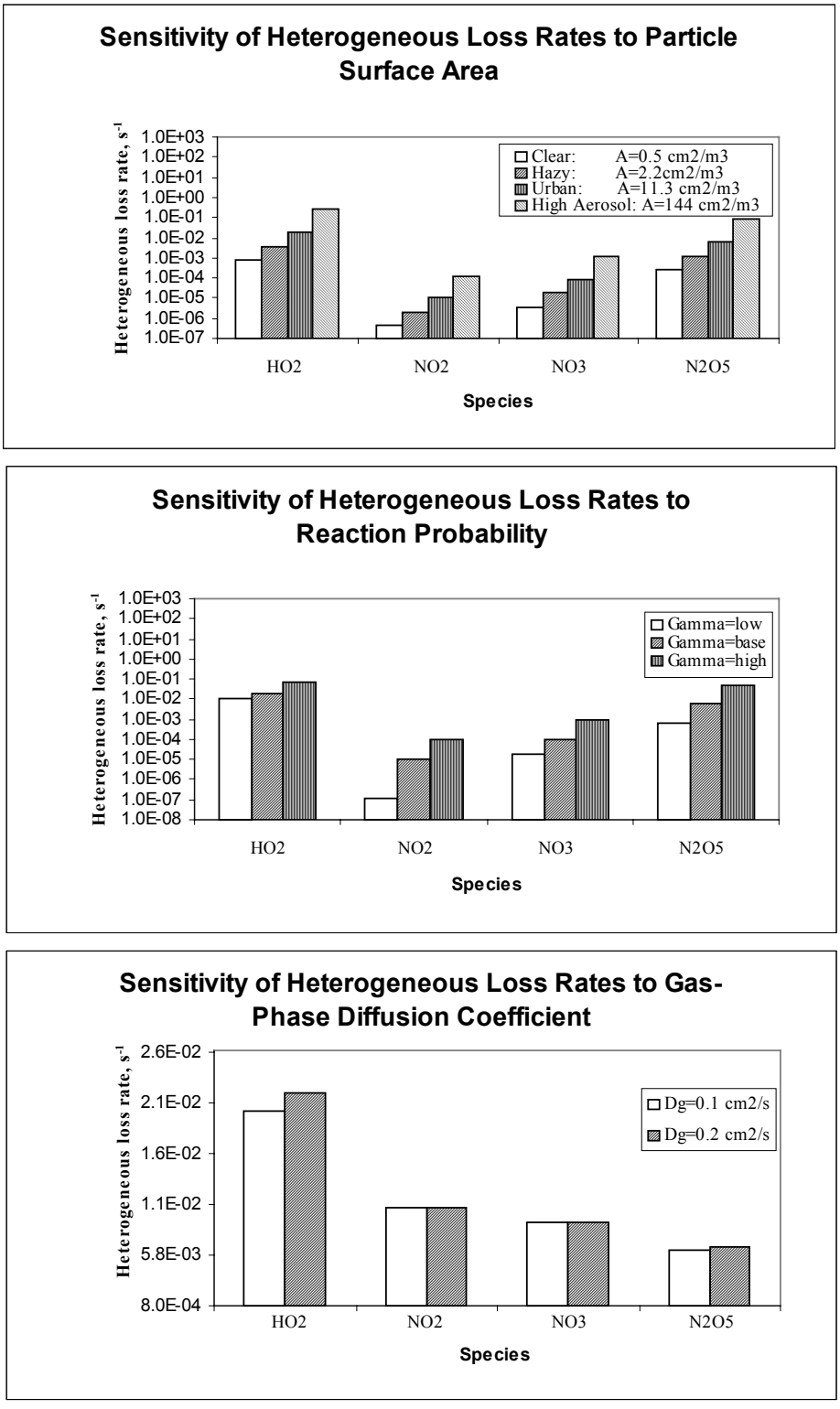

Figure 6-4
The sensitivity of k_{HO2}, k_{NO2}, k_{NO3}, and k_{N2O5} (integrated over the particle size distribution) to particle size distribution (i.e., the particle surface area *A*), γ, and D_g.

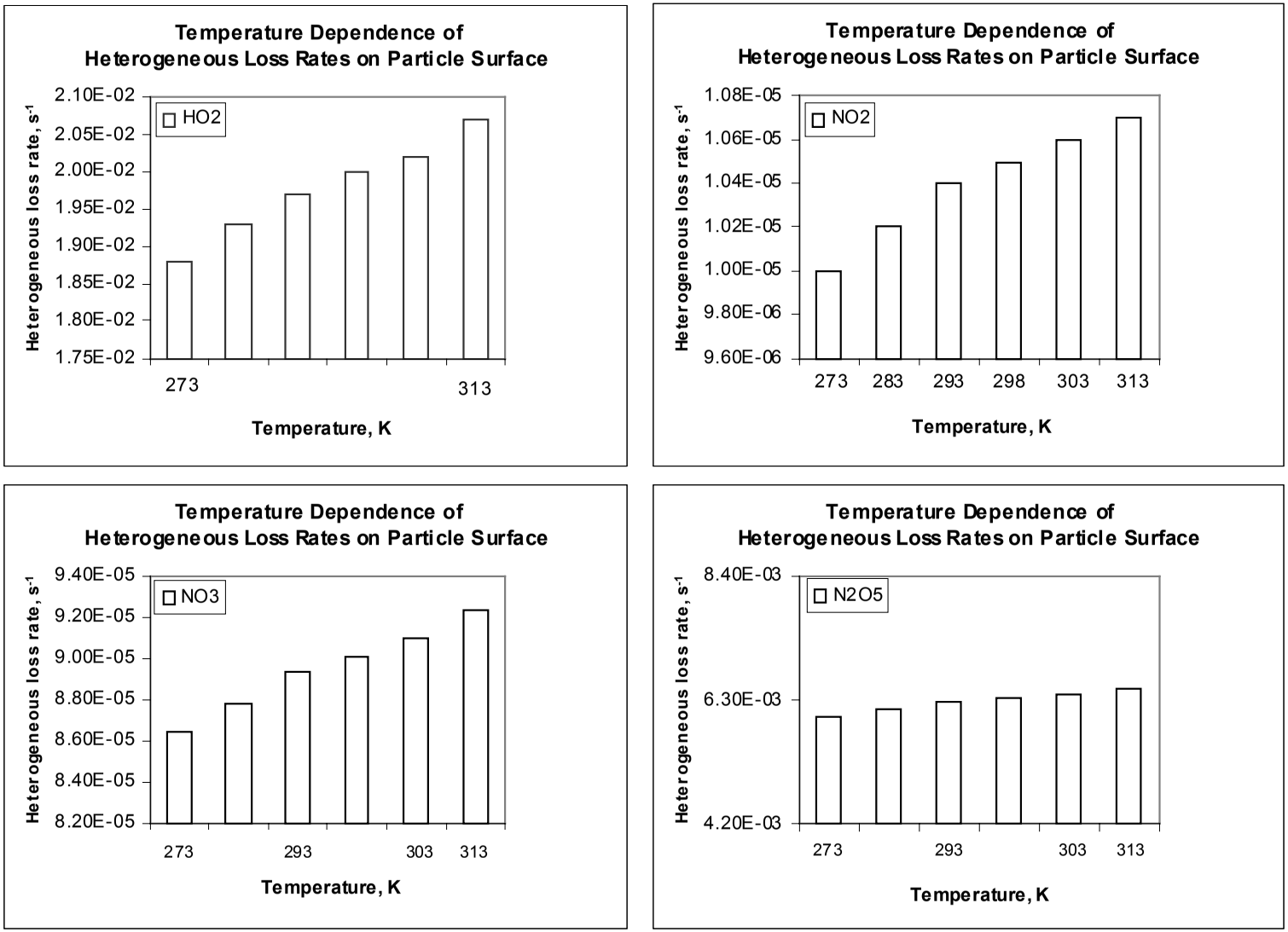

Figure 6-5
The sensitivity of k_{HO2}, k_{NO2}, k_{NO3}, and k_{N2O5} (integrated over the particle size distribution) to temperature.

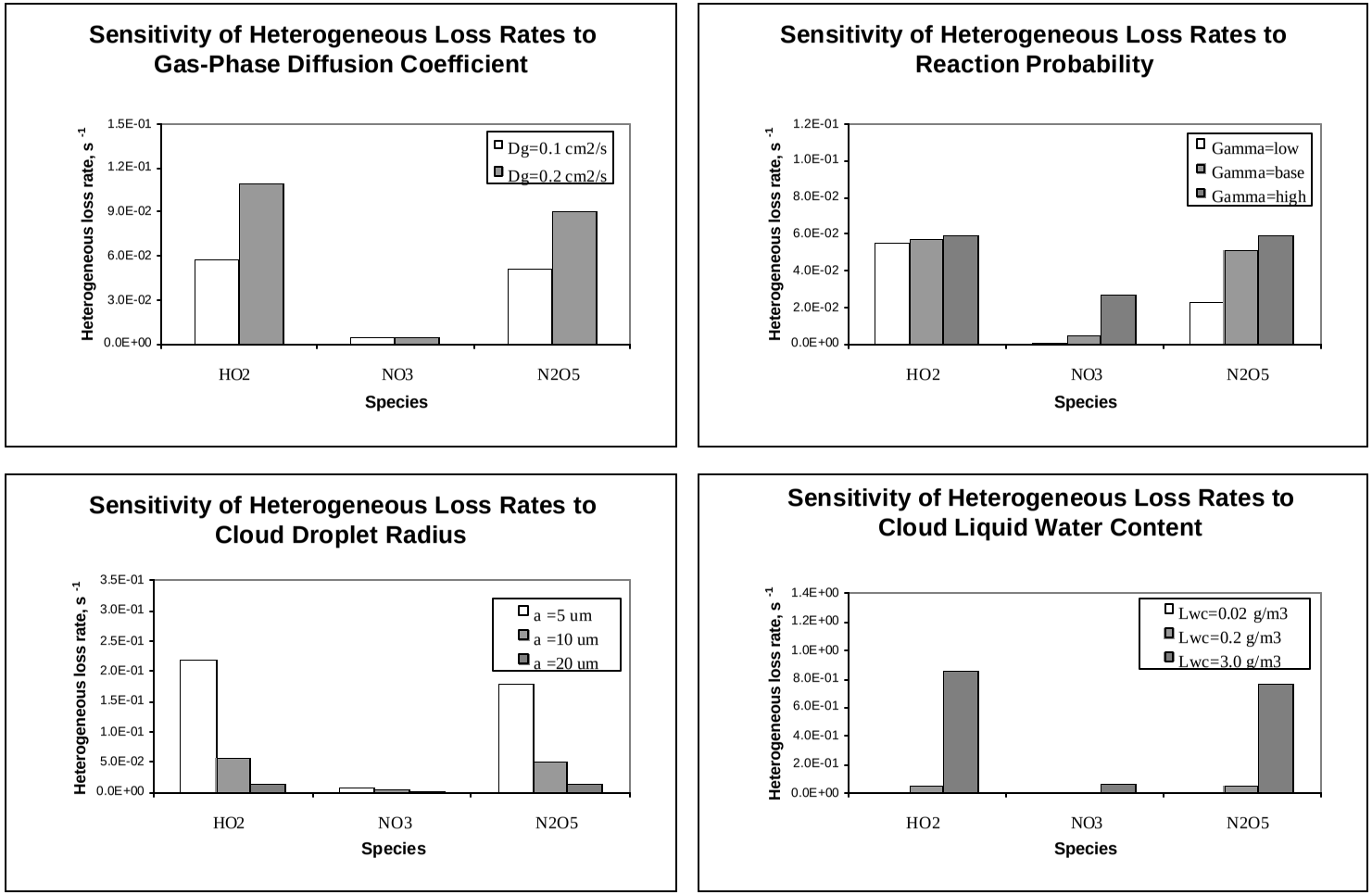

Figure 6-6
The sensitivity of *k* for HO_2, NO_3, and N_2O_5 in cloud/fog droplets to the gas-phase diffusion coefficient D_g, reaction probability g, droplet radius *a*, and liquid water content LWC.

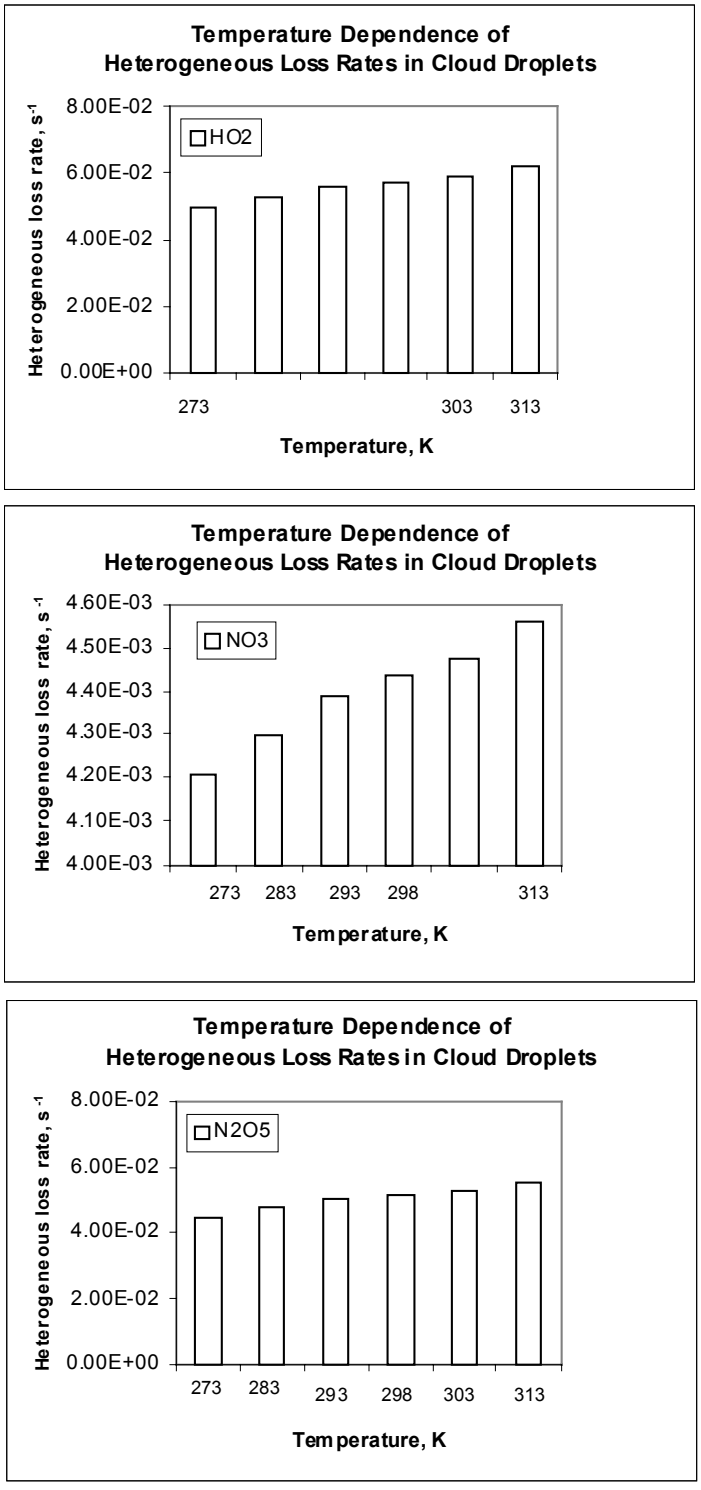

Figure 6-7
The sensitivity of *k* for HO_2, NO_3, and N_2O_5 in cloud/fog droplets to temperature. A cloud droplet radius of 10 μm, a D_g of 0.1 $cm^2 s^{-1}$, a liquid water content of 0.2 g m^{-3}, and the base γ values were used.

The values of k for HO_2 and N_2O_5 increase by 91% and 75%, respectively, but that for NO_3 only increases by 4% when D_g increases from 0.1 to 0.2 cm^2s^{-1}. The uptake of HO_2 and N_2O_5 by cloud/fog droplets with a diameter of 20 μm and γ value of 0.2 and 0.1, respectively, is diffusion-limited, whereas with its $\gamma = 10^{-3}$, the uptake of NO_3 by cloud/fog droplets is not diffusion-limited.

For the same reason, the uptake of HO_2 is almost insensitive to changes in γ, whereas the uptake of NO_3 is very sensitive to changes in γ. The values of k increase by 8% and a factor of 28 for HO_2 and NO_3, respectively, when γ changes from its lower limit to higher limit. The uptake of N_2O_5 is modestly sensitive to changes in γ, increasing by a factor of 2.6 when γ increases from 0.01 to 1.0, because the uptake of N_2O_5 changes from a transition regime to a diffusion-limited regime.

The values of k for HO_2, NO_3, and N_2O_5 are sensitive to changes in the droplet radius, decreasing by 93%, 78%, and 92%, respectively, when the droplet radius increases from 5 to 20 μm. The higher response in k for HO_2 and N_2O_5 is due to the fact that the uptake of HO_2 and N_2O_5 is diffusion-limited, whereas the uptake of NO_3 is limited by both gas-phase diffusion and free molecular collision.

The values of k for HO_2, NO_3, and N_2O_5 are very sensitive to changes in the liquid water content, increasing by a factor of 15 when the liquid water content increases from 0.02 to 3.0 g m^{-3}. As shown in Figure 6-7, temperature has a larger impact on k for cloud/fog droplets than for particles because the process is more diffusion-limited for droplets than for particles. The values of k for HO_2, NO_3, and N_2O_5 increase by 26%, 8%, and 24%, respectively, when the temperature increases from 273 to 313 K.

6.2.3 Summary

The heterogeneous reaction rate constant for the uptake of all species of interest is very sensitive to changes in the particle size distribution, droplet radius, and droplet liquid water content, and modestly sensitive to changes in temperature. The sensitivity of k to changes in γ and D_g depends on which regime (diffusion-limited or collision-limited) governs the uptake of the species by particles or droplets. For species with a dominant gas-phase diffusion-limited uptake such as HO_2, the heterogeneous reaction rate constant is insensitive to changes in γ and either modestly or highly sensitive to changes in D_g, depending on the radius of the condensed phase. For species that are not limited by gas-phase diffusion (e.g., NO_2 and NO_3), the heterogeneous reaction rate constant is very sensitive to changes in γ and insensitive to changes in D_g. The uptake of N_2O_5 can be either fully diffusion-limited (e.g., in cloud droplets with diameter greater than 20 μm and $\gamma = 0.1$), partially diffusion-limited (e.g., on particles under urban conditions with $\gamma = 0.1$) or in a transition regime (in cloud droplets with diameter greater than 20 μm and $\gamma = 0.01$ or on particles under urban conditions with $\gamma = 0.01$), depending on the radius of the particle/droplet and the values of the reaction probabilities used. For urban conditions, the uptake of N_2O_5 by particles is highly sensitive to changes in γ and slightly sensitive to changes in

D_g. For the cloudy conditions considered here, the uptake of N_2O_5 is sensitive to changes in both γ and D_g.

In MADRID, the values of the reaction probabilities are chosen to be the base values listed in Table 6-1; i.e., 0.2, 1.0×10^{-4}, 1.0×10^{-3} and 0.1 for HO_2, NO_2, NO_3 and N_2O_5, respectively. The heterogeneous reactions of HO_2, NO_2, NO_3 and N_2O_5 on the surface of particles are added to the three gas-phase mechanisms (i.e., CBM-IV, RADM2 and CACM) in CMAQ/MADRID. Since the CMU aqueous-phase mechanism already includes the scavenging of HO_2, NO_2, and NO_3 by cloud droplets and their subsequent aqueous-phase equilibria and reactions, the heterogeneous reaction of N_2O_5 in cloud droplets is the only one added to the three gas-phase mechanisms.

7
ATMOSPHERIC DEPOSITION

The treatment of atmospheric deposition differs in several respects between the original CMAQ and CMAQ-MADRID. First, we describe the treatment of dry deposition. Next, we describe the treatment of wet deposition.

7.1 Dry Deposition

7.1.1 Gases

Dry deposition is treated for precursor and condensable organic species that were added in CMAQ-MADRID for the treatment of secondary organic aerosol (SOA) formation. Condensable gases typically contain multiple functional groups, such as aldehyde, acid, and alcohol groups. Without information on the identities of the condensable compounds in the Odum/Griffin et al. chamber experiments, deposition velocities of the organic gases are assumed to be analogous to that of higher aldehydes in MADRID 1. For the condensable products formed in CACM/MADRID 2, secondary condensable compounds were assigned dry deposition velocities based on their major functional groups, following one of three classes of compounds: aromatics, aldehydes, nitrates, and acids.

7.1.2 Particles

The treatment used for dry deposition of particles in CMAQ is based on the standard resistance approach.

$$V_d = \frac{1}{r_a + r_b + r_a\, r_b\, V_s} + V_s \qquad (7\text{-}1)$$

where V_d is the total dry deposition velocity of the particle, V_s is the gravitational settling (sedimentation) velocity, r_a is the aerodynamic resistance in the lower atmosphere and r_b is the resistance in the quasi-laminar layer near the surface. Venkatram and Pleim (1999) demonstrated that this approach does not conserve mass because the resistance component depends on a concentration gradient whereas the sedimentation term does not. They solved the particle dry deposition flux equation to obtain the following mass-conserving equation.

$$V_d = \frac{V_s}{1 - \exp\left(-(r_a + r_b)V_s\right)} \tag{7-2}$$

This expression of the dry deposition velocity for particles is used in CMAQ-MADRID. It is calculated for each particle size section and the dry deposition flux is calculated accordingly by size section.

7.2 Scavenging and Wet Deposition

7.2.1 Scavenging of Gases

Wet deposition is treated similarly in the CMU cloud module as in the RADM cloud module (Roselle and Binkowski, 1999). If precipitation occurs, the column from the surface to the cloud base is treated as being at equilibrium between the gas phase and the droplets. The CMU aqueous-phase chemistry module calculates the droplet concentrations of dissolved chemical species and activated particulate species in the cloud. Below the cloud, the droplet concentrations of the soluble gases are calculated using their Henry's law and the particles are assumed to be completely absorbed into the rain droplets. The column-weighted droplet concentrations are then multiplied by the precipitation rate to calculate the wet deposition fluxes.

In CMAQ-MADRID, the treatment of below-cloud scavenging of gases (washout), in both the CMU module and the RADM module is as follows. In the original CMAQ formulation, the solubility of gases into raindrops is calculated using the Henry's law constant. For chemical species that dissociate in aqueous solutions such as acids (e.g., HNO_3, HCl) and bases (e.g., NH_3), the solubility is then underestimated. In CMAQ-MADRID, we take into account the aqueous dissociation reactions by using the effective Henry's law constant.

For acid gases that dissociate once, the dissociation reaction is as follows.

$$HA(aq) \leftrightarrows H^+ + A^-$$

The effective Henry's law constant, $H_{HA,e}$ is calculated as follows,

$$H_{HA,e} = H_{HA,i} + \frac{K_{HA}}{[H^+]} \tag{7-3}$$

where $H_{HA,i}$ is the intrinsic Henry's law constant and K_{HA} is the aqueous dissociation equilibrium constant.

$$H_{HA,i} = \frac{[HA_{(aq)}]}{[HA_{(g)}]} \tag{7-4}$$

$$K_{HA} = \frac{[H^+][A^-]}{[HA_{(aq)}]} \tag{7-5}$$

This approach is used in CMAQ-MADRID for HNO_3, HCl, HNO_2, and HCOOH.

For acid gases that dissociate twice, the dissociation reactions are as follows,

$$H_2B \quad \leftrightarrows \quad H^+ + HB^-$$

$$HB^- \quad \leftrightarrows \quad H^+ + B^{2-}$$

The effective Henry's law constant, $H_{H_2B,e}$ is calculated as follows.

$$H_{H_2B,e} = H_{H_2B,i}\left(1 + \frac{K_{H_2B}}{[H^+]} + \frac{K_{H_2B} \cdot K_{HB^-}}{[H^+]^2}\right) \tag{7-6}$$

where $H_{H_2B,i}$ is the intrinsic Henry's law constant, K_{H_2B}, and H_{HB^-} are the aqueous dissociation equilibrium constants.

$$H_{H_2B,i} = \frac{[H_2B_{(aq)}]}{[H_2B_{(gas)}]} \tag{7-7}$$

$$K_{H_2B} = \frac{[H^+] \cdot [HB^-]}{[H_2B_{(aq)}]} \tag{7-8}$$

$$K_{HB^-} = \frac{[H^+] \cdot [B^{2-}]}{[HB^-]} \tag{7-9}$$

This approach is used in CMAQ-MADRID for SO_2 and CO_2.

For other important atmospheric gases such as H_2O_2 and HCHO, the dissociation or the hydrolysis reactions are as follows,

$$H_2O_2\,(aq) \quad \leftrightarrows \quad HO_2^- + H^+$$

$$HCHO(aq) + H_2O \quad \rightleftarrows \quad H_2C(OH)_2$$

The effective Henry's law constants are calculated as follows.

$$H_{H_2O_2,e} = H_{H_2O_2,i}\left(1+\frac{K_{H_2O_2}}{H^+}\right) \quad (7\text{-}10)$$

$$H_{HCHO,e} = H_{HCHO,i}\left(1+K_{HCHO}\right) \quad (7\text{-}11)$$

where $H_{H_2O_2,i}$ and $H_{HCHO,i}$ are the intrinsic Henry's law constants for H_2O_2 and HCHO, respectively, $K_{H_2O_2}$ is the aqueous dissociation equilibrium constant, and K_{HCHO} is the hydrolysis equilibrium constant.

For bases, the dissociation reaction is as follows.

$$B(aq)+H^+ \rightarrow BH^+$$

The effective Henry's law constant, $H_{B,e}$ is calculated as follows.

$$H_{B,e} = H_{B,i} + K_B[H^+] \quad (7\text{-}12)$$

where $H_{B,i}$ is the intrinsic Henry's law constant and K_B is the aqueous equilibrium constant.

$$H_{B,i} = \frac{B_{(aq)}}{B_{(g)}} \quad (7\text{-}13)$$

$$K_B = \frac{[BH^+]}{[B_{(aq)}][H^+]} \quad (7\text{-}14)$$

This approach is used in CMAQ-MADRID for NH_3.

A constant pH value of 4.0 is used for cloud/rain water to calculate the above Henry's law constants.

The rate of change due to scavenging, S_i, for in-cloud concentrations (m_i^{cld}) for each pollutant (i) following the cloud timescale (τ_{cld}) is given by (Byun and Ching, 1999):

$$S_i = \left.\frac{\partial m_i^{cld}}{\partial t}\right|_{scav} = m_i^{cld}\left(\frac{e^{-\beta_i \tau_{cld}}-1}{\tau_{cld}}\right) \quad (7\text{-}15)$$

where β_i is the scavenging coefficient for the pollutant. For subgrid convective clouds, τ_{cld} is 1 hour for grid resolved clouds; it is equal to the CMAQ's synchronization timestep. For gases, the scavenging coefficient is given by:

$$\beta_i = \left(\frac{1}{\tau_{washout} \left(1 + \frac{TWF}{H_i} \right)} \right) \tag{7-16}$$

where H_i is the effective Henry's law constant for the pollutant, *TWF* is the total water fraction given by:

$$TWF = \left(\frac{\rho_{H2O}}{\overline{W}_T RT} \right) \tag{7-17}$$

where ρ_{H2O} is the density of water, $\overline{W}_T$ is the mean total water content (kg/m^3), *R*, is the universal gas constant, and *T* is the in-cloud air temperature (K). The washout time, $\tau_{washout}$ represents the amount of time required to remove all of the water from the cloud volume at the specified precipitation rate (Λ_r), and is given by:

$$\tau_{washout} = \left(\frac{\overline{W}_T \, \Delta z_{cld}}{\rho_{H2O} \, \Lambda_r} \right) \tag{7-18}$$

where, Δz_{cld} is the cloud thickness.

7.2.2 Scavenging of Particles

As described in Section 5.2.1, large particles are assumed to be completely scavenged by cloud and rain water. The scavenging coefficient for those large particles is simply a function of the washout time:

$$\beta_{coarse} = \frac{1}{\tau_{washout}} \tag{7-19}$$

The concentrations of activated particles in cloud droplets, $m_{p,cld}(t)$, can be obtained by solving the following Equation,

$$\frac{dm_{p,cld}(t)}{dt} = S + P \tag{7-20}$$

where *S* and *P* are the rate of change in the concentrations of activated particles in cloud droplets due to in-cloud scavenging and aqueous-phase chemical production in cloud droplets, respectively. *S* can be obtained from Equation 7-15.

Small particles are partially scavenged by cloud and rain water according to Equation 5-1. The in-cloud concentrations of those activated particles are obtained by solving Equation 5-8.

7.2.3 Wet deposition of Gases and Particles

The wet deposition amount of gases and particles depends on the precipitation rate (Λ_r) and their concentrations in cloud water (m_i^{cld}), it can be calculated as follows (Byun and Ching, 1999):

$$wdep_i = \int_0^{\tau cld} m_i^{cld} \, \Lambda_r \, dt \qquad (7\text{-}21)$$

Deposition amounts are accumulated for each of the modeled species.

8
APPLICATION OF CMAQ-MADRID

The 3-D air quality model, CMAQ-MADRID, described above was applied to simulate the 27-28 August 1987 episode in the Los Angeles basin. Figure 8-1 shows the simulation domain and the locations of eight PM sampling sites in the basin. A comprehensive database of the Southern California Air Quality Study (SCAQS) is available that provides data needed for model inputs and evaluation. This episode has been used earlier for the evaluation of PM air quality models (see Seigneur, 2001) and, therefore, it provides a convenient benchmark. In the SCAQS simulation, the southwest corner of the modeling domain was placed at 33° 18' N latitude and 119° 24' W longitude. The horizontal grid system consists of 63 x 28 grid cells, with a grid resolution of 5 x 5 km^2. 30 layers of the MM5 grid system were mapped to 15 layers of CMAQ-MADRID, with a one to one mapping near the surface. The CBM-IV gas-phase chemical mechanism, the CMU aqueous-phase chemical mechanism, and the MADRID 1 aerosol module were used. Two size sections were used to represent the particle size distribution. The gas/particle mass transfer was simulated with the CMU hybrid approach. The heterogeneous reactions of HO_2, NO_2, NO_3, and N_2O_5 on the surface of particles and those of HO_2, NO_3, and N_2O_5 in the cloud droplets were accounted for.

8.1 Meteorology

The meteorological fields were simulated using the meteorological Mesoscale Model version 5 (MM5) with four-dimensional data assimilation. This MM5 simulation has been described previously (Hegarty et al., 1998) and used in previous air quality simulations (Pai et al., 2000; Seigneur et al., 2000a, 2000b). As discussed in these earlier results, the meteorological fields were mispredicted during daytime, particularly on 28 August, at inland locations. These mispredictions led to overestimated vertical mixing. To minimize the impact of such meteorological inputs on the air quality simulations, we added a post-processing step to the MM5 outputs by developing a diagnostic 4-D field of mixing heights using data available from acoustic sounders at 9 meteorological monitoring locations within the basin. A vertical diffusion coefficient of 1 m^2/s was used to represent these mixing heights.

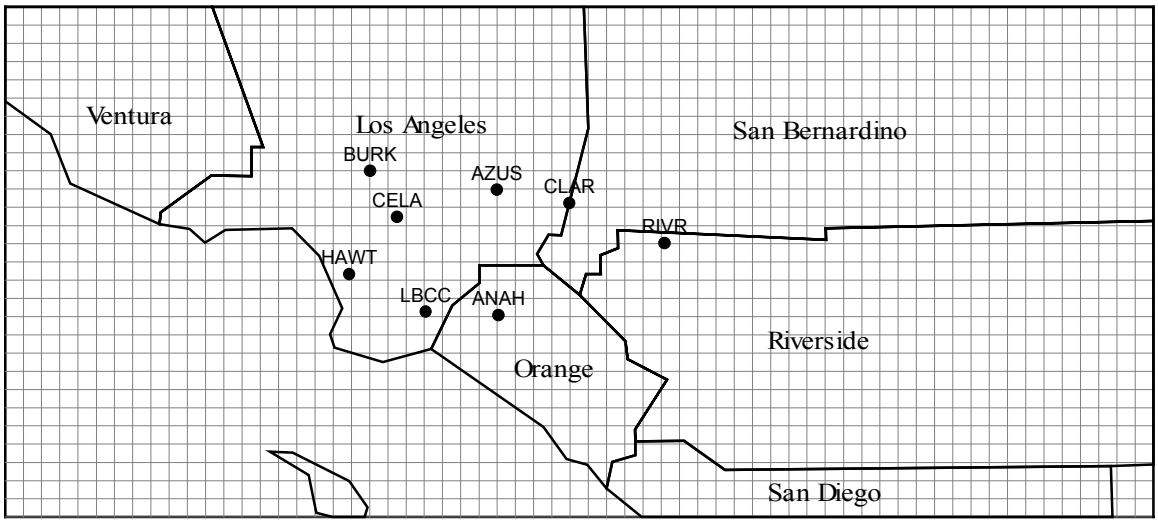

Figure 8-1
CMAQ-MADRID modeling domain and the PM measurement sites within the domain during SCAQS, 1987 (ANAH – Anaheim, AZUS – Azusa, BURK – Burbank, CELA – Downtown Los Angeles, CLAR – Claremont, HAWT – Hawthorne, LBCC – Long Beach, RIVR – Riverside/Rubidoux).

8.2 Emissions

Emissions of gases and particles generally follow Pai et al. (2000). The emissions of NO_x, CO, SO_2, SO_3, and speciated VOC are based on the 1987 SCAQS emission inventory of Allen and Wagner (1992). Because of the reported underestimation in motor vehicle VOC emissions and total VOC emissions (Harley et al., 1997 and Lu et al., 1997), the SCAQS motor vehicle VOC emissions were increased by a factor of 2.4 and the total VOC emissions were increased by a factor of 1.3 to bring the total VOC emissions in the inventory into agreement with the ratio of 8.8 for VOC/NO_x ambient concentrations. The emissions of NH_3 were obtained from Meng et al. (1998), which was originally based on the 1982 NH_3 emission inventory of Cass and Gharib (1984). Larger uncertainties remain in the PM emission inventory. The emissions of total $PM_{2.5}$ and $PM_{10-2.5}$ and the PM chemical speciation are also based on Meng et al. (1998). The chemical composition of PM emissions includes sulfate (SO_4^{2-}), sodium (Na^+), chloride (Cl^-), elemental carbon (EC), organic material (OM), and crustal material (OI) in fine (i.e., $PM_{2.5}$) and coarse (i.e., $PM_{10-2.5}$) size ranges. Two adjustments were made to the PM chemical speciation used by Meng et al. (1998). First, 71% of total EC emissions are assigned to the sub-2.5 μm size range. This value is based on the observed mean mass ratio of $EC_{2.5}$ to EC_{10} during this SCAQS episode. $EC_{2.5}$ accounts for 78% and 80% of total EC emissions in Meng et al. (1998) and Jacobson (1997b). However, $EC_{2.5}$ concentrations were overpredicted with a bias of 30-35% in both works. Second, we assumed that sea salt emissions are 32 tons/day with 10.3% in the sub-2.5 μm size range. Neither the SCAQMD nor the CARB emission inventory includes sea salt emissions which produce most of the sodium and chloride mass. Lurmann et al. (1997) and Meng et al. (1998) assumed a total NaCl emission of 75 tons/day with 29% in the sub-2.5 μm size range. Lurmann reported a moderate overprediction of sodium and chloride with bias of 38% and 24%,

respectively. The total oceanic area covered in the simulated domain in Meng et al. (1998) is roughly two times larger than that in our simulated domain. We scaled down the emission rate of 75 tons/day to 52 and 32 tons/day in two test simulations. Better agreement between simulated and observed sodium and chloride mass was obtained with 32 tons/day; this value was therefore used in our simulation.

8.3 Initial and Boundary Conditions

Initial conditions (IC) and boundary conditions (BC) for gases follow Pai et al. (2000). IC and BC for PM in the fine and coarse size ranges were speciated into sodium, chloride, sulfate, nitrate, ammonium, EC, OM, and other species using their observed concentrations in the two size ranges from San Nicholas Island, a "background" site during SCAQS 1987.

8.4 Results and Discussions

The SCAQS simulation was conducted for the period starting at 4:00 PST on August 25 and ending at 4:00 PST on August 29, 1987. The first two days were used as spin-up days to generate initial conditions for August 27. Results are analyzed and presented for August 27 and 28.

8.4.1 Predicted PM Chemical Composition at SCAQS Sampling Sites

Figures 8-2 to 8-5 show the observed and simulated 24-hr average concentrations for $PM_{2.5}$, PM_{10} and their compositions on August 27 and 28 at four sites: Hawthorne (HAWT), Los Angeles (CELA), Azusa (AZUS), and Riverside (RIVR). They represent an upwind coastal site in the western basin, a downtown area with high motor vehicle emissions, a mid-basin rural/suburban site, and a downwind urban site in the eastern basin, respectively. A factor of 1.4 was used to convert the observed OC concentrations to OM to be compared with the predicted OM concentrations (White and Roberts, 1977).

The observed concentrations at the four sites show the evolution of $PM_{2.5}$ and PM_{10} across the basin from the coast to the east. The observed PM concentrations were relatively low near the coast but became significantly higher as the air mass was transported across the basin. PM reached its highest level among all monitoring sites at RIVR on both days. The observed $PM_{2.5}$ and PM_{10} sulfate concentrations ranged across the basin from 5.7 to 10 $\mu g\ m^{-3}$ and 6.8 to 12 $\mu g\ m^{-3}$, respectively. The nitrate concentrations were relatively low near the coast, but increased significantly downwind of the NH_3 source areas in the eastern part of the basin, and the highest ammonium and nitrate concentrations occurred at RIVR. EC and OM concentrations were relatively low near the coast, but increased significantly in the downtown area and in the northern and eastern basin. AZUS had the highest $EC_{2.5}$ and OM_{10} concentrations on both days, the highest EC_{10} on August 27, and the highest $OM_{2.5}$ on August 28. The highest EC_{10} occurred at RIVR on August 28. The highest $OM_{2.5}$ occurred at CLAR on August 27 (not shown), a northern site close to AZUS ($OM_{2.5}$ at AZUS was the second highest across the basin).

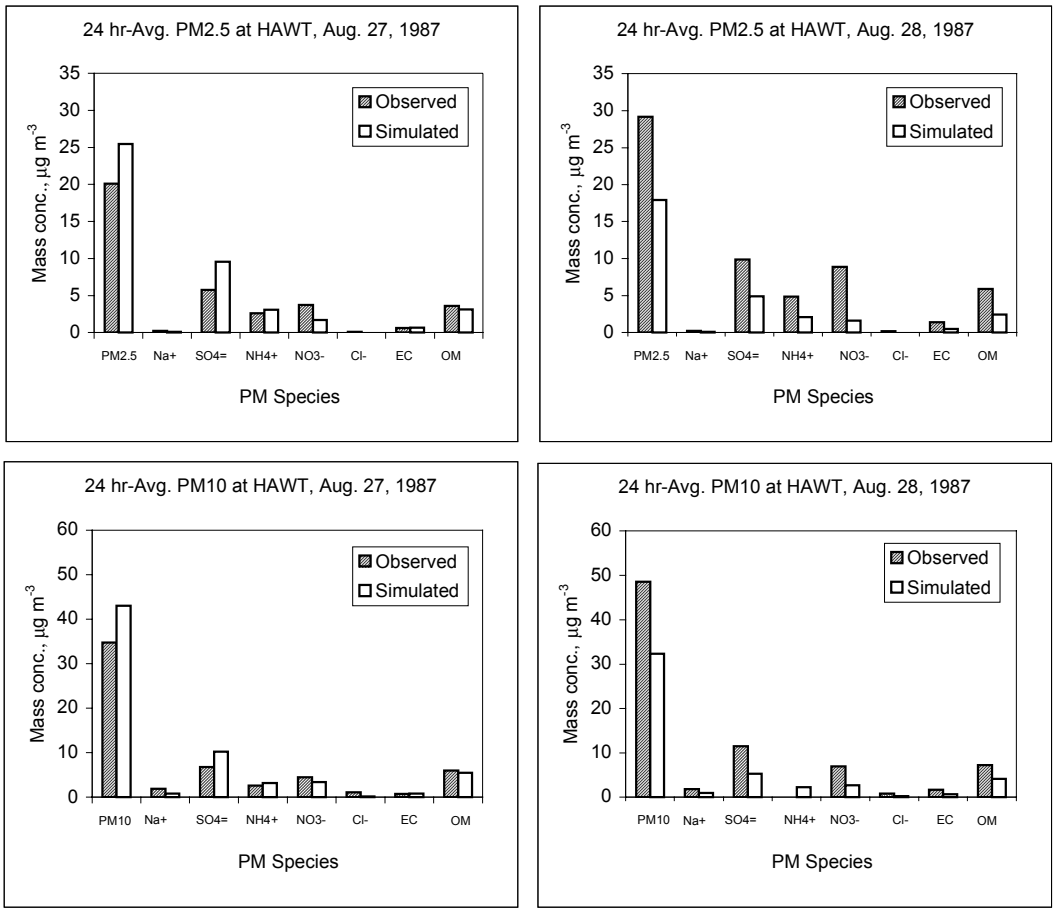

Figure 8-2
Observed and predicted 24-hr average concentrations for $PM_{2.5}$, PM_{10} and their chemical compositions on August 27-28, 1987 at Hawthorne (HAWT), CA.

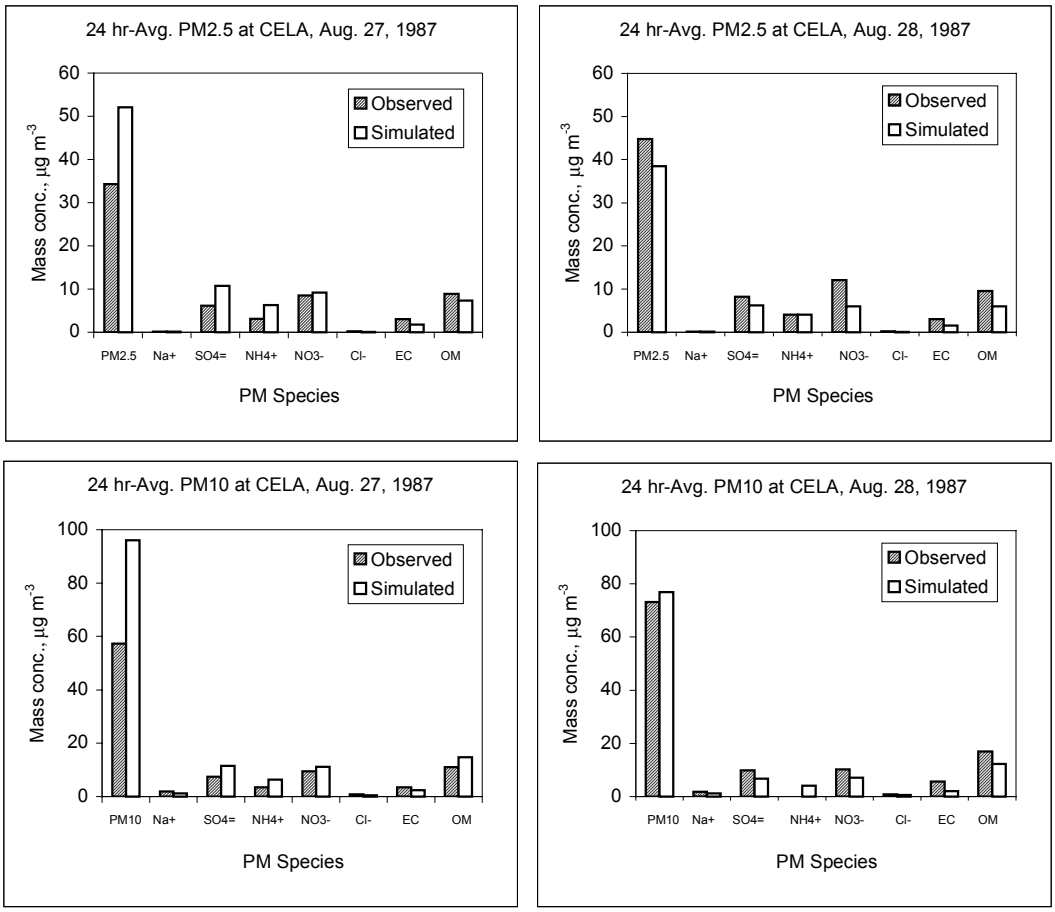

Figure 8-3
Observed and predicted 24-hr average concentrations for $PM_{2.5}$, PM_{10} and their chemical compositions on August 27-28, 1987 at Central Los Angeles (CELA), CA.

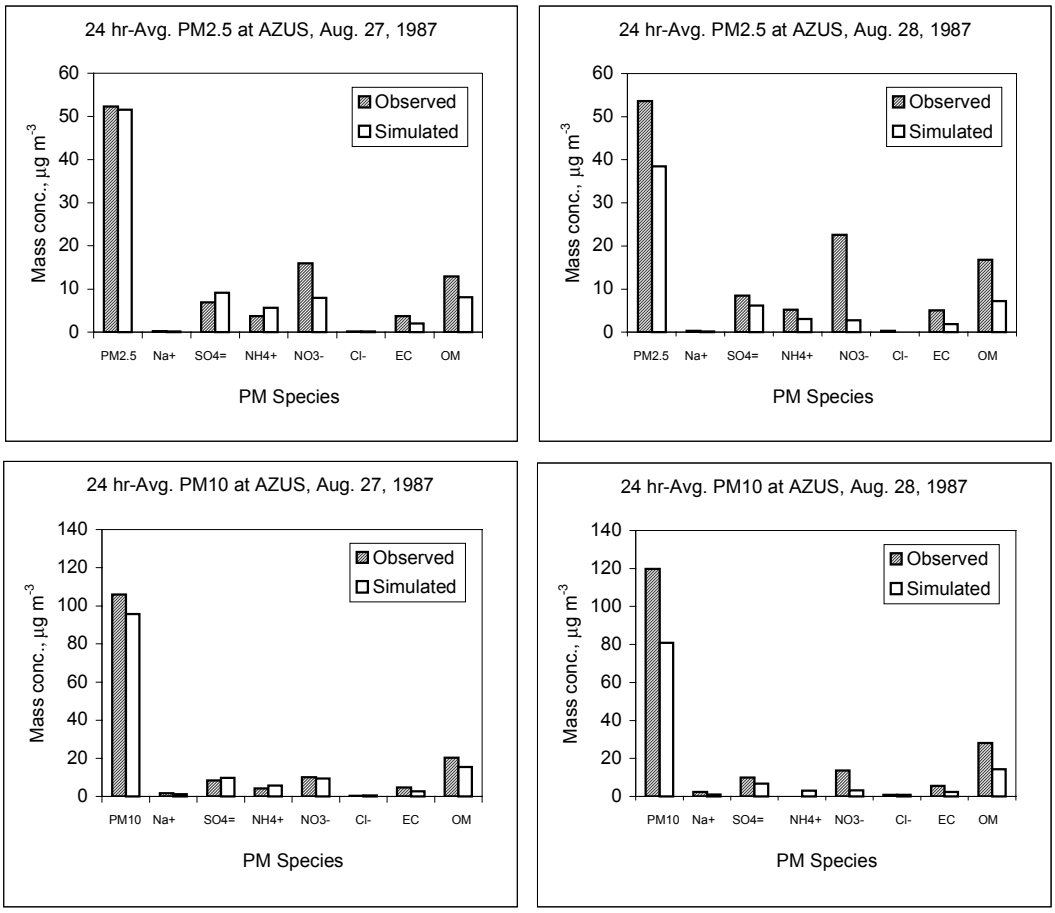

Figure 8-4
Observed and predicted 24-hr average concentrations for $PM_{2.5}$, PM_{10} and their chemical compositions on August 27-28, 1987 at Azusa (AZUS), CA.

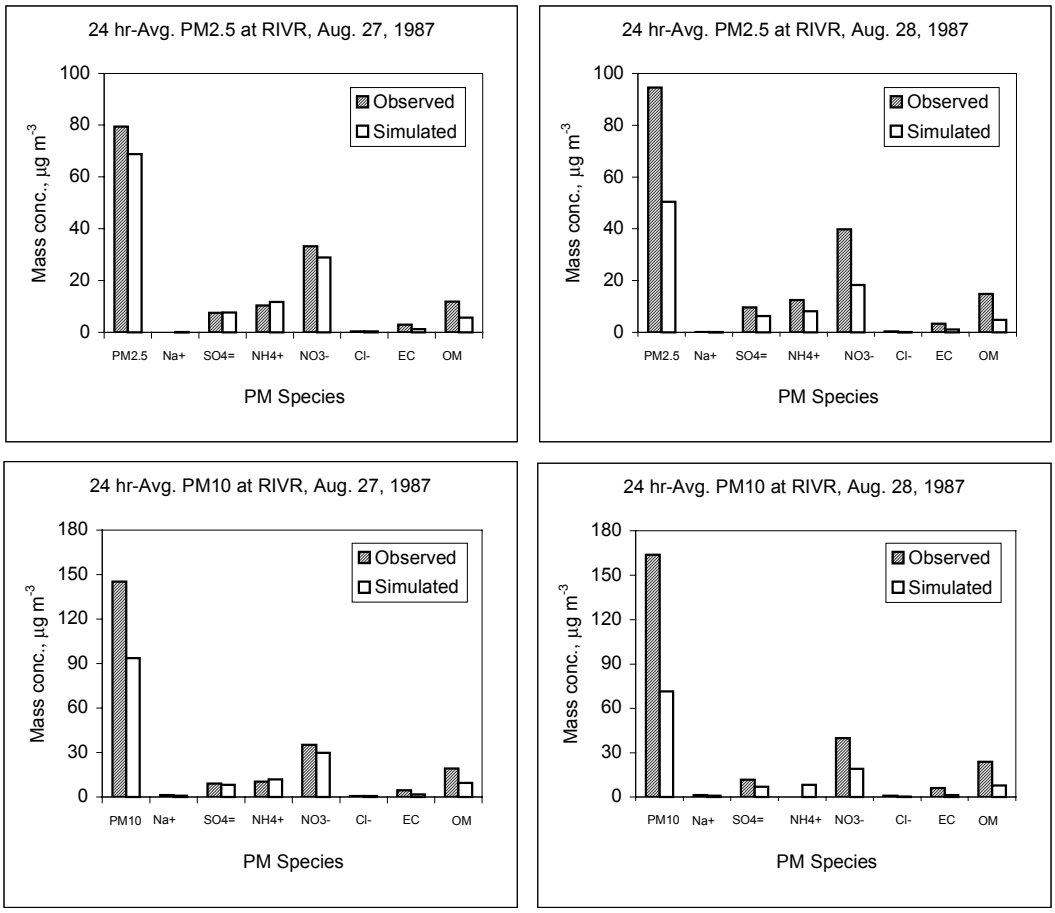

Figure 8-5
Observed and predicted 24-hr average concentrations for $PM_{2.5}$, PM_{10} and their chemical compositions on August 27-28, 1987 at Riverside (RIVR), CA.

The model reproduces well the observed evolution of PM and its composition. The predicted sulfate concentrations match quite well the observed values at all sites except at HAWT, where a moderate overprediction and underprediction occurred on August 27 and 28, respectively. The lowest and highest ammonium and nitrate concentrations were predicted at HAWT and RIVR, respectively, consistent with the observations. The predicted nitrate concentrations agree well with the observations at CELA and RIVR on August 27, but show moderate to significant underpredictions on August 28 and at other sites on both days. Better agreement is obtained between the simulated and observed ammonium at all sites. Moderate underprediction in EC concentrations occurred at almost all sites on both days. The OM concentration was underpredicted moderately near the coast and in the downtown area and significantly in some areas in the northern basin (e.g., at AZUS but not at CLAR) and downwind in the eastern basin on August 28. The OM predictions on August 27 show a much better agreement with observations at all sites. The predictions of sodium chloride are generally consistent with the observations, with a moderate underprediction at HAWT.

8.4.2 Model Performance Evaluation

We evaluated model performance following the guidance developed by Seigneur et al. (2000c). Our evaluation focuses on the mean bias and error in predicted O_3 and PM concentrations at the sampling sites. Table 8-1 shows the normalized gross errors and biases for 1-hr average O_3 concentrations and 24-hr average concentrations of $PM_{2.5}$, PM_{10} and their components averaged at all sampling sites on August 27 and 28, 1987. Table 8-1 also shows the ranges of the errors and biases obtained from simulations of SCAQS episodes with other 3-D air quality models including GATOR (Jacobson, 1997b), CIT (Meng et al., 1998), and UAM-AERO (Lurmann et al., 1997). GATOR and CIT were applied to the same episode whereas UAM-AERO was applied to a June 1987 episode.

The normalized gross error and bias in O_3 predictions at 38 sites are 36% and 20% for August 27 and 31% and -3% for August 28. The statistical values were calculated for each day using a low cutoff value of 40 ppb for O_3.

The statistical values for $PM_{2.5}$, PM_{10} and their components were calculated at 8 PM sampling sites in the modeling domain where measurements are available. The predicted mean $PM_{2.5}$ and PM_{10} concentrations at all 8 locations are 51.8 and 91.7 $\mu g\ m^{-3}$ on August 27, which moderately overpredict the mean observed values of 42.3 and 75.9 $\mu g\ m^{-3}$ by 21-22%. The predicted mean $PM_{2.5}$ and PM_{10} concentrations at all 8 locations are 43.4 and 81.3 $\mu g\ m^{-3}$ on August 28, which compare well with the observed values of 48.1 and 85.3 $\mu g\ m^{-3}$. The mean normalized gross error and bias in the predicted $PM_{2.5}$ concentrations are 42 and 30% on August 27 and 47 and -2% on August 28. The normalized gross error and bias in PM_{10} concentrations are slightly higher (53% and 33% for August 27 and 56% and 8% for August 28). The performance statistics for both $PM_{2.5}$ and PM_{10} are consistent with those obtained with the other three models.

The predicted $PM_{2.5}$ and PM_{10} sulfate concentrations match well the observations at all sites, with an error and bias of 27 to 49% and -27 to 49% for $PM_{2.5}$ sulfate and 35% and -35 to 32% for PM_{10} sulfate. These values are commensurate with those of other SCAQS studies. The predicted mean $PM_{2.5}$ and PM_{10} sulfate concentrations are 9.5 and 10.2 $\mu g\ m^{-3}$ on August 27 and 6.3 and 6.8 $\mu g\ m^{-3}$ on August 28. The corresponding observed values are 6.5 and 7.9 $\mu g\ m^{-3}$ on August 27 and 8.8 and 10.6 $\mu g\ m^{-3}$ on August 28. In addition to direct emissions within the basin, particulate sulfate concentrations are also affected by the upwind boundary conditions and the formation of H_2SO_4 via SO_2 oxidation. Large uncertainties exist in the particulate sulfate emissions and the upwind sulfate boundary concentrations, which may contribute to the moderate overprediction on August 27 and underprediction on August 28 in both $PM_{2.5}$ and PM_{10} sulfate. A boundary concentration of 2.1 and 2.6 $\mu g\ m^{-3}$ was used for $PM_{2.5}$ and PM_{10} sulfate, respectively, contributing to up to 35% of $PM_{2.5}$ and PM_{10} sulfate concentrations. The oxidation of SO_2 is slow in the absence of clouds but the gas-phase SO_2 oxidation produced up to 1.0 - 1.5 ppb of H_2SO_4 at the eight PM sampling sites, which may contribute up to 75% and 33% of hourly and 24-hr average concentrations of $PM_{2.5}$ sulfate, respectively, for this episode. The moderate overprediction on August 27 and underprediction on August 28 in particulate sulfate concentrations may, therefore, also result from the gas-phase formation of H_2SO_4 via SO_2 oxidation by OH radicals. OH is primarily produced through the photolytic reaction of O_3 and

subsequent hydrolysis reaction of $O(^1D)$ with H_2O. The predicted O_3 and water vapor concentrations on August 28 are lower than those on August 27 at most sites in the northern and eastern portions of the SCAQS domain (e.g., BURK, CELA, RIVR), resulting in relatively high total gas-phase oxidizing capacity (i.e., higher OH levels) on August 27 and relatively lower oxidizing capacity (i.e., lower OH levels) on August 28. At coastal sites (e.g., HAWT and LBCC) and one northern site (i.e., AZUS), the OH levels on August 28 are similar to those on August 27, but the predicted SO_2 concentrations are lower than those on August 27 due possibly to some biases in other predicted meteorological variables that affect diffusion and transport of chemical species. This could also contribute to lower H_2SO_4 formation on August 28 at those sites.

The predicted mean $PM_{2.5}$ and PM_{10} nitrate concentrations are, respectively, 10 and 11.6 $\mu g\ m^{-3}$ on August 27 and 7.5 and 8.4 $\mu g\ m^{-3}$ on August 28. The corresponding observed values are 13.2 and 12.1 $\mu g\ m^{-3}$ on August 27 and 16.6 and 13.5 $\mu g\ m^{-3}$ on August 28. Two measurement techniques were used to measure nitrate during SCAQS. The observed PM_{10} nitrate concentrations obtained with the Teflon filter were lower than the $PM_{2.5}$ nitrate concentrations measured with the denuder difference method, which is generally believed to be more accurate than the Teflon filter method. The discrepancies in $PM_{2.5}$ and PM_{10} nitrate measurements suggest that the Teflon filter method may underestimate nitrate mass. Consequently, the nitrate measurements obtained with the denuder difference method were used here. The normalized gross error and bias in predicted $PM_{2.5}$ nitrate concentrations are 29 and -25% on August 27 and 60 and -51% on August 28. The corresponding values in predicted PM_{10} nitrate concentrations are 25 and -1% on August 27 and 59 and -27% on August 28. While the model tends to overpredict nitrate mass at night, it underpredicts nitrate mass during the day, resulting in an underprediction in 24-hr average $PM_{2.5}$ nitrate concentrations on both days and in PM_{10} nitrate concentrations on August 28.

Table 8-1
Normalized gross errors and biases for 1-hr average O_3 and 24-hr average PM predictions averaged at all measurement sites on August 27 and 28, 1987[a].

	August 27		August 28		Other SCAQS Simulations	
Species	**Gross error, %**	**Bias %**	**Gross error, %**	**Bias %**	**Gross error, %**	**Bias %**
O_3[e]	36.2	20.3	31.0	-3.3	27.8[b]	-6.6[b]
$PM_{2.5}$ mass	41.5	30.1	46.9	-1.8	32 to 46[b,c,d]	-8 to 46[b,c,d]
PM_{10} mass	53.2	32.8	55.9	8.2	50.1 to 72[b,c]	-9.3 to 72[b,c]
$PM_{2.5}$ SO_4	48.7	48.7	27.0	-27.0	28.4 to 48[b,c,d]	-30 to 3.7[b,c,d]
PM_{10} SO_4	35	31.6	35.4	-35.4	26.3 to 40[b,c]	2 to –8.3[b,c]
$PM_{2.5}$ NH_4	61.3	61.3	43.6	-10.7	29 to 57[b,c,d]	-52.3 to 56[b,c,d]
PM_{10} NH_4	49.8	47.1	43.6	-19.2	23 to 45.7[b,c]	-0.2 to 12[b,c]
$PM_{2.5}$ NO_3	28.9	-24.8	59.5	-50.7	18 to 67.8[b,c,d]	-20.7 to 47[b,c,d]
PM_{10} NO_3	24.9	-0.7	58.9	-26.6	15 to 69.8[b,c]	6 to 18.4[b,c]
$PM_{2.5}$ EC	38.5	-17.2	69.7	-23.0	15 to 57.5[b,c,d]	-10 to 35[b,c,d]
PM_{10} EC	37.0	-17.9	60.3	-34.1	34 to 50.6[b,c]	-15 to 16.2[b,c]
$PM_{2.5}$ OM	38.4	-14.4	60.8	-28.2	38 to 49[b,c,d]	-44.1 to 14[b,c,d]
PM_{10} OM	53.6	16.9	64.6	-7.2	32 to 45.4[b,c]	0.3 to 5.8[b,c]
PM_{10} Na	39.1	-35.2	36.9	-33.7	36 to 47[b,c]	-30.2 to 38[b,c]
PM_{10} Cl	49.2	-34.4	79.8	2.7	24 to 46.8[b,c]	16 to 24[b,c]

a. The mean normalized gross error and bias are defined as:

$$\sum_{i=1}^{N} \frac{|P_i - O_i|}{O_i} \qquad \textit{and} \qquad \sum_{i=1}^{N} \frac{(P_i - O_i)}{O_i}$$

where P_i and O_i are the predicted and observed values for location and time period I, and N is the total number of data pairs.

b. Jacobson, 1997b, statistics are for average values over eight PM sampling sites for August 27-28, 1987.

c. Lurmann et al., 1997, statistics are for 24-hr average values over eight sites for June 25, 1987.

d. Meng et al., 1998, statistics are for 24-hr average values over eight sites for August 28, 1987.

e. A cutoff mixing ratio of 40 ppb was used in the calculation of O_3 statistics.

The formation of particulate nitrate occurs when HNO_3 dissolves into droplets or condenses on the surface of particles through a chemical conversion process (e.g., formation of ammonium nitrate or sodium nitrate). The reversed process can also occur under some ambient conditions (e.g., conditions with high temperature and low relative humidity (RH)) due to the volatility of particulate nitrate. HNO_3 is formed primarily by gas-phase reaction of NO_2 with OH during daytime and by gas-phase reaction of NO_2 with O_3 forming NO_3 and subsequent gas-phase or heterogeneous reactions of NO_3 at night. The condensation of HNO_3 on the surface of particles tends to dominate the formation of nitrate during daytime in the absence of fog or clouds. At night, both the condensation of HNO_3 on the surface of wetted and colder particles and the heterogeneous reactions of nitrogen species such as N_2O_5 and NO_3 on the surface of wetted particles can be dominant processes. Particulate nitrate formation is enhanced with high NH_3 concentrations, high RH levels and low temperature. NH_4NO_3 becomes deliquescent at an RH of 61.4% at 25°C and 1 atm and at an even lower RH (e.g., 50%) when several mixtures co-exist in the aqueous/particulate phase. Solid NH_4NO_3 will typically be present at RH values lower than 50% under sulfate-poor and ammonium-rich condition, which covered most of areas in the SCAQS domain during morning and late afternoon or early evening. Thus, the formation of particulate nitrate can be limited by the abundance of HNO_3 (i.e., NO_x-limited), NH_3 (i.e., NH_3-limited) or ambient water vapor (i.e., H_2O-limited), depending on the chemical and meteorological conditions at a specific location. Therefore, the accuracy in nitrate predictions depends not only on the accuracy of the emissions of precursors such as NO_x and NH_3 but also on the accuracy of the gas-phase chemistry, aqueous-phase chemistry and gas-to-particle conversion processes simulated in the model as well as the accuracy of the meteorological inputs.

Few clouds were present during this SCAQS episode, therefore, HNO_3 formation was governed primarily by gas-phase reactions and to a lesser extent heterogeneous reactions. Gas-to-particle conversion was simulated in this MADRID simulation with the CMU hybrid approach. ISORROPIA is used to calculate the particulate chemical concentrations. ISORROPIA has been shown to produce better fine ammonium and nitrate predictions than SEQUILIB (Nenes et al., 1999) (SEQUILIB was used in the simulations of SCAQS June 24-26 episode of Lurmann et al., 1997). In addition, we tested the performance of ISORROPIA under 400 cases typical of the atmospheric conditions in the eastern and the western U.S. and found that the predictions of total PM and its chemical composition by ISORROPIA are comparable with those predicted by the more comprehensive equilibrium modules such as SCAPE2 and EQUISOLV that were used in the CIT and GATOR models, respectively. The underpredictions in the particulate nitrate concentration are, therefore, unlikely related to the model treatment of gas-to-particle conversion in MADRID.

There were generally sufficient amounts of HNO_3 on both days at many locations. Underpredictions in NH_3 concentrations may contribute to the underpredictions of particulate nitrate concentrations at some western and central sites such as HAWT and ANAH on August 28 when the formation of NH_4NO_3 was NH_3-limited. The predicted low NH_3 concentrations during daytime may also contribute to low nitrate formation at other inland locations, especially in the eastern domain. Underestimation of the ambient RH during daytime is likely another factor that contributed to the underprediction of particulate nitrate. For example, the observed daytime RH values during August 27-28 range from 65-83% at Hawthorne (HAWT) and 28-60% at Riverside

(RIVR), while the predicted daytime RH values range from 44-75% at HAWT and 16-45% at RIVR. Therefore, the low predicted RH limited to some extent the dissolution and condensation of HNO_3, resulting in lower nitrate formation during daytime on both days.

The biases in predicted meteorological fields may also have affected particulate ammonium concentrations that depend on the accuracy of the precursor emissions and the predicted meteorological conditions. The predicted mean $PM_{2.5}$ and PM_{10} ammonium concentrations are 6.2 and 6.3 μg m^{-3} on August 27, which are higher by 51 and 40% than the observed values of 4.1 and 4.5 μg m^{-3}. The predicted mean $PM_{2.5}$ and PM_{10} ammonium concentrations are 4.6 and 4.7 μg m^{-3} on August 28, which are lower by 18 and 19% than the observed values of 5.6 and 6.1 μg m^{-3}. The normalized mean error and bias at all 8 sites are 61% on August 27 and 44% and -11% on August 28 for predicted $PM_{2.5}$ ammonium concentrations and 50% and 47% on August 27 and 44% and -19% on August 28 for predicted PM_{10} ammonium concentrations. The NH_3 emission inventory used here was based on 1982 NH_3 emissions estimated by Cass and Gharib (1984); therefore, it may not accurately reflect the actual total NH_3 emissions and their regional distributions in 1987. Also, since the particulate $PM_{2.5}$ sulfate concentrations are dominated by ammonium sulfate, the moderate overprediction on August 27 and underprediction on August 28 in particulate sulfate and ammonium are highly correlated. The underprediction in particulate ammonium on August 28 also correlates with the underprediction in particulate nitrate, due to the presence of NH_4NO_3 in the particulate phase.

The predicted mean $PM_{2.5}$ and PM_{10} EC mass are, respectively, 1.8 and 2.3 μg m^{-3} on August 27 and 1.7 and 2.2 μg m^{-3} on August 28. These values are lower than the observed values of 2.5 and 3.3 μg m^{-3} on August 27 and 2.8 and 4.0 μg m^{-3} on August 28. As discussed above, large uncertainties exist in the PM emission inventory that affects the predicted EC concentrations.

The predicted mean $PM_{2.5}$ OM concentrations are 7.3 and 6.8 μg m^{-3} on August 27 and 28; these values are lower by 22 and 40% than the observed values of 9.4 and 11.4 μg m^{-3}. The predicted PM_{10} OM concentrations are 13.9 and 13.0 μg m^{-3} on August 27 and 28; the corresponding observed values are 13.6 and 16.9 μg m^{-3}. The normalized mean error and bias at all 8 sites are 38 and -14% on August 27 and 61% and -28% on August 28 for $PM_{2.5}$ OM concentrations and 54% and 17% on August 27 and 65% and -7% on August 28 for PM_{10} OM concentrations. Those values are generally consistent with those obtained in earlier SCAQS simulations; except for slightly higher error for $PM_{2.5}$ and PM_{10} OM predictions on August 28 and a slightly higher bias for PM_{10} OM predictions on August 27.

The predicted PM_{10} sodium concentrations agree well with observations at all sites, with average error and bias of 37 to 39% and -35 to -34%, respectively, whereas the statistics deteriorate somewhat for the predicted PM_{10} chloride mass with average error and bias of 49 to 80% and -34 to 3%, respectively. The predicted mean PM_{10} sodium and chloride concentrations are 1.1 and 0.5 μg m^{-3} on August 27 and 1.1 and 0.73 μg m^{-3} on August 28. The corresponding observed values are 1.7 and 0.76 μg m^{-3} on August 27 and 1.7 and 0.72 μg m^{-3} on August 28. The large mean error in the predicted PM_{10} chloride on August 28 resulted from a significant overprediction in terms of percentage in PM_{10} chloride concentration at Anaheim (ANAH) and Long Beach

(LBCC) (1.8 and 1.2 μg m^{-3}, respectively), where a low 24-hr average PM_{10} chloride concentration of 0.5 μg m^{-3} was observed. For comparison, the observed 24-hr average PM_{10} chloride concentrations were 0.77 μg m^{-3} at HAWT and 0.75-0.86 μg m^{-3} at the other sites located in the central, northern, and eastern portions of the domain. It is not clear why the observed 24-hr average PM_{10} chloride concentrations at ANAH and LBCC were even lower than those at other sites further away from the Pacific ocean. The low observed values at the two coastal sites suggest that significant uncertainties may exist in chloride data collected during the SCAQS episode. Also, the sea salt emissions used for this SCAQS episode are quite uncertain.

8.5 Summary

CMAQ-MADRID was applied to simulate an air pollution episode in the Los Angeles basin. Model performance was shown to be consistent with existing guidance. The evolution of the chemical composition of PM from the coastal areas to the inland areas was well reproduced by the model except that SOA and particulate nitrate formation were underpredicted. The underpredictions in nitrate are due mainly to underpredictions in the relative humidity and uncertainties in the emissions of primary pollutants such as VOC, NO_x and NH_3. The treatment of SOA formation is still an area of ongoing research and large uncertainties currently exist for this PM component in all existing air quality models.

9
REFERENCES

Abdul-Razzak, H., Ghan, S.J. and Rivera-Carpio, C., 1998. A parameterization of aerosol activation 1. Single aerosol type, *J. Geophys. Res.*, **103**, 6123-6131.

Abdul-Razzak, H. and Ghan, S.J., 1999. A parameterization of aerosol activation 2. Multiple aerosol types, *J. Geophys. Res.*, submitted.

Allen, P.D. and K.K. Wagner, 1987. *SCAQS Emission Inventory*, magnetic tape numbers ARA806 and ARA807; Technical Support Division, California Air Resources Board: Sacramento, CA, 1992.

Bilde, M. and S.N. Pandis, 2001. Evaporation rates and vapor pressures of individual aerosol species formed in the atmospheric oxidation of α- and β-Pinene, *Environ. Sci. Technol.*, **35**, 3344-3349.

Binkowski, F.S. and U. Shankar, 1995. The regional particulate matter model. 1: Model description and preliminary results, *J. Geophys. Res.*, **100**, 26191-26209.

Bott, A., 1989. A positive definite advection scheme obtained by nonlinear renormalization of the advective fluxes, *Mon. Wea. Rev.*, **117**, 1006-1015.

Byun, D.W. and J.K.S. Ching, 1999. Science Algorithms of the EPA Models-3 Community Multiscale Air Quality (CMAQ) Modeling System, EPA/600/R-99/030, Office of Research and Development, U.S. Environmental Protection Agency, Washington, D.C.

Capaldo, K.P., C. Pilinis and S.N. Pandis, 2000. A computationally efficient hybrid approach for dynamic gas/aerosol transfer in air quality models, *Atmos. Environ.*, **34**, 3617-3627.

Cheung, J. L., Y. Q. Li, J. Boniface, Q. Shi and P. Davidovits, 2000. Heterogeneous interactions of NO_2 with aqueous surfaces, *J. Phys. Chem.*, **104**, 2655-2662.

Chock, D.P. and S.L. Winkler, 2000. A trajectory-grid approach for solving the condensation and evaporation equations of aerosols, *Atmos. Environ.*, **34**, 2957-2973.

References

Clegg, S.L., P. Brimblecombe and A.S. Wexler, 1998a. A thermodynamic model of the system H^+ -NH_4^+ -Na^+ -SO_4^{2-} -NO_3^- -Cl^- -H_2O at 298.15 K, *J. Phys. Chem.*, **102**, 2155-2171.

Clegg, S.L., P. Brimblecombe and A.S. Wexler, 1998b. A thermodynamic model of the system H^+ -NH_4^+ -Na^+ -SO_4^{2-} -NO_3^- -Cl^- -H_2O at tropospheric temperatures, *J. Phys. Chem.*, **102**, 2137-2154.

Dassios K.G. and S.N. Pandis, 1999. The mass accommodation coefficient of ammonium nitrate aerosol, *Atmos. Environ.*, **33**, 2999-3003.

Drefahl, A. and M. Reinhard, 1995. Handbook of Estimating Physico-Chemical Properties of Organic Compounds, Stanford Bookstore, Stanford, CA.

EPA, 2001. Guidance for Demonstrating Attainment of Air Quality Goals for $PM_{2.5}$ and Regional Haze, Draft, Office of Air Quality Planning and Standards, U.S. Environmental Protection Agency, Research Triangle Park, NC.

EPRI, 1999. Organic Aerosol Partition Module Documentation, TR-113095, EPRI, Palo Alto, CA.

Fitzgerald, J.W., W.A. Hoppel and F. Gelbard, 1998. A one-dimensional sectional model to simulate multicomponent aerosol dynamics in the marine boundary layer. 1. Modal description, *J. Geophys. Res.*, **103**, 16085-16102.

Ghan, S.J., C.C. Chuang and J.E. Penner, 1993. A parameterization of cloud droplet nucleation, I. Single aerosol type, *Atmos. Res.*, **30**, 197-221.

Ghan, S.J., C.C. Chuang, R.C. Easter, and J.E. Penner, 1995. A parameterization of cloud droplet nucleation, II. Multiple aerosol types, *Atmos. Res.*, **36**, 39-54.

Gillani, N.V., S.E. Schwartz, W.R. Leaitch, J.W. Strapp and G.A. Isaac, 1995. Field observations in continental stratiform clouds: Partitioning of cloud particles between droplets and unactivated interstitial aerosols, *J. Geophys. Res.*, **100**, 18687-18706.

Griffin, R.J., 2000. Private communication, California Institute of Technology, Pasadena, CA.

Griffin, R.J., D.R. Cocker III, R.C. Flagan and J.H. Seinfeld, 1999. Organic aerosol formation from the oxidation of biogenic hydrocarbons, *J. Geophys. Res.*, **104**, 3555-3567.

Griffin, R.J., D. Dabdub and J.H. Seinfeld, 2002. Secondary organic aerosol: I Atmospheric chemical mechanism for production of molecular constituents, *J. Geophys. Res.*, in press.

Harley, R., R.F. Sawyer and J.B. Milford, 1997. Updated photochemical modeling for California South Coast Air Basin: Comparison of chemical mechanisms and motor vehicle emission inventories, *Environ. Sci. Technol.*, **31**, 2829-2839.

Harrington, D. Y. and S. M. Kreidenweis, 1998. Simulation of Sulfate Aerosol Dynamics. I. Model Description. *Atmos. Environ.*, **32**, 1691-1700.

Hegarty, J., M. Leidner and M. Iacono, 1998. Modeling air pollution in the Los Angeles Basin using the MM5-SAQM modeling system. Part I: meteorological simulations. "In Proceedings of the 10th Joint Conference on the Applications of Air Pollution Meteorology with the A&WMA; Phoenix, AZ, January 11-16.

Hoppel, W.A., G.M. Frick and J.W. Fitzgerald, 1996. Deducing droplet concentration and supersaturation in marine boundary layer clouds from surface aerosol measurements, *J. Geophys. Res*., **101**, 26553-26565.

Jacob, D., 2000. Heterogeneous chemistry and tropospheric ozone, *Atmos. Environ.*, **34**, 2132-2159.

Jacob, D., 2001. Private communication, Division of Engineering and Applied Science, Harvard University, Cambridge, MA.

Jacobson, M.Z., 1997a. Development and application of a new air pollution modeling system – II. Aerosol module structure and design, *Atmos. Environ.*, **31**, 131-144.

Jacobson, M.Z., 1997b. Development and application of a new air pollution modeling system – Part III. Aerosol-phase simulations, *Atmos. Environ.*, **31**, 587-608.

Jacobson, M.Z., 1999. Studying the effects of calcium and magnesium on size-distributed nitrate and ammonium with EQUISOLV II, *Atmos. Environ.*, **33**, 3635-3649.

Jacobson, M.Z. and R.P. Turco, 1995. Simulating condensational growth, evaporation, and coagulation of aerosols using a combined moving and stationary size grid, *Aerosol Sci. Technol.*, **22**, 29-92.

Kerminen, V.M. and A.S. Wexler, 1994. Post-Fog Nucleation of H_2SO_4 – H_2O Particle in Smog, *Atmos. Environ.*, **28**, 2399-2406.

Kim, Y.P. and J.H. Seinfeld, 1995. Atmospheric gas-aerosol equilibrium III: thermo-dynamics of crustal elements Ca^{2+}, K^{+}, and Mg^{2+}, *Aerosol Sci. Technol.*, **22**, 93-110.

Lamb B., D. Grosjean, B. Pun, and C. Seigneur, 1999. Review of the Emissions, Atmospheric Chemistry, and Gas/Particle Partition of Biogenic Volatile Organic Compounds and Reaction Products, CRC Report A-23-1, Coordinating Research Council, Inc., Alpharetta, Georgia.

Leaitch, W.R., 1996. Observations pertaining to the effect of chemical transformation in cloud on the anthropogenic aerosol size distribution, *Aerosol Sci. Technol.*, **25**, 157-173.

Leaitch, W.R., C.M. Banic, G.A. Isaac, M.D. Couture, P.S.K. Liu, I. Gultepe and S.M. Li, 1996. Physical and chemical observations in marine stratus during the 1993 North Atlantic Regional Experiment: Factors controlling cloud droplet number concentrations, *J. Geophys. Res.*, **101**, 29123-29135.

Liu, P.S.K., W.R. Leaitch, C.M. Banic, S.M. Li, D. Ngo and W.J. Megaw, 1996. Aerosol observations at Chebogue Point during the 1993 North Atlantic Regional Experiment: Relations among cloud condensation nuclei, size distribution, and chemistry, *J. Geophys. Res.*, **101**, 28971-28990.

Lu, R., R.P. Turco and M.Z. Jacobson, 1997. An integrated air pollution modeling system for urban and regional scales: 2. Simulations for SCAQS 1987, *J. Geophys. Res.*, **102**, 6081-6098.

Lurmann, F.W., A.S. Wexler, S.N. Pandis, S. Musarra, N. Kumar and J.H. Seinfeld, 1997. Modeling urban and regional aerosols - II. Application to California's south coast air basin, *Atmos. Environ.*, **31**, 2695-2715.

McMurry, P.H. and S.K. Friedlander, 1979. New particle formation in the presence of an aerosol, *Atmos. Environ.*, **13**, 1635-1651.

Meng, Z., J.H. Seinfeld, P. Saxena and Y.P. Kim, 1995. Atmospheric gas-aerosol equilibrium, IV: thermodynamics of carbonates, *Aerosol Sci. Technol.*, **23**, 131-154.

Meng, Z., D. Dabdub and J.H. Seinfeld, 1998. Size-resolved and chemically resolved model of atmospheric aerosol dynamics, *J. Geophys. Res.*, 103, 3419-3435.

Nenes, A., S.N. Pandis and C. Pilinis, 1998. ISORROPIA: A new thermodynamic equilibrium model for multiphase multicomponent inorganic aerosols, *Aquatic Geochemistry*, **4**, 123-152.

Nenes, A., C. Pilinis and S.N. Pandis, 1999. Continued development and testing of a new thermodynamic aerosol module for urban and regional air quality models, *Atmos. Environ.*, **33**, 1553-1560.

Nguyen, K. and D. Dabdub, 2002. Semi-Langrangian flux scheme for the solution of the aerosol condensation/evaporation equation, *Aerosol Sci. Technol.*, **36**, 407-418.

Odum, J.R., T.P.W. Jungkamp, R.J. Griffin, H.J.L. Forstner, R.C. Flagan and J.H. Seinfeld, 1997. Aromatics, reformulated gasoline, and atmospheric organic aerosol formation, *Environ. Sci. Technol.*, **31**, 1890-1897.

Pai, P., K. Vijayaraghavan, C. Seigneur, 2000. Particulate matter modeling in the Los Angeles Basin using SAQM-AERO, *J. Air Waste Manage. Assoc.*, **50**, 32-42.

Pandis, S.N. and J.H. Seinfeld, 1989. Sensitivity analysis of a chemical mechanism for aqueous-phase atmospheric chemistry, *J. Geophys. Res.*, **94**, 1105-1126.

Pandis, S.N., L.M. Russell and J.H. Seinfeld, 1994. The relationship between DMS flux and CCN concentration in remote marine regions, *J. Geophys. Res.*, **99**, 16945-16957.

Pankow, J.F., 1994. An absorption model of the gas/aerosol partition involved in the formation of secondary organic aerosol, *Atmos. Environ.*, **28**, 189-193.

Pilinis, C. and J.H. Seinfeld, 1987. Continued development of a general equilibrium model for inorganic multicomponent atmospheric aerosols, *Atmos Environ.*, **32**, 2453-2466.

Press, W.H., S.A. Teukolsky, W.T. Vetterling and B.P. Flannery, 1992. Numerical recipes in C, Diskette v.2.08, Cambridge University Press, NY, NY, Chapter 9.7.

Pruppacher, H.R. and J.D. Klett, 1978. Microphysics of Clouds and Precipitation, Reidel, Dordrecht, Holland.

Pun, B.K., 1998. Treatment of Uncertainties in Atmospheric Chemical Systems: A Combined Modeling and Experimental Approach, Ph.D. Thesis, Massachusetts Institute of Technology, Cambridge, MA.

Pun, B.K., R.J. Griffin, C. Seigneur and J.H. Seinfeld, 2002a. Secondary organic aerosol: II. Thermodynamic model for gas/particle partitioning of molecular constituents, *J. Geophys. Res.*, in press.

Pun, B., Y. Zhang, S.-Y. Wu, K. Vijayaraghavan, and C. Seigneur, 2002b. Models-3/Community Multiscale Air Quality Model (CMAQ) User's Guide to Alternative Particulate Matter and Cloud Modules, EPRI, Palo Alto, CA.

Roselle, S.J. and F.S. Binkowski, 1999. Cloud dynamics and chemistry, Chapter 11 in Science Algorithms of the EPA Models-3 Community Multiscale Air Quality (CMAQ) Modeling System, D.W. Byun and J.S. Ching, eds., EPA/600/R-99/030, U.S. Environmental Protection Agency, Washington, D.C.

Santos, L., R.I. Sykes, P. Karamchandani, C. Seigneur, F. Lurmann and R. Arndt, 1999. Second-order Closure Puff Model with Aqueous-Phase Chemistry and Aerosols, Report to EPRI, Palo Alto, CA.

Saxena, P. and L.M. Hildemann, 1996. Water-soluble organics in atmospheric particles: a critical review of the literature and application of thermodynamics to identify candidate compounds, *J. Atmos. Chem.*, **24**, 57-109.

Seigneur, C., 1982. A model of sulfate aerosol dynamics in atmospheric plumes, *Atmos. Environ.*, **16**, 2207-2228.

Seigneur, C., 2001. Current status of air quality modeling for particulate matter, *j. Air Waste Manage. Assoc.*, **51**, 1508-1521.

Seigneur, C. and P. Saxena, 1984. A study of atmospheric acid formation in different environments, *Atmos. Environ.*, **18**, 2109-2124.

Seigneur, C., A. B. Hudischewskyi, J. H. Seinfeld, K. T. Whitby, E. R. Whitby, J. R. Brock and H. M. Barnes, 1986. Simulation of aerosol dynamics: A comparative review of mathematical models, *Aerosol Sci. Technol.*, **5**, 205-222.

Seigneur, C. and P. Saxena, 1988. A theoretical investigation of sulfate formation in clouds, *Atmos. Environ.*, **22**, 101-115.

Seigneur, C., P. Pai, P. Hopke and D. Grosjean, 1999. Modeling atmospheric particulate matter, *Environ. Sci. Technol.*, **33**, 80A-84A.

Seigneur, C., P. Karamchandani, P. Pai, K. Vijayaraghavan, K. Lohman and S.Y. Wu, 2000a. Model comparisons and application of Models-3/CMAQ APT. First Annual Models-3 Workshop, 12-14 June 2000, Arlington, Virginia.

Seigneur, C., C. Tonne, K. Vijayaraghavan and P. Pai, 2000b. Sensitivity of $PM_{2.5}$ source-receptor relationships to atmospheric chemistry and transport in a three-dimensional air quality model, *J. Air Waste Manage. Assoc.*, **50**, 428-435.

Seinfeld, J.H. and S.N. Pandis, 1998. Atmospheric Chemistry and Physics - From Air Pollution to Climate Change, John Wiley & Sons, Inc., New York, NY.

Seinfeld, J.H., R.J. Griffin, B.K. Pun, C. Seigneur and D. Dabdub, 2002. Thermodynamics Organic Atmospheric Aerosols, Contract #98-314, Air Resources Board, Sacramento, CA.

Squires, P., 1958. The microstructure and colloidal stability of warm clouds, II, The causes of the variations in microstructure, *Tellus*, **10**, 262-271.

Strader, R., C. Gurciullo, S. Pandis, N. Kumar and F.W. Lurmann, 1998. Development of gas-phase chemistry secondary organic aerosol, and aqueous-phase chemistry modules for PM modeling, STI Final Report to Coordinating Research Council, Atlanta, GA.

Tao, Y. and P.H. McMurry, 1989. Vapor pressures and surface free energies of C14-C18 monocarboxylic acids and C5 and C6 dicarboxylic acids, *Environ. Sci. Technol.*, **23**, 1519-1523.

Twomey, S., 1959. The nuclei of natural cloud formation, II, The supersaturation in natural clouds and the variation of cloud droplet concentration, *Geophys. Pura Appl.*, **43**, 243-249.

Venkatram, A. and J. Pleim, 1999. The electrical analogy does not apply to modeling dry deposition of particles, *Atmos. Environ.*, **33**, 3075-3076.

Walcek, C.J. and G.R. Taylor, 1986. A theoretical method for computing vertical distributions of acidity and sulfate production within cumulus clouds, *J. Atmos. Sci.*, **43**, 339-355.

Wexler A.S. and J.H. Seinfeld, 1990. The distribution of ammonium salts among a size and composition dispersed aerosol, *Atmos. Environ.*, **24A**, 1231-1246.

White W.H. and P.T. Roberts, 1977. On the nature and origins of visibility-reducing aerosols in the Los Angeles air basin, *Atmos. Environ.*, **11**, 803-812.

Zhang, Y., C.H. Bischof, R.C. Easter, P.-T. Wu, 1998. Sensitivity analysis of a mixed phase chemical mechanism using automatic differentiation, *J. Geophys. Res.*, **103**, 18953-18979.

Zhang, Y. and G. Carmichael, 1999. The role of mineral aerosol in tropospheric chemistry in East Asia-A model study, *J. Appl. Meteor.*, **38**, 353-366.

Zhang, Y., C. Seigneur, J.H. Seinfeld, M.Z. Jacobson and F.S. Binkowski, 1999. Simulation of aerosol dynamics: A comparative review of algorithms used in air quality models, *Aerosol Sci. Technol.*, **31**, 487-514.

Zhang, Y., C. Seigneur, J.H. Seinfeld, M. Jacobson, S.L. Clegg and F.S. Binkowski, 2000. A comparative review of inorganic aerosol thermodynamic equilibrium modules: similarities, differences, and their likely causes, *Atmos. Environ.*, **34**, 117-137.

Target:

Assessment Tools for Ozone, PM, and Regional Haze

About EPRI

EPRI creates science and technology solutions for the global energy and energy services industry. U.S. electric utilities established the Electric Power Research Institute in 1973 as a nonprofit research consortium for the benefit of utility members, their customers, and society. Now known simply as EPRI, the company provides a wide range of innovative products and services to more than 1000 energy-related organizations in 40 countries. EPRI's multidisciplinary team of scientists and engineers draws on a worldwide network of technical and business expertise to help solve today's toughest energy and environmental problems.

EPRI. Electrify the World

Printed on recycled paper in the United States of America

1005239

EPRI • 3412 Hillview Avenue, Palo Alto, California 94304 • PO Box 10412, Palo Alto, California 94303 • USA
800.313.3774 • 650.855.2121 • askepri@epri.com • www.epri.com